



POLITECNICO DI TORINO

M.Sc in Biomedical Engineering

Master's Degree Thesis

**The impact of inlet velocity profile shape on
computational hemodynamic results in left
circumflex coronary arteries**

Supervisor:

Prof. Umberto Morbiducci

Co-supervisor:

Prof. Diego Gallo

Dr. Claudio Chiastra

Ing. Maurizio Lodi Rizzini

Author:

Giulio Indennitate

July 2020

*Alla mia famiglia per avermi sempre sostenuto,
a me stesso per averci sempre creduto.*

*“Rachel, non è tanto chi sono,
quanto quello che faccio, che mi qualifica.”
(Batman Begins, 2005)*

Abstract

Nowadays, hemodynamics in blood vessels can be analyzed by means of numerical simulations. Such methods, based on patient-specific image-based three-dimensional models, represents a powerful tool with many potential clinical applications such as diagnoses of vascular diseases or post-surgical follow-ups. To make the numerical model and the related results reliable, realistic boundary conditions are required. The aim of this thesis was to evaluate the impact that inflow velocity profile has on hemodynamic results. To do that, 6 left circumflex coronary artery geometries were reconstructed from clinical images of subjects which underwent invasive coronary cineangiography after heart transplant with no sign of atherosclerosis provided by Città della Salute e della Scienza hospital (Turin, Italy). After the three-dimensional reconstruction of the vessels, 11 different velocity profiles were generated by means of analytical formulations taking in account three-dimensional features such as eccentricity and different patterns of secondary flows. Then, steady-state computational hemodynamics simulations were performed prescribing the custom-made profiles to each model and their results were compared both in terms of near-wall (wall shear stress) and intravascular (helical flow) hemodynamics. As can be seen from the near-wall results, differences due to the shape of the velocity profile were found only near the inlet. Same observations can be translated also to intravascular flow results with higher differences near to the inlet zone which became negligible after a certain distance. In conclusion, the shape of velocity profiles has an impact on the computational hemodynamics results of left circumflex coronary arteries limited within a short distance from the inlet, after this, differences became negligible and the results were approximately identical.

Contents

<i>Abstract</i>	<i>iv</i>
1 Overview of the cardiovascular system	2
1.1 Blood vessels	4
1.1.1 Structure of the vessel wall	5
1.1.2 Biomechanical properties	6
1.2 Coronary arteries	7
1.3 Blood	9
1.3.1 Plasma	9
1.3.2 Red blood cells	9
1.3.3 White blood cells.....	10
1.3.4 Platelets	11
1.4 Atherosclerosis	11
2 Hemodynamics	14
2.1 Principles of fluid dynamics	14
2.1.1 Navier-Stokes equations.....	15
2.1.2 Reynolds number.....	19
2.2 Blood rheology	20
2.3 Non-Newtonian models	23
2.4 Hagen-Poiseuille law	25
2.5 Flow in a curved pipe	27
2.5.1 Secondary flow	27
2.6 Hemodynamics and vessel pathophysiology	28
3 Computational Hemodynamics	31
3.1 Computational fluid dynamics	31
3.1.1 Finite volume method.....	33

3.2	Cardiovascular modeling	34
3.2.1	What is a model?	34
3.2.2	Multiscale modeling	34
3.2.3	Patient-specific modeling	35
3.2.4	Boundary conditions	36
4	<i>From clinical image to numerical results</i>	38
4.1	Imaging and 3D vessel reconstruction	38
4.2	Geometry preparation	40
4.3	Mesh generation	41
4.4	Mathematical model	44
4.5	Inflow conditions	45
4.6	Outflow conditions	49
4.7	Sensitivity analysis	50
4.8	Hemodynamic descriptors and data analysis	52
5	<i>Results and discussion</i>	56
5.1	Surface results	56
5.1.1	Wall shear stress (WSS)	56
5.1.2	Axial wall shear stress (WSSax)	65
5.1.3	Secondary wall shear stress (WSSsc)	73
5.1.4	Wall shear stress ratio (WSSratio)	81
5.2	Volume results	88
5.2.1	Local normalized helicity (LNH)	88
5.2.2	Quantification of helicity	90
6	<i>Conclusions</i>	96
	<i>Bibliography</i>	98

1 Overview of the cardiovascular system

The cardiovascular system consists of heart, blood vessels (veins and arteries) and blood which transport nutrients (such as amino acids and electrolytes), oxygen, carbon dioxide, hormones and blood cells to and from the whole body. It has a fundamental role in fighting diseases and providing for homeostasis and basic functions of human cells and organs. The heart is a muscular organ made of two synchronised sides, right and left, each side separated into atrium and ventricle by an atrioventricular valve: the left side supplies the systemic circulation collecting oxygenated blood from the pulmonary veins and perfuses the rest of the body whereas the right side collects deoxygenated blood from the systemic veins and perfuses the lungs and the left side [1].

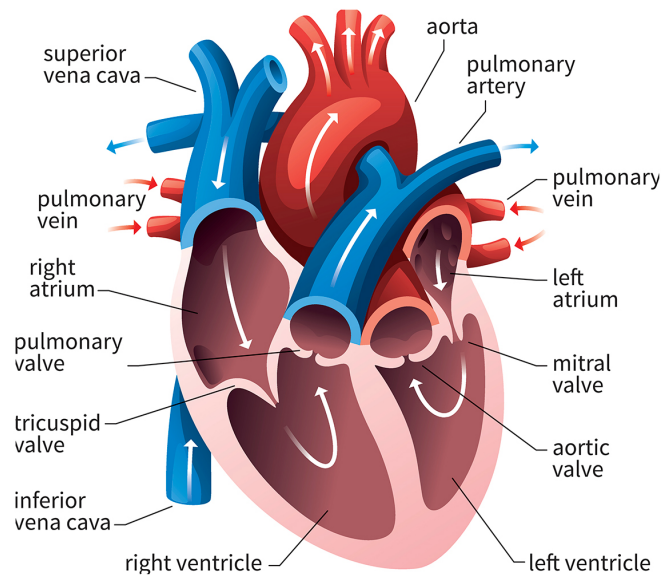


Figure 1.1 Sketch of a cross section of the heart [2]

Blood flows through the heart in a single direction because of the valvular system that regulates opening and closure of valves as an effect of a pressure gradient.

The valvular system is composed by four valves of two different types:

- Atrioventricular valve, separate the atrium from the ventricle
 - Tricuspid valve (or right atrioventricular valve)
 - Bicuspid valve (or left atrioventricular valve, or mitral valve)
- Semilunar valve, separate the ventricle from the outgoing blood vessels
 - Pulmonary valve (or right semilunar valve)
 - Aortic valve (or left semilunar valve)

The vascular network can be divided into three main groups:

1. Systemic circulation originates in the left side of the heart and functions by receiving oxygenated blood into the left atrium from the lungs which flows down into the left ventricle via the bicuspid valve. From the left ventricle, oxygen-rich blood is pumped to all organs of the human body through the aortic valve. It removes waste substances from body tissues and returns deoxygenated blood to the right side of the heart.
2. In pulmonary circulation deoxygenated systemic blood reach the right atrium via the superior vena cava and inferior vena cava. Then, this blood is pumped to the right ventricle and eventually flows through the pulmonary artery ending into the lungs for gas exchange.
3. Coronary circulation is the network needed to perfuse the heart. Begins from the aortic root by two coronary arteries, right coronary artery and left coronary artery, and through their branches supply oxygenated blood to the heart muscle tissue. Venous blood returns into the coronary sinus via the coronary veins and eventually ends into the right atrium [1].

1.1 Blood vessels

Blood vessels form the living system of “tubes”, made up of arteries and veins, of the human body. The vascular networks are closed and dense systems of deformable vessels with highly different diameters and length. The main task of arterial and venous vessels is to carry blood to and from the various tissues and organs. The anatomical configuration of the vasculature and the mechanisms that dilate and constrict blood vessels regulates the amount of blood flow and blood pressure to specific organs or tissues. Most major organ systems present a parallel arrangement between the venous network and the arterial network. Basically, this layout is needed to avoid that blood flow changes in one organ affects blood flow in other organs [3]. Blood vessels may be summarised with respect to their diameter, their function, blood velocity and many other features.

Vessel type	Diameter (mm)	Length (mm)
Aorta	22	600
Large arteries	6	300
Small arteries	2	50
Arterioles	0.02	3
Capillaries	0.01	1
Venules	0.04	3
Small veins	2	50
Large veins	10	300
Venae cava	22	500

Table 1.1 Types of blood vessels and corresponding diameters [4]

The systemic network starts with the aorta and progressively divides, increasing the number of vessels and the whole cross-sectional area. Beyond the capillary beds the vessels gradually unite until there are just two vessels, the inferior and

superior vena cava, connected back the right side of the heart. Using a simpler classification system, blood vessels can be distinguished into:

- Large vessels
- Small vessels (or microcirculation)

The threshold value of the diameter between these two categories is discussed by many authors and it ranges approximately from diameters of 100 to 250 μm [5]. This threshold is typically used since the structure of the smallest arteries and arterioles and of smallest veins and venules are very similar. Furthermore, in microcirculation another noticeable feature is that Reynolds number (Reynolds number will be defined in next chapter) is generally $\ll 1$, which means that viscous forces are greater than inertial forces.

1.1.1 Structure of the vessel wall

The wall of arteries and veins has the same histological structure made up of three layers, better known as tunics, with different functionalities and mechanical properties [6]:

1. The tunica adventitia (or tunica externa), the outer layer. It consists of connective tissue, elastic fibers, nerves and the vasa vasorum, small vessels that supply blood to vessels itself. Normally it is the thickest tunics in veins.
2. The tunica media, the middle layer, is composed by smooth muscle cells and elastic tissue. It is responsible for the vasoconstriction and vasodilation of the vessel. Vasoconstriction decreases blood flow as the smooth muscle cells contracts and the blood pressure increase as a consequence of the narrowing of the lumen. With the same principle, vasodilation increases the blood flow as smooth muscle cells relaxes and blood pressure decrease. Larger arteries are also provided of the external elastic membrane which separates the tunica media from the tunica adventitia
3. The tunica intima, the innermost layer, exposed to the blood. It consists of a single layer of endothelial cells, biological mechanotransducers that

sense pressure changes as biological signals for vasoconstriction and vasodilation. Larger arteries have also thick layer of elastic fibers called internal elastic membrane which provide elasticity to the wall of the vessel. The elastic membrane is fenestrated enabling exchange of materials between the tunics. Unlike larger arteries, veins are not provided of the internal elastic membrane and in addition, some of them, contain one-way valves to prevent blood flowing backward.

Typically, arteries have a smaller lumens and ticker walls than veins because they are closer to the heart and receive high-pressure blood [6], [7].

1.1.2 Biomechanical properties

As far as structural properties are concerned, the two main constituent materials of arteries are collagen and elastin. The collagen is arranged in an irregular network in the tunica adventitia in low mechanical stress conditions. As mechanical stress increases, the collagen molecules reorganize themselves providing stiffness to the wall. Elastin is a protein which form a thin layer between the tunica intima and the tunica media, the internal elastic membrane. The mechanical behaviour of collagen and elastin may be tested by a stress-strain test.

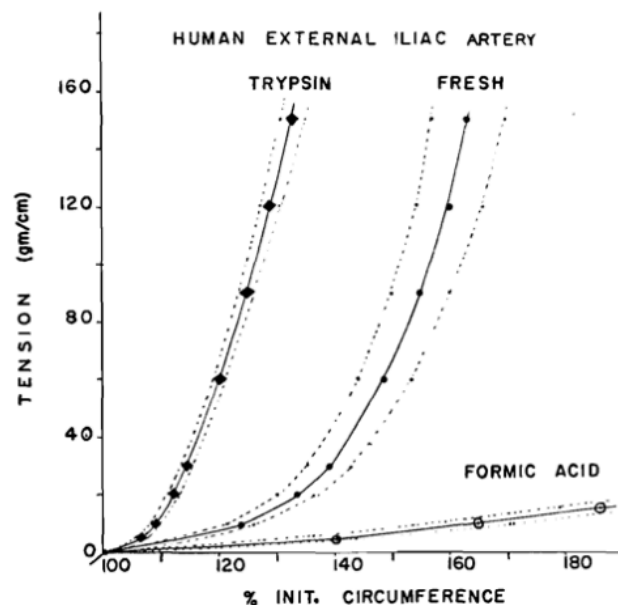


Figure 1.2 Stress-strain curve of an iliac artery [8]

Figure 1.2 depicts the stress-strain curves of three different samples of the same artery. In the left curve the elastin has been digested using trypsin, in this way mechanical behaviour depends only on collagen. In the right curve collagen has been removed which means that mechanical behaviour is governed by elastin. Firstly, the curves show a non-linear shape due to the heterogeneous material of the wall. At low strains collagen shows stresses greater than elastin, in other words it has a higher elastic modulus, approximately 100 MPa while the elastic modulus of the elastin varies between 0.4 MPa and 0.6 MPa [4]. As for the veins, from the histological point of view, smooth muscle fibers are arranged as a short-pitch helix. Elastin fibers form a fenestrated layer while collagen forms an unorganized network until a proper stress is imposed. At the beginning, the stress development is due to the smooth muscle cells. After that, elastin fibers contribute to the tension increase. As the strain grows, collagen fibers rearrange themselves in a straight configuration which corresponds to a higher tension.

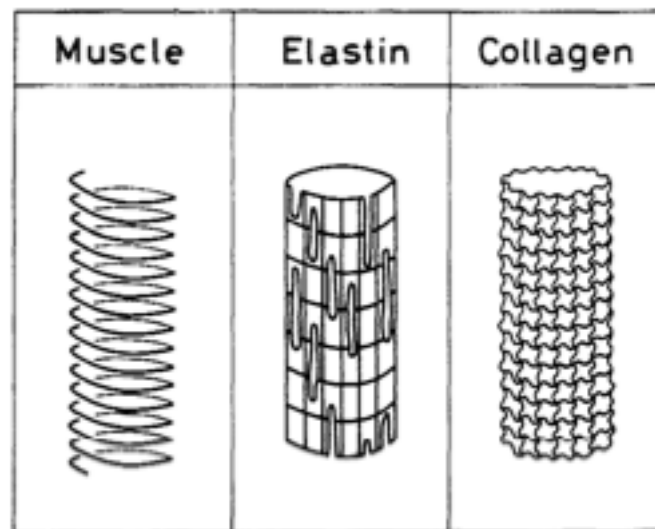


Figure 1.3 Arrangements of constituent materials of the vein wall [9]

1.2 Coronary arteries

Coronary arteries have a relevant role in blood circulation because they provide oxygenated blood to the heart which requires a continuous supply of oxygen to

survive and work properly, like every other organ or tissue of the human body. Coronary arteries form a network that lies on the external wall of the heart. They arise from the sinuses of Valsalva and converge towards the cardiac apex. There are two main coronary arteries: the left coronary artery (LCA), which bifurcates in left anterior descending coronary artery (LAD) and left circumflex coronary artery (LCX), and the right coronary artery (RCA).

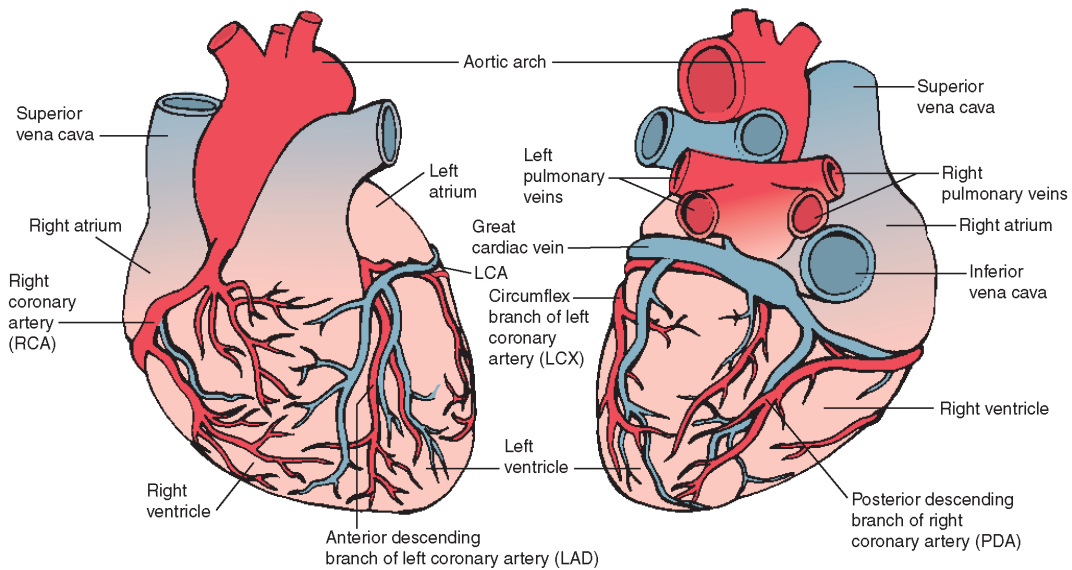


Figure 1.4 Coronary arteries and cardiac veins [10]

The RCA supplies the right side of the heart. It stems from the right sinus of Valsalva of the ascending aorta, runs to the right between the pulmonary artery and the right side of the heart, descends across the right atrioventricular sulcus and continues posteriorly towards the crux of the heart. The RCA is divided into a proximal segment, a middle segment and a distal segment. It may give rise several branches and its normal length varies between 12 and 14 cm. The LCA stems from the left sinus of Valsalva and passes between the the main pulmonary artery and the left auricle. Its normal length is from 2 cm to 4 cm and bifurcates into the LAD and the LCX [11]. The LAD originates from the bifurcation of the LCA and descends towards the apex of the heart. Its length varies from 10 cm to 13 cm and give rise to diagonal and septal branches. Such coronary artery can be divided into a proximal segment, a middle segment and a distal segment [11], [12]. The LCX typically arises from LCA bifurcation, runs in the posterior intraventricular groove

and provides blood to the inferior wall and inferior third of the intraventricular septum. It has only two segments: the proximal segment and the distal segment, divided by the first obtuse marginal branch. Its average length varies between 5 cm to 8 cm [12].

1.3 Blood

Blood is the fluid that flows through the cardiovascular network. It can be seen as a suspension of many different particles (red blood cells, white blood cells and platelets) in a fluid (plasma) with complex rheological properties discussed in next chapter. It has several important tasks:

- Transports oxygen to tissues and organs, by means of haemoglobin located inside the red cells, carrying away carbon dioxide
- Transports nutrient substances, such as amino acids, sugar, minerals, and collects waste products
- Contributes to regulate the body temperature
- Transports hormones, enzymes and vitamins
- Defends the organism by means of white cells
- Plays a fast healing function of wounds through the coagulation

1.3.1 Plasma

The plasma is a fluid that consist mainly of water (about 90%), electrolytes and other macromolecules. It contains glucose, lipids, proteins, glycoproteins, hormones, amino acids and vitamins. Proteins, including fibrinogen and other clotting factors, is the most abundant solute by weight varying to 6.5 to 8 g/dl. Albumin is the main plasma protein. One of the functions of plasma proteins is to regulate the osmotic pressure of the blood [13].

1.3.2 Red blood cells

The red blood cell (also called erythrocyte) is a small biconcave disc-shaped cell devoid of nucleus delimited by a membrane called stroma. Its diameter is about 8

μm . Inside its cytoplasm is located a solution of haemoglobin, the red protein that gives the red blood cell its color and carries most of the oxygen. The haematocrit is the percent by volume of red cells. It depends from lifestyle, gender, age. The haematocrit has a normal range of 41-52% in men and 36-48% in women [4].

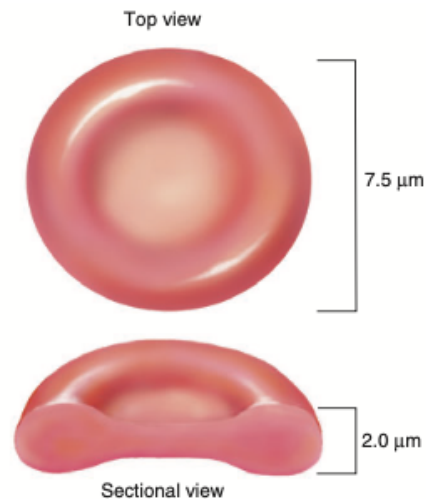


Figure 1.5 Red blood cell [6]

High haematocrit means a highly oxygenate blood, on the other hand it is also a risky condition because blood has a higher viscosity which means a greater resistance to flow and increased probability of clinical events. Since the capillary diameter are often smaller than the red blood cell diameter, during their travel through the microcirculation this kind of cells have to considerably deform themselves. Red blood cells live for about 120 days and are constantly regenerated by the bone marrow. The red blood cells production process is known as haemopoiesis.

1.3.3 White blood cells

White blood cells (or leukocytes) are globular cells which play an important role in the body's defense against pathogens. Unlike red blood cells, they contain nuclei and are less deformable. White blood cells may be divided in five big groups: neutrophils, eosinophils, basophils (called granulocytes) and lymphocytes, monocytes (called agranulocytes).

1.3.4 Platelets

Platelets, also called thrombocytes, are much larger cells with a diameter of about 3 μm . They live approximately for 10 days and participate in blood clotting process known as haemostasis. Platelets exist in unactivated and activated forms. When activated, platelets become bigger and able to group together. When a vessel is broken collagen fibers of its wall are exposed to the blood. Upon contact with collagen, platelets become activated and adhere to the vessel and other platelets repairing the damaged area [6].

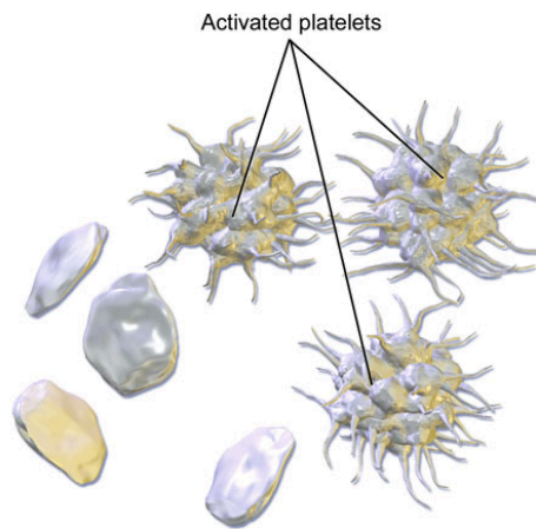


Figure 1.6 Unactivated and activated platelets [4]

1.4 Atherosclerosis

Atherosclerosis (from Greek *ἀθήρα* (athera), meaning ‘gruel’, and *σκλήρωσις* (sklerosis), meaning ‘hardening’) is a vascular disease of large and medium arteries such as aorta, coronary arteries and brain arteries, leading to narrowing of the vessel lumen and hardening of the arterial wall [14]. Such disorder is caused by the buildup and spreading in the tunica intima of several plaques known as atheromas (or atheromatous plaques), lesions composed of a core of lipids, macrophage cells, platelets and proteins, and an external cap of fibrous tissue.

Besides it is a rarely fatal inflammatory chronic condition, a plaque rupture may lead to thrombosis.

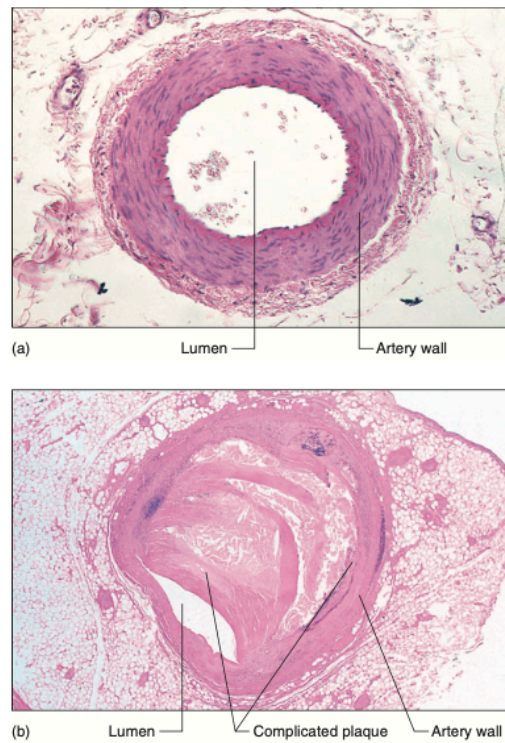


Figure 1.7 (a) Cross section of a healthy artery; (b) cross section of an artery with atherosclerosis [6]

Thrombi or plaque debris produce emboli into the blood stream which may cause heart attacks, strokes or ischemia[15]. The atheromatous plaques development is divided in seven stages.

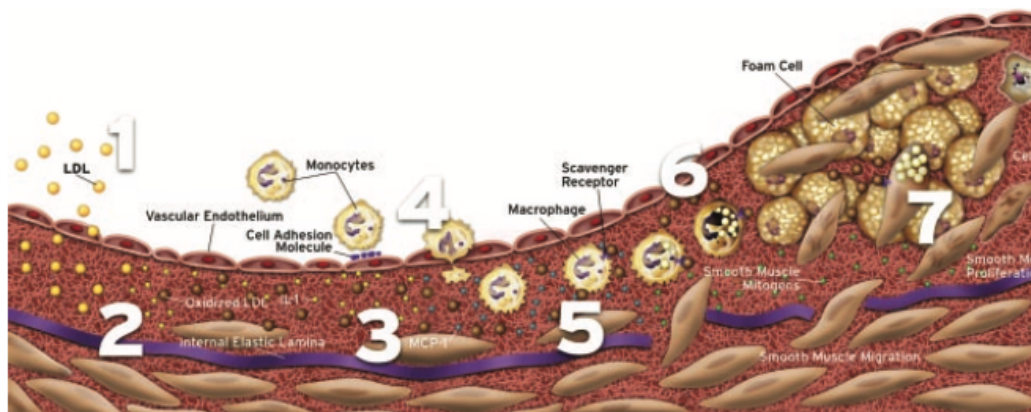


Figure 1.8 The 7 stages of development of an atherosclerotic plaque [16]

Firstly, low-density lipoprotein (LDL) moves under the endothelium and is oxidized by macrophage and smooth muscle cells. After that, platelet adhesion release growth factors which attract additional macrophages. Smooth muscle cells move from the tunica media to the tunica intima which eventually causes the growth of the plaque[16]. Among the risk factor, probably the most important is the plasma cholesterol level. Other risk factors are aging, diet, sedentary lifestyle, hypertension, diabetes, male gender, cigarette smoking. Furthermore, as discussed in the next chapter, lesions development is also related to hemodynamics and geometry of blood vessels.

2 Hemodynamics

Hemodynamics is the physical study of the blood flow and of all the vasculatures through which blood flows [17]. Even if blood is not a fluid but a suspension of many particles as previously described in paragraph 1.3, to evaluate the blood flow and its role in the development of vascular pathologies, the use of fluid dynamics laws is needed.

2.1 Principles of fluid dynamics

Fluids, including both liquids and gases, are substances tending to flow or conform to the shape of their container. One of the main physical properties of fluid is *density* ρ , the mass per unit volume expressed in $\left[\frac{kg}{m^3}\right]$. Unlike gases, liquids' density does not misurably change with temperature and pressure, for this reason it may be considered constant. A fluid having this feature is called *incompressible fluid*. Another important property of the fluid is the *dynamic viscosity* μ expressed either in $[Pa \cdot s]$, according to the MKS system, or

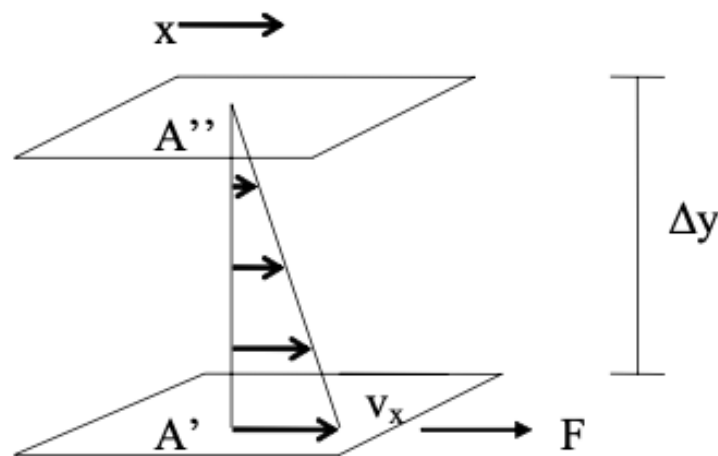


Figure 2.1 Illustration of Newton's experiment [18]

in Poise [P]¹ according the CGS system. The viscosity of a fluid is a measure of its resistance to the transmission of forces. It has been defined by Newton putting a fluid between two infinitely large parallel plates, one fixed and one in motion at velocity v through the action of a force F and eventually obtaining the following Newton's law of viscosity:

$$\frac{F}{A} = \mu \frac{v_x}{\Delta y} \quad 2.1$$

The term $\frac{F}{A} = \tau$ is know as *shear stress*. The term $\frac{v_x}{\Delta y}$ can be written as follows:

$$\frac{dv_x}{dy} = \lim_{\Delta y \rightarrow 0} \frac{v_x(y_1) - v_x(y_0)}{y_1 - y_0} = - \frac{v_x}{\Delta y} \quad 2.2$$

where $\dot{\gamma} = -\frac{dv_x}{dy}$ is called *shear rate*. So, the equation 2.1 may be written as:

$$\tau = \mu \dot{\gamma} \quad 2.3$$

According to their viscosity, fluids can be separated in two main groups:

- *Newtonian*, if $\mu = \text{constant}$
- *Non-Newtonian*, if $\mu = \mu(\dot{\gamma})$

2.1.1 Navier-Stokes equations

The *Navier-Stokes equations* are the governing equations of the motion of fluids. Under the assumption of fluid as a continuum, which means that its molecular nature is neglected, these equations arise from mass and momentum conservation via a Eulerian framework.

¹ 1 Poise = 0,1 Pa · s

The Eulerian mass conservation can be expressed considering an infinitesimal parallelepiped with volume $dV = dx dy dz$, density $\rho = \rho(x, y, z)$ and mass $m = \rho dV$.

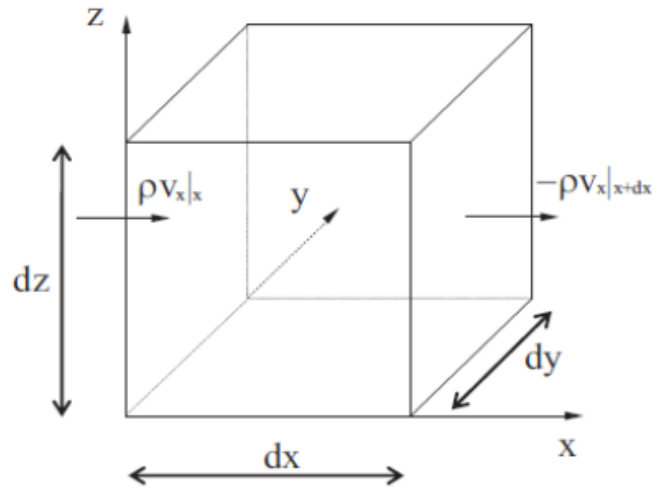


Figure 2.2 Infinitesimal volume [19]

The variation in time of mass inside the volume is:

$$\frac{\partial \rho}{\partial t} dx dy dz \quad 2.4$$

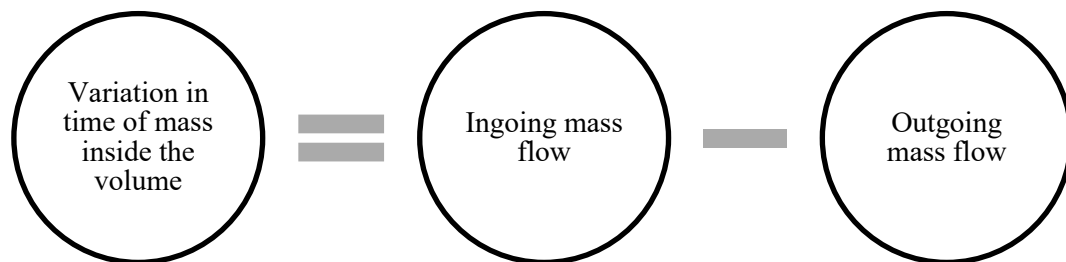


Figure 2.3 Conservation of mass

Then we have an ingoing/outgoing mass flow for each face of the volume. For instance, considering x direction, the ingoing mass flow is:

$$\rho v_x|_x dydz \quad 2.5$$

while the outgoing mass flow is:

$$\rho v_x|_{x+dx} dydz \quad 2.6$$

The variation of mass due to equation 2.5 and equation 2.6 divided by the volume is:

$$\begin{aligned} \lim_{dx \rightarrow 0} \frac{\rho v_x|_x dydz - \rho v_x|_{x+dx} dydz}{dx dydz} \\ = - \frac{\rho v_x|_{x+dx} - \rho v_x|_x}{dx} = - \frac{\partial \rho v_x}{\partial x} \end{aligned} \quad 2.7$$

The same thing applies to the mass flows in y and z direction. The variation in time of mass inside the volume became:

$$\frac{\partial \rho}{\partial t} = - \frac{\partial \rho v_x}{\partial x} - \frac{\partial \rho v_y}{\partial y} - \frac{\partial \rho v_z}{\partial z} \quad 2.8$$

The previous equation can be written as:

$$\frac{\partial \rho}{\partial t} + v_x \frac{\partial \rho}{\partial x} + v_y \frac{\partial \rho}{\partial y} + v_z \frac{\partial \rho}{\partial z} + \rho \frac{\partial v_x}{\partial x} + \rho \frac{\partial v_y}{\partial y} + \rho \frac{\partial v_z}{\partial z} = 0 \quad 2.9$$

Using total derivative, we have:

$$\frac{D\rho}{Dt} + \frac{\rho \partial v_x}{\partial x} + \frac{\rho \partial v_y}{\partial y} + \frac{\rho \partial v_z}{\partial z} = 0 \quad 2.10$$

For an incompressible fluid ($\rho = \text{constant}$), equation 2.10 may be written as:

$$\nabla \cdot \vec{v} = 0 \quad 2.11$$

The previous equation is also called *continuity equation*.

As for the Eulerian momentum conservation, the variation in time of momentum inside the considered volume in x direction is:

$$\frac{\partial(\rho v)_x}{\partial x} dx dy dz \quad 2.12$$

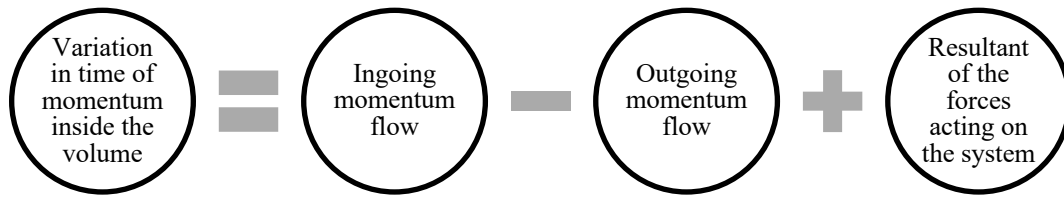


Figure 2.4 Conservation of momentum

The ingoing convective term of momentum flow through the volume surface in x direction is:

$$(\rho v_x) v_x |_x dy dz \quad 2.13$$

While the outgoing term is:

$$(\rho v_x) v_x |_{x+dx} dy dz \quad 2.14$$

The same thing applies to the momentum flows through the other surfaces. The total convective contribute in x direction is:

$$dy dz [(\rho v_x) v_x |_x - (\rho v_x) v_x |_{x+dx}] + dx dz [(\rho v_x) v_y |_y - (\rho v_x) v_y |_{y+dy}] + dx dy [(\rho v_x) v_z |_z - (\rho v_x) v_z |_{z+dz}] \quad 2.15$$

The contribute due to the shear stresses (tangential forces) is:

$$dydz[(\tau_{xx})|_x - (\tau_{xx})|_{x+dx}] + dx dz[(\tau_{yx})|_y - (\tau_{yx})|_{y+dy}] + dx dy[(\tau_{zx})|_z - (\tau_{zx})|_{z+dz}] \quad 2.16$$

Eventually, there are pressure forces (normal forces) and external body forces (gravity):

$$dydz[p|_x - p|_{x+dx}] + \rho g_x dx dy dz \quad 2.17$$

So putting together all the terms and dividing them by $dx dy dz$ the x component of momentum conservation is:

$$\begin{aligned} \frac{\partial(\rho v)_x}{\partial x} = & - \left(\frac{\rho \partial v_x v_x}{\partial x} + \frac{\rho \partial v_y v_x}{\partial y} + \frac{\rho \partial v_z v_x}{\partial z} \right) \\ & - \left(\frac{\partial \tau_{xx}}{\partial x} + \frac{\partial \tau_{yx}}{\partial y} + \frac{\partial \tau_{zx}}{\partial z} \right) - \frac{\partial p}{\partial x} + \rho g_x \end{aligned} \quad 2.18$$

Using the equation 2.11, after some calculations, the three components of momentum conservation may be written as:

$$\rho \frac{D\vec{v}}{Dt} = -\nabla p - \nabla \cdot \bar{\tau} + \rho \vec{g} \quad 2.19$$

Equations 2.19 and 2.11 are known as Navier-Stokes equations for incompressible fluids. Since they are non-linear partial differential equations, finding an analytical solution is, in most of cases, an impossible task. The non-linearity is due to the convective term of the equation of momentum conservation. For this reason, Navier-Stokes equations are typically solved by means of computational methods.

2.1.2 Reynolds number

The Reynolds number is a dimensionless parameter given by:

$$Re = \frac{\rho \vec{v} L}{\mu} = \frac{\text{inertial forces}}{\text{viscous forces}} \quad 2.20$$

where ρ is the fluid density, \vec{v} is the the fluid velocity, L is the characteristic dimension of the considered geometry (vessel, pipe, etc) and μ is the fluid dynamic viscosity. From a physical point of view, it represents the ratio of the inertial forces to the viscous forces. According to Reynolds number, fluid flow in pipes is typically classified in:

- *Laminar flow* ($Re < 2000$): occurs at low Reynolds numbers. Flow appears organized, with no mixing, with each fluid layer slide over the adjacent one.
- *Transitional flow* ($2000 < Re < 10000$): is a mixture of laminar and turbulent flow, viscous and inertial forces are significantly unbalanced.
- *Turbulent flow* ($Re > 10000$): occurs at high Reynolds numbers. Inertial forces are dominant. Flow is characterized by chaotic structures such as eddies and vortices.

2.2 Blood rheology

Rheology (from Greek $\rho\epsilon\omega$ (reo), meaning ‘to flow’) is the science of how materials flow and deform in response to applied forces. As already discussed, blood is a suspension of particles (blood cells) in a water-like solution (plasma). Unlike plasma, blood shows a strongly shear-thinning² non-Newtonian behaviour, particularly in a certain flow condition. Its mechanical behaviour is highly governed by the red blood cells because they are plenty more than white cells or platelets. In fact, it was shown that blood density depends on haematocrit according the following formula:

² Behaviour of fluids whose viscosity decrease as shear rate increase

$$\rho_b = (1 - Ht)\rho_p + Ht\rho_{gr} \quad 2.21$$

where $\rho_p=1035 \frac{kg}{m^3}$ is the plasma density and $\rho_{gr}=1090 \frac{kg}{m^3}$ is the density of blood particles. A healthy adult with $Ht=45\%$ has $\rho_b=1060 \frac{kg}{m^3}$ [13]. Blood viscosity depends on plasma viscosity, that under physiological condition varying between 1.1 and 1.6 cP:

$$\begin{cases} \mu_p = 1.8 \cdot \mu_w, & T > 20^\circ C \\ \mu_p = \mu_w(1.32 + 0.024 \cdot T), & T < 20^\circ C \end{cases} \quad 2.22$$

Since plasma is mainly composed of water, its viscosity depends on water viscosity. Water viscosity can be expressed as follows:

$$\mu_w = \frac{\mu_0}{(1 + 0.0337 \cdot T + 0.00022 \cdot T^2)} \quad 2.23$$

where μ_w is water viscosity, $\mu_0=1.808$ cP is water viscosity at $T=0$ °C and T is the temperature expressed in °C. Even though each protein differently impacts on blood viscosity, some empirical relations was developed to evaluate the relationship with protein content. Such relationship may be expressed as:

$$\mu_p = \mu_w \frac{1}{1 - k \cdot c} \quad 2.24$$

where c is protein concentration and k a constant depending on protein. In practical cases, in order to arrive at a reliable estimate of blood viscosity, the following formula is used:

$$\mu_b = \mu_p(1 + 2.5 \cdot Ht) \quad 2.25$$

Moreover, blood properties are influenced by shear rate. At very low shear rate (approximately $\dot{\gamma} < 100 \text{ s}^{-1}$), due to the presence of fibrinogen and globulin

(plasma proteins), red blood cells aggregate themselves forming *rouleaux* which implies an increase of viscosity [20]. Such phenomenon is depicted in Figure 2.5. The “normal cells in plasma” (NP) curve is related to a sample of normal blood. The “hardened cells in plasma and albumin” (HA) is related to a suspension of artificially made indeformable red blood cells. The “normal cells in plasma and albumin” (NA), related to a suspension of red blood cells in a solution containing albumin devoided of fibrinogen, shows that the aggregation of red cells seems to be blocked and as a consequence of that, the viscosity of the suspension decreases. The difference between the HA curve and NA curve highlights the influence of the deformability on viscosity of the blood [13], [21]. As shear rate increases, red cells reshape themselves and get from a random-oriented configuration to a more organized one until they orient their long axis with streamlines and the blood viscosity decreases.

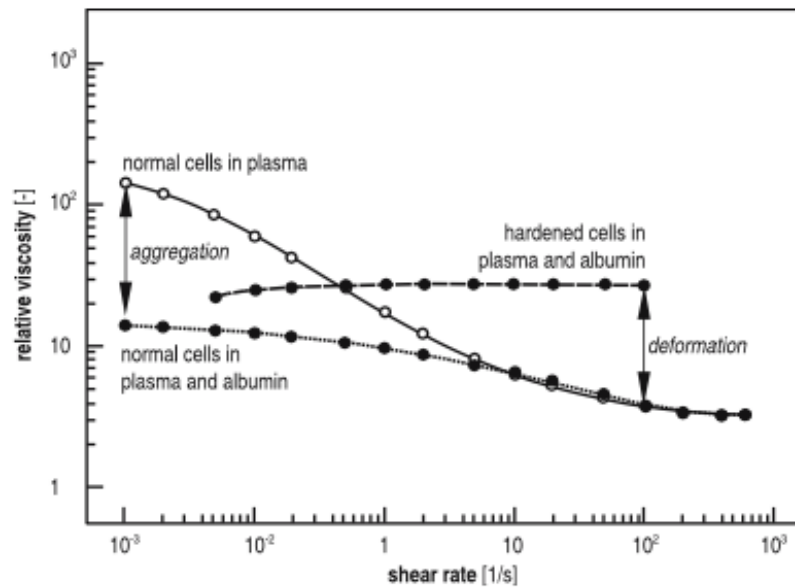


Figure 2.5 Relation between viscosity and shear rate [21]

The high deformability of red blood cells is due to the absence of a nucleus, to the elastic and viscous properties of its membrane and also to geometric factors such as its biconcave-disc shape. Furthermore, for high values of shear rate (approximately $\dot{\gamma} > 100 \text{ s}^{-1}$), blood acts like a Newtonian fluid and its viscosity became constant.

2.3 Non-Newtonian models

The most common non-Newtonian rheological models used for biological fluids are:

- Bingham model
- Casson model
- Casson model
- Power-Law model
- Carreau model

The Bingham model is described by the following relation:

$$\tau = \tau_0 + \mu_B \cdot \dot{\gamma} \quad 2.26$$

where μ_B is the Bingham viscosity and τ_0 is the minimum value of shear rate needed to produce the fluid motion known as *yield stress*. For low shear stresses ($\dot{\gamma} < 100 \text{ s}^{-1}$) it roughly approximates blood behaviour.

The Casson model is given by:

$$\sqrt{\tau} = \sqrt{\tau_0} + \sqrt{\mu_C} \cdot \sqrt{\dot{\gamma}} \quad 2.27$$

where μ_B is the Casson Viscosity. Casson relation is similar to the previous one, it was obtained by fitting experimental data. Such model is highly hematocrit-influenced.

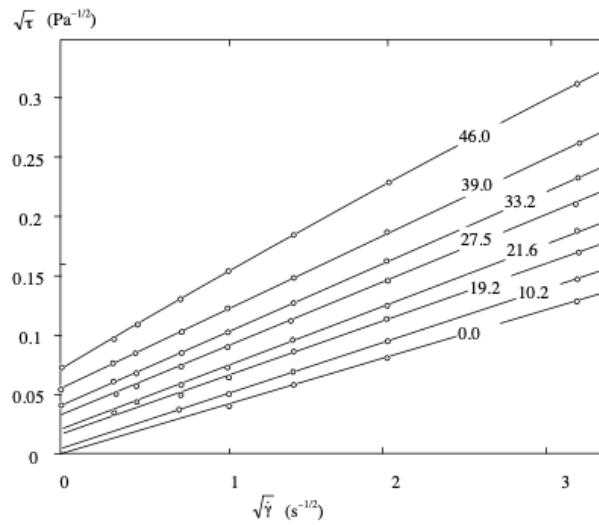


Figure 2.6 Casson model for different hematocrit values [13]

The Power-Law of blood viscosity is:

$$\mu(\dot{\gamma}) = k(\dot{\gamma})^{n-1} \quad 2.28$$

where in its exponent n and parameter k depends on hematocrit and plasma volume devioded of albumin.

Since blood has a typical shear thinning behaviour under certain conditions, the following model is used to better describe its viscosity.

The Carreau model is given by:

$$\mu(\dot{\gamma}) = \mu_{\infty} + (\mu_0 - \mu_{\infty})[1 + (\lambda\dot{\gamma})^2]^{\frac{n-1}{2}} \quad 2.29$$

where μ_0 and μ_{∞} are the infinite and zero shear rate limit viscosities respectively, λ is the relaxation time constant and n the power law index.

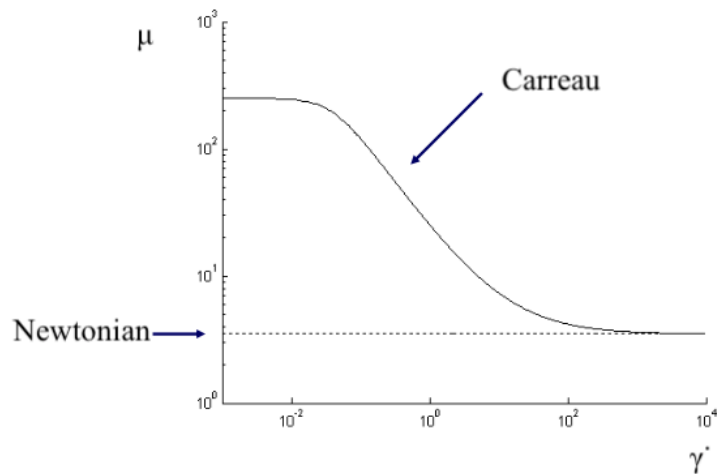


Figure 2.7 Shear rate varying Carreau and Newtonian viscosity

Transitions and slope in the power law region of the plot are controlled by the relaxation time constant λ and the power law index n , respectively.

2.4 Hagen-Poiseuille law

In this particular case, the Navier-Stokes equations admit an analytical solution. It was experimentally derived by Jean Leonard Marie Poiseuille and Gotthilf Heinrich Ludwig Hagen in 1839 aiming to understand the physical factors governing blood flow, and published by Poiseuille in 1840-41 and 1846 [22].

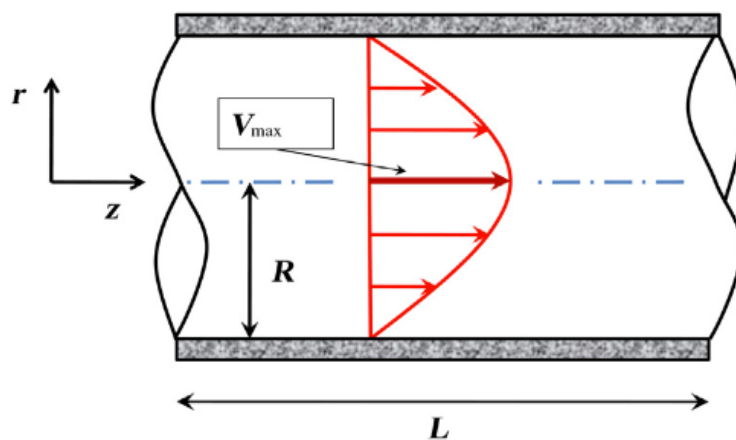


Figure 2.8 Longitudinal view of the pipe [23]

This law describes the flow of a fluid in a rigid cylindrical pipe using a cylindrical reference system (r, θ, z) . It is based on the following assumptions:

- Newtonian and incompressible fluid
- Laminar flow: $v_r = v_\theta = 0$
- Steady flow: v_z does not depend on time t
- Axial symmetry: v_z does not depend on θ
- Fully developed flow: v_z does not depend on z
- No-slip conditions on the walls: $v_z(r = R) = 0$

The Navier-Stokes equations in this case are reduced to:

$$-\frac{\partial p}{\partial z} + \frac{\mu}{r} \frac{\partial}{\partial r} \left(r \frac{\partial v_z}{\partial r} \right) = 0 \quad 2.30$$

Which a possible solution is:

$$v_z(r) = -\frac{\Delta P}{4\mu L} r^2 + c_1 \log(r) + c_2 \quad 2.31$$

Since for $r=0$, $\log(r) \xrightarrow{\text{yields}} -\infty$ and v_z is a continuous function, $c_1 = 0$. c_2 can be determined applying the no-slip condition. In the end, the fluid velocity is given by:

$$v_z(r) = \frac{\Delta P}{4\mu L} R^2 \left[1 - \frac{r^2}{R^2} \right] \quad 2.32$$

And its flow rate is:

$$Q = 2\pi \int_0^R v_z(r) r dr = -\frac{\Delta P}{8\mu L} \pi R^4 \quad 2.33$$

The mean velocity is:

$$\bar{v}_z = \frac{Q}{\pi R^2} = \frac{v_{zmax}}{2} \quad 2.34$$

Performing the derivative of the velocity with respect to the radius and multiplying each member by $-\mu$:

$$-\mu \frac{\partial v_z}{\partial r} = \frac{\Delta P r}{2L} = \tau = \mu \dot{\gamma} \quad 2.35$$

Which is the shear stress obtained by means of the Newton's law of viscosity. Hagen-Poiseuille law is fundamental in understanding how blood behaves inside the cardiovascular system. Even if it describes a Newtonian fluid, a non-Newtonian fluid such as blood, can be treated with equation 2.35 by replacing μ with an *apparent viscosity* μ_{app} which is not a constant anymore but it will depend on $\dot{\gamma}$ and other factors according to the considered rheological model:

$$\tau = \mu_{app} \dot{\gamma} \quad 2.36$$

2.5 Flow in a curved pipe

As already seen, cardiovascular system is a highly complex network of vessels. Its geometry varies according to the anatomical location, vessel type and other factors. Typically, vessels are not straight as hydraulic pipes: there are many curved tracts, bifurcations and branching sites which makes describing the blood flow a very hard task. To properly analyze the fluid dynamics, it is important to understand the effects of curvatures on the flow.

2.5.1 Secondary flow

In general, when a fluid flows in a curved pipe, the fluid near the central axis is driven outward due to the centrifugal force whereas fluid near the walls is driven toward the inside of the curve due to the onset of slow-velocity vortices caused by

a pressure gradient with higher pressure at the outer wall and lower pressure at the inner wall[24].

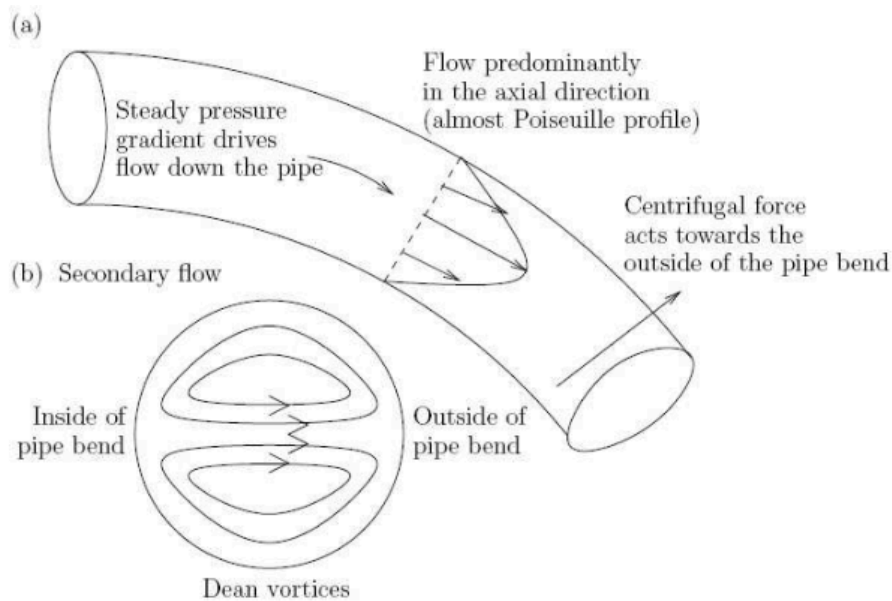


Figure 2.9 Dean flow. (a) longitudinal cross-section showing Poiseuille-like skewed profile, (b) transverse cross-section showing secondary flow [24]

So unlike Hagen-Poiseuille flow, the peak of the velocity profile is skewed toward the outer wall of the curve. Moreover, as a result of curvature counter rotating vortices lying in the transverse cross-section of the pipe occurs, known as *secondary flow*. This phenomenon was described by William Reginald Dean in 1927 who was the first to provide an analytical solution for the case of an incompressible Newtonian fluid in steady motion through a curved pipe of circular cross-section [25]. The combination of through-plane flow, represented by Hagen-Poiseuille flow, and secondary flow produce a helix-shaped blood stream known as *helical flow*, a typical characteristic of arteries [26].

2.6 Hemodynamics and vessel pathophysiology

The role played by hemodynamics on the onset of vascular pathologies is fundamental. As discussed in paragraph 1.4, atherosclerosis is the most diffuse artery disease [27]. Atherosclerosis is usually regarded as a systemic disease and

several well-identified risk factors (hypertension, diabetes mellitus, obesity, cigarette smoking, etc) are implicated in its pathogenesis. The disease is usually gradual since taking decades before the affected person is in danger of cardiovascular or cerebrovascular problems. The development of such disease is complicated, but the primary event seems to be injury to the artery's wall through various mechanisms. Among these mechanisms, there is much evidence suggesting that initiation and progression of atherosclerotic disease is influenced by hemodynamic factors. Wall shear stress is fundamental in maintaining normal functioning of the circulatory system. In fact, arteries in order to attempt in maintaining a physiological wall shear stress are able to remodel to a larger/smaller diameter. Atheroma development occurs in locations characterised by particular geometries such as bifurcations or branching sites, areas involved in flow recirculation and stasis, and also in which wall shear stress appears to be relatively low and oscillatory. On the other hand, the development of atherosclerotic plaque is inhibited in those vascular regions in which wall shear stress is higher [28],[29].

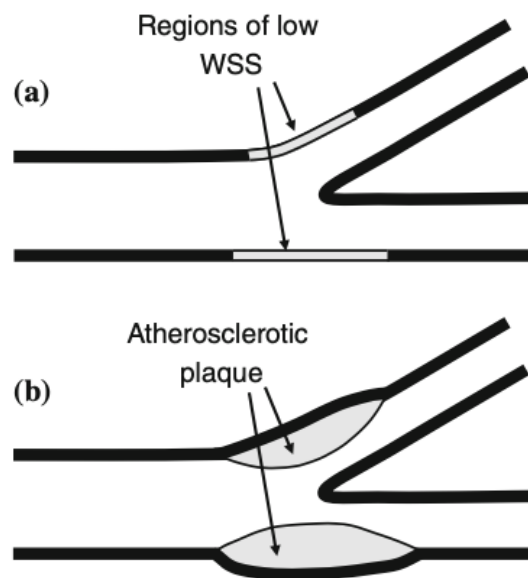


Figure 2.10 (a) low shear stress region before the onsets of the disease (b) the same region with atheromas [4]

It has been shown that wall shear stress can change the morphology and orientation of the endothelial cells. Endothelial cells subjected to laminar flow

with high values of wall shear stress tend to elongate and align according to the direction of the flow, whereas in areas subjected to disturbed flow cells are exposed to low and oscillatory wall shear stress assuming an unorganized configuration. This behaviour is related to the intima thickening process [30].

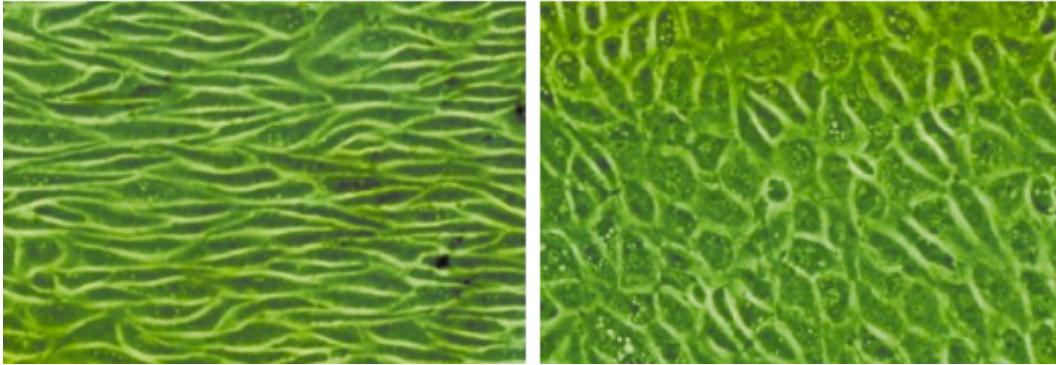


Figure 2.11 (Left) endothelial cells exposed to physiological shear stress. (Right) Endothelial cells exposed to low shear stress [29]

Besides anatomical characteristics, a developing atherosclerotic lesion can itself disturb the local hemodynamics resulting in an altered local shear stress with similar features to those seen in atherogenic sites mentioned above. In vitro studies in adult carotid bifurcations have demonstrated that areas where atherosclerotic plaques occur were associated to low and oscillatory wall shear stress[31].

All the bifurcations of the coronary circulation may also be affected by atherosclerosis. Their geometry represents a risk factor since may lead to disturbed blood flow [31]. It has been noted that the sharpness/smoothness of the arteries branching sites influence the local wall shear stress: the sharper the bifurcation the lower the shear stress [31]. In addition, recent studies have been demonstrated that besides the widely discussed wall shear stress, also physiological helical flow has a relevant impact on atherosclerosis [26]. Findings have shown that such flow arrangement is a physiological feature of hemodynamics in coronary arteries that minimizes the luminal surface exposed to low wall shear stress and suppresses flow disturbances [26].

3 Computational Hemodynamics

Computational hemodynamics is the computer-aided simulation of blood flow in the cardiovascular system. Such analysis technique allows for reconstruction of complex flow patterns with high spatial and temporal resolution in cardiovascular districts usually characterized by complex hemodynamics and highly-variable geometry. By means of computational hemodynamics it is possible to analyze and describe intravascular fluid structures and near wall features promoting the onset of vascular pathologies. For this reason, it is very promising for clinical practice because it represents a non-invasive instrument in diagnoses of cardiovascular diseases, pre-surgical planning and post-surgical follow-ups. Furthermore, it is a more economic alternative to in vitro or in vivo experiments for research and development of new medical devices, pharmaceutical products, etc. Computational hemodynamics relies on computational fluid dynamics technique [32].

3.1 Computational fluid dynamics

Computational fluid dynamics, abbreviated with CFD, is a branch of fluid mechanics that analyze and solve complex systems, usually not analytically solvable, involving fluid flow by means of numerical method. It is a very powerful and widely used technique that covers many different application areas:

- Aerodynamics of aircrafts
- Hydrodynamics of ships
- Electrical and electronic engineering
- Biomedical engineering
- Mathematics

- Physics

In most of cases, analyze and properly describe the physical phenomenon of interest is a very hard task since the governing equations do not admit an analytical solution. By means of high-performing computers, CFD is used in order to obtain the most accurate approximate solution [33].

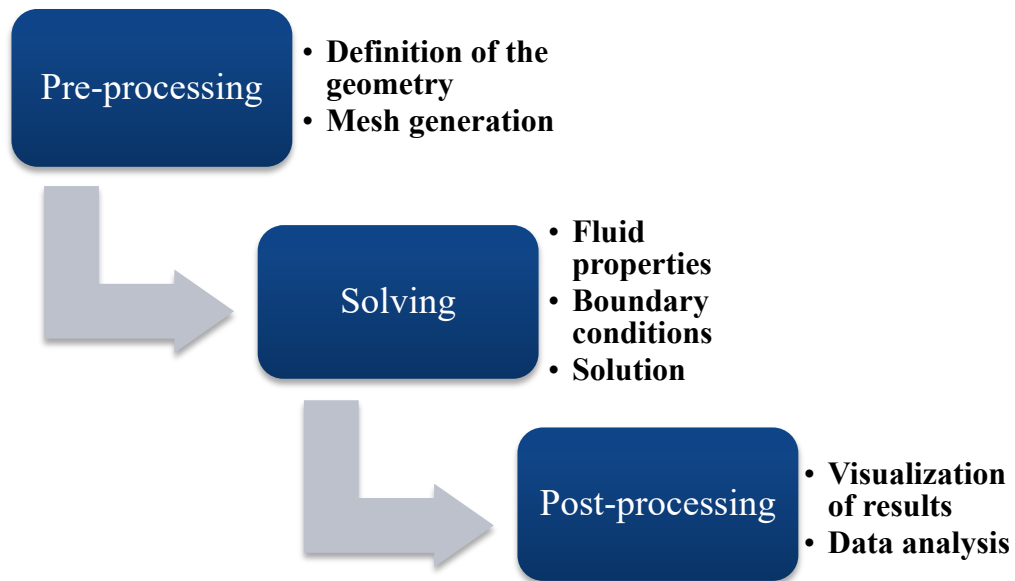


Figure 3.1 CFD simulation phases

Typically, all CFD algorithms covers three main phases:

- *Pre-processing*: during this phase, the computational domain is defined and discretized in smaller sub-domains obtaining the so-called *mesh*, a grid of elements of interest.
- *Solving*: during the solving stage the user selects properties that best describe the fluid behaviour and provide the proper boundary conditions for border elements. After that, the governing equations are solved in the volume of interest using numerical methods (finite volume method, finite element method, ...) obtaining an approximate solution of the considered problem.
- *Post-processing*: involves data analysis and visualization of results via plots, surface maps, etc.

3.1.1 Finite volume method

The *finite volume method (FVM)* is one of the existing numerical solution techniques used in CFD. It involves the discretization of fluid into discrete control volumes. The center of each volumes, known as *node*, is related to the values of the variables of interest (velocity and pressure). The governing partial differential equations are integrated over each volume and then discretized obtaining a set of algebraic equations. Considering the *i*-direction, for the analyzed node we have:

$$a_v v_i = \sum_{nb} a_{v,nb} v_{i,nb} + \sum_{e,w} a_{p,nb} p_{i,nb} + b_v \quad 3.1$$

where:

- *nb* denoted the boundary faces, *e* and *w* are east and west neighbour nodes
- *v* and *v_{nb}* represent velocity of current node and neighbour node respectively
- *a_v*, *a_{v,nb}*, *a_{p,nb}* are coefficients of current and neighbour velocity and neighbour pressure respectively
- *b_v* is a constant due to volume forces

Then the pressure is computed using the continuity equation. Since such equation in the case of incompressible fluid is devoided of a pressure term, the momentum conservation equation is solved introducing trial variables *v**, *p**. Pressure may be wrote as:

$$p = p^* + p' \quad 3.2$$

where *p'* is a correction factor. Considering the equation 3.1 and neglecting the terms related to *v_{nb}* and *b_b* we have both for the correct case:

$$a_v v_i = \sum_{e,w} a_{p,nb} p_{i,nb} \quad 3.3$$

and for the approximated one:

$$a_v v_i^* = \sum_{e,w} a_{p,nb} p_{i,nb}^* \quad 3.4$$

Subtracting 3.4 to 3.3 we have:

$$v_i = v_i^* + \frac{\sum_{e,w} a_{p,nb}}{a_v} (p_{i,nb} - p_{i,nb}^*) = v_i^* + d_f p' \quad 3.5$$

All the previous calculations are repeated for each direction of the reference system.

3.2 Cardiovascular modeling

3.2.1 What is a model?

A model is a representation of reality, involving some degrees of approximation, to answer a specific question. It consists of a set of mathematical equations. Typically, cardiovascular models may be summarised in two general categories:

- *Diagnostic models*: aims to describe one or many features related to a certain disease or health condition.
- *Prognostic models*: attempt to predict the consequences of a treatment enabling to compare more treatments selecting the best one for the case of interest.

Models can be designed with a different order of complexity. Such complexity depends on how deeply the phenomenon must be described: if the model is too simple it may not properly describe some relevant aspects, but on the other hand, if it is too complex it may probably be hard to use.

3.2.2 Multiscale modeling

Since physical phenomena occur in four dimensions (three spatial dimensions and time), models may be designed in four dimensions which means a more detailed description but also a higher complexity. On the other hand, lower dimensional

model may be less complex but also less accurate. For this reason, it is preferred to design models with different degrees of detail, using a *multiscale* approach. In fact, considering an hemodynamical problem, local models (higher dimensional model) are used to describe in detail the vascular district of interest whereas systemic models (lower dimensional models) are used to summarised and briefly describe the hemodynamical features of the rest of the system.

3.2.3 Patient-specific modeling

With the current progress in technology it has become possible to perform numerical simulations in anatomically accurate three-dimensional geometries. *Patient-specific modeling* is a new concept in describing pathophysiological features that includes the integration of data of a specific patient with numerical simulations.

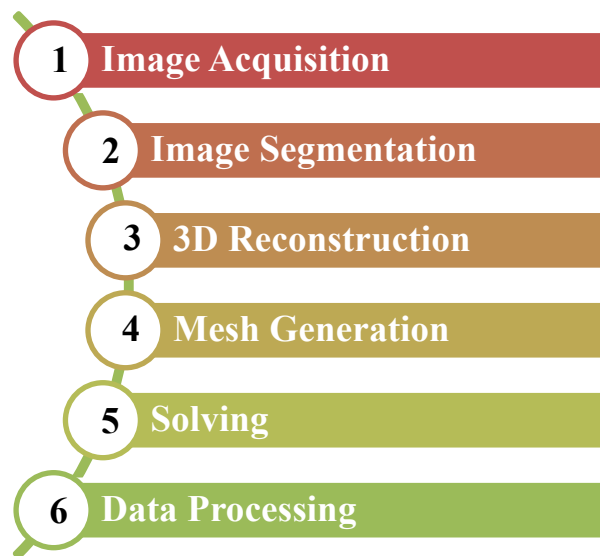


Figure 3.2 Steps of patient-specific simulation of blood flow

Such models are widely used to study clinical scenarios and hemodynamical behaviour in many cardiovascular regions. The process from clinical image to results typically involves several different steps as depicted in Figure 3.2. Firstly, clinical images of the anatomical region are acquired using either a non-invasive imaging technique such as computed tomography, magnetic resonance imaging or invasive method combining angiography and intravascular ultrasound[34]. Then the region of interest is identified through the segmentation procedure and after

that, the three-dimensional geometrical model must be reconstructed. Before solving the governing equations, the geometrical model is meshed in a finite number of smaller volumes. Lastly, results are processed and analyzed.

3.2.4 Boundary conditions

The governing equations need to be completed by proper *boundary conditions*, a set of additional constraints which determine the particular solutions to be obtained. In literature many approaches in prescribing boundary conditions can be found. In studies involving aortas, phase-contrast MRI (magnetic resonance imaging) is typically used to obtain concurrently vascular geometries and *in vivo* 4D velocity profile [35], [36]. Measuring coronary flow by means of phase-contrast MRI is challenging because a high spatial resolution is required and to date, only few clinical applications have been reported. Consequently, other techniques are used [37]. In a recent study conducted on 30 reconstructed coronary arteries (10 RCA, 10 LAD, and 10 LCX), both inflow and outflow conditions were prescribed according to *in vivo* doppler velocity measurements, which represents an accurate method to obtain personalized coronary artery computational models [26]. Doutel et al. to investigate atherosclerosis development, mixed and *in silico* to *in vitro* experiment designing a methodology combining CFD simulations and μ PIV (micro Particle Image Velocimetry). For the numerical case, the fluid velocity was set at the inlet using the mean velocity derived by the Hagen-Poiseuille's law whereas for outflow boundary conditions the flow partition Murray's law (later described) was used [38]. Since the typical approach to calculate flow rate with doppler velocity measurements consists in measuring the maximum velocity and in estimating the mean velocity assuming parabolic profile, which is an unrealistic situation, Ponzini et al. proposed a different way for estimating the flow rate regarded as a function of maximum velocity and Womersley number. Such law represents a valid alternative to setting the inlet boundary condition using Hagen-Poiseuille's law whose fundamental hypothesis are always unverified for the cardiovascular case [39]. Unlike the others previously mentioned, Kim et al. imposed outlet boundary conditions using

a lumped parameter vascular bed model representing the impedance of downstream coronary vascular networks absent in the computational domain [40].

4 From clinical image to numerical results

4.1 Imaging and 3D vessel reconstruction

The advent of high-resolution imaging techniques allows to obtain information about anatomy of blood vessels in a non-invasive or mini-invasive way. By employing this information, it is possible to model hemodynamics based on models with realistic geometry. Since geometry has a strong impact on hemodynamics, the procedure used to model the geometry of a blood vessel from medical images plays a fundamental role in determining the robustness of hemodynamic predictions and their clinical significance[5].

In this study, 6 subjects that underwent invasive coronary cineangiography after heart transplant with no sign of atherosclerosis were considered. Clinical images of their left circumflex coronary artery have been acquired at Città della Salute e della Scienza hospital (Turin, Italy) using the monoplane X-ray system Allura Xper (Philips Medical System, Amsterdam, The Netherlands). The three-dimensional geometrical models were reconstructed with the commercial software QAngio XA Bifurcation RE (Medis Medical Imaging Systems, Leiden, The Netherlands) using two end-diastolic angiographic projections, with a minimum angle of 25° between them. The main branch was segmented and reconstructed considering one side branch per time with a diameter greater than 1 mm obtaining a model for each side branch. After that a smoothing process is performed via the Vascular Modeling Toolkit (VMTK), an open source software based on VTK and ITK libraries and composed by a collection of libraries and tools for 3D reconstruction, geometric analysis, mesh generation and surface data analysis from biomedical images. In order to obtain a model provided with all side branches, the Voronoi diagram computed over each bifurcation were combined in

a single diagram leading to joined centerlines³ of the vessel. From now on, all the presented visualizations were obtained using the open-source software ParaView.

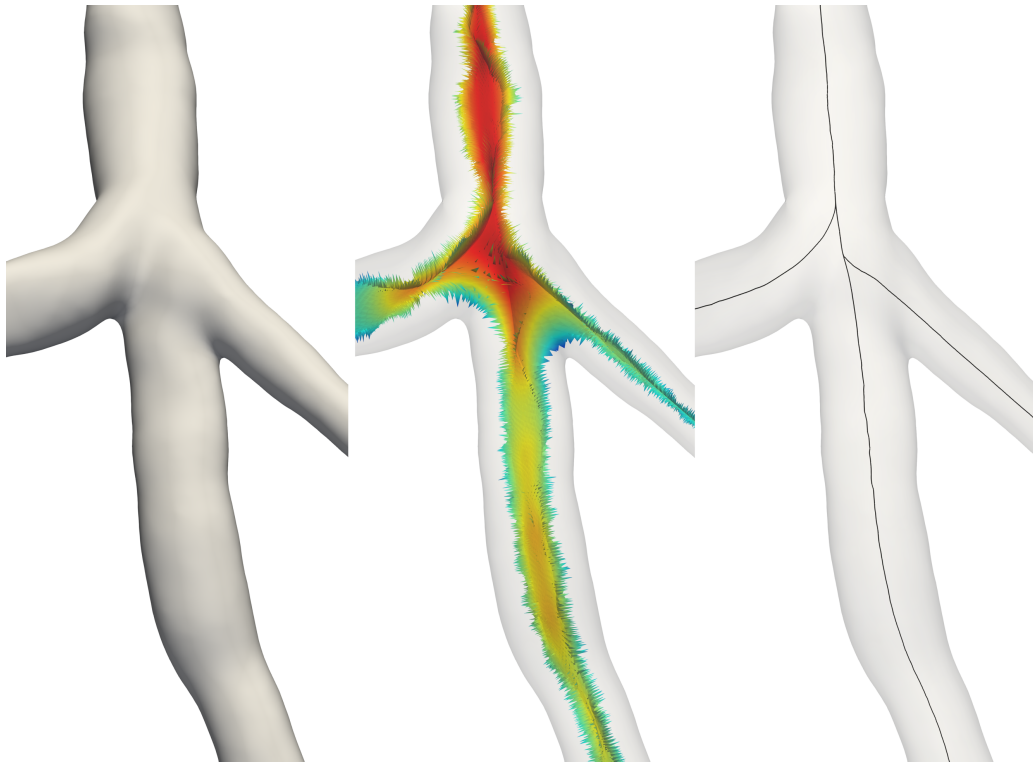


Figure 4.1 Reconstructed 3D model (left) with its Voronoi diagram (center) and centerlines (right)

The Voronoi diagram can be seen as the place where the centers of maximal inscribed spheres are defined. Centerlines are determined as the paths defined on the Voronoi diagram that minimize the integral of the radius of maximal inscribed spheres along the path. This procedure is done by propagating a wave from a source point corresponding to one endpoint of the centerline, using the inverse of the radius as the wave speed. The wave arrival time is recorded for all the points of the Voronoi diagram, and then a line is backtracked from a target point down along the gradient of arrival times [41]. The final results of the reconstruction process are shown in the following figures where each LCX model is identified by an alphanumeric code.

³ Continuous line running through the center of the cross-sectional surface of the vessel

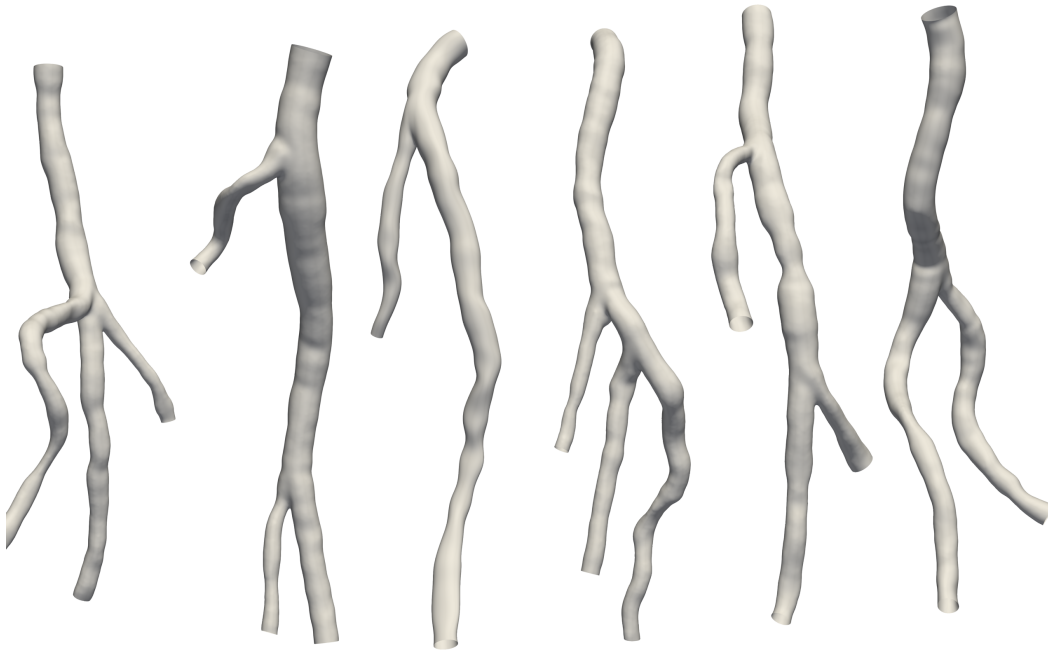


Figure 4.2 Reconstructed LCX coronary models

As can be seen, some models are provided with two side branches whereas others are provided with only one side branch: it comes from the enormous coronary anatomical variability between subjects and as already said, by the fact that only branches with a diameter greater than 1 mm were reconstructed.

4.2 Geometry preparation

Despite the CFD results analysis will be performed on the main branch of the models, side branches must be taken in account since they have a great importance for hemodynamic characterization. On the other hand, in order to reduce the computational cost, the side branches are truncated near to the bifurcation point. To do that, by means of properly coded Python scripts and VMTK, sections located 5 spheres away from each bifurcation were clipped obtaining the following clipped LCX models.

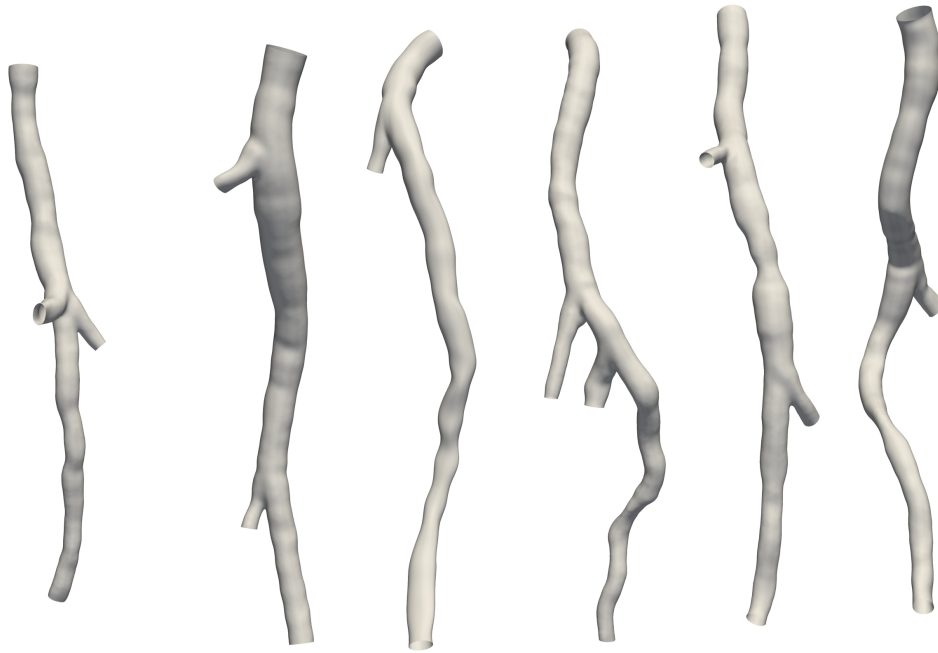


Figure 4.3 LCX coronary clipped models

4.3 Mesh generation

Mesh generation is a crucial stage for patient specific modeling process. The solution accuracy and the processing time are highly influenced by the total number of elements: the higher is the number of elements, the higher are processing time and solution accuracy.

Global mesh setup					Prism parameters	
Scale factor	Max element	Curvature refinement	Min size limit	Refinement	Height ratio	Number of layers
0.16	1.0	enabled	0.4	20	1.1	5

Table 4.1 Main meshing parameters

To do so, the commercial software ANSYS ICEM CFD (Ansys Inc, USA) was used. First of all, curves were extracted in order to generate inlet and outlet

surfaces and then a body representing the blood was created within the model. In order to discretize the volume of interest different type of elements can be used. For all the considered models, a hybrid unstructured mesh characterized by tetrahedral elements and 5 layers of prismatic elements at wall boundaries was generated, this allows to better describe the physical behaviour near the vessel wall. The unstructured mesh has been generated using the *Octree method* which is basically rely on the divide-and-conquer principle: starting from a single element, each element is iteratively divided in smaller element until some criterion is satisfied. Such method is fast, conceptually simple and works reasonably well [32].

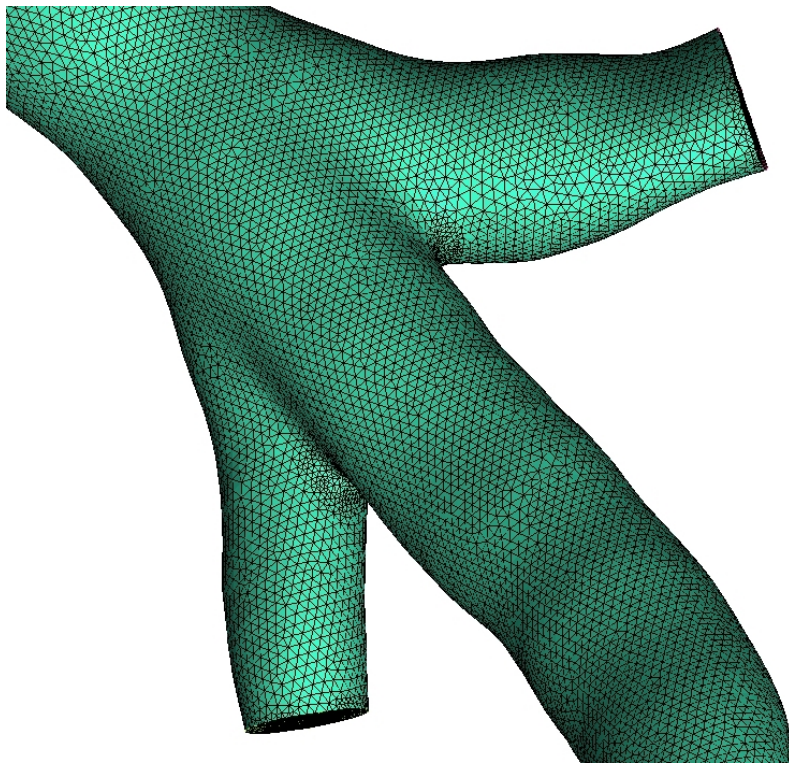


Figure 4.4 Bifurcation zone of a meshed LCX model

Once mesh is computed, a smoothing process was performed with to improve mesh quality. Such process is able to move and merge nodes, and even to delete some elements if it necessary to improve the quality of the mesh. In the end an output file was properly prepared, needed to the solving software to carry out the simulation. The following figures depicts some mesh details.

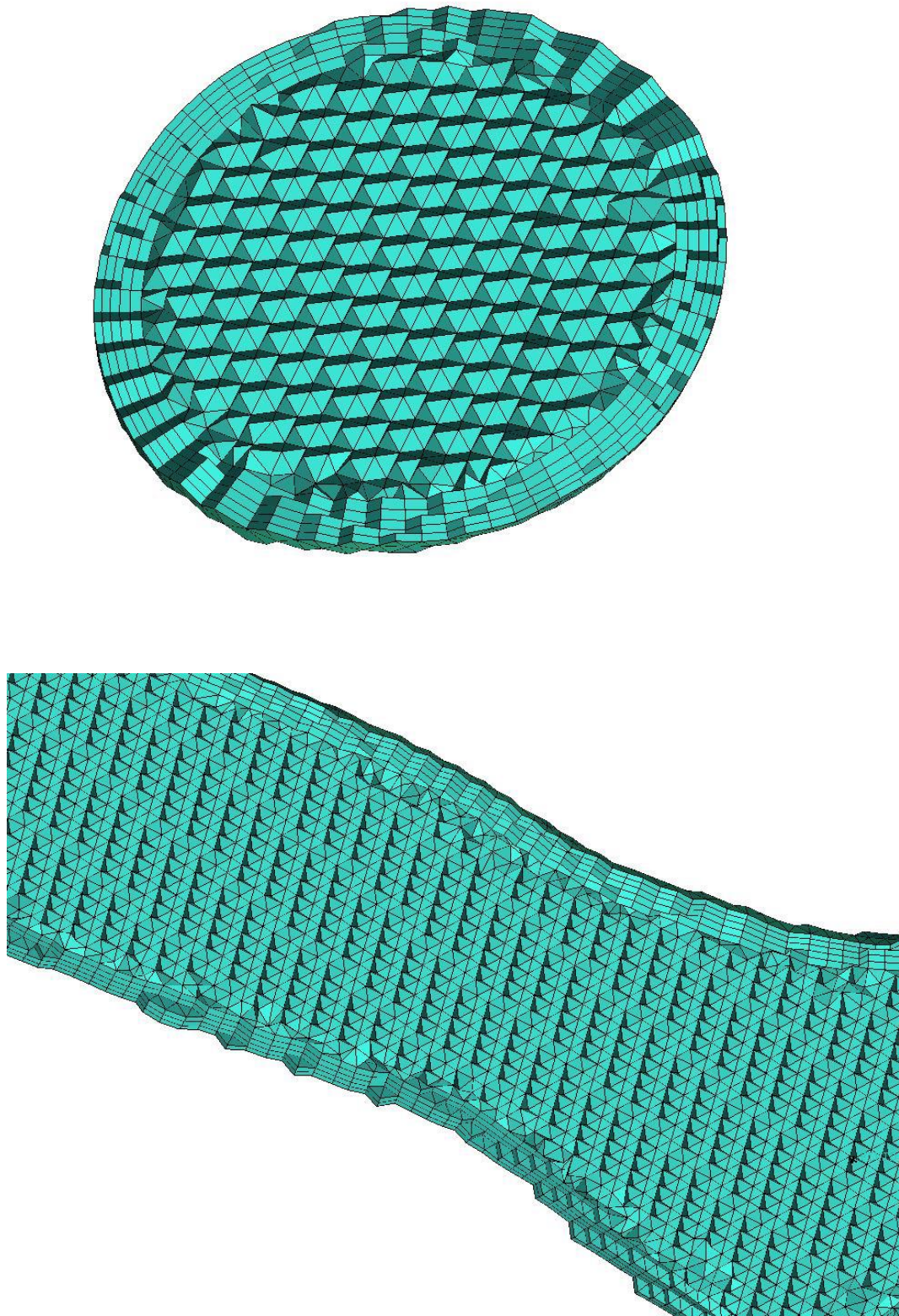


Figure 4.5 Cross-sectional (Top) and transversal (Bottom) mesh cut plane

4.4 Mathematical model

The mathematical equations of fluid dynamics are the key components of hemodynamics modeling. The blood flow is governed by the Navier-Stokes equations for an incompressible fluid, widely discussed in paragraph 2.1.1, and rewritten below.

$$\begin{cases} \rho \frac{D\vec{v}}{Dt} = -\nabla p - \nabla \cdot \bar{\tau} + \rho \vec{g} \\ \nabla \cdot \vec{v} = 0 \end{cases} \quad 4.1$$

The vessel wall was assumed to be rigid and with no-slip conditions at the wall. Blood was treated as a non-Newtonian fluid according the Carreau model

$$\mu(\dot{\gamma}) = \mu_{\infty} + (\mu_0 - \mu_{\infty}) [1 + (\lambda \dot{\gamma})^2]^{\frac{n-1}{2}} \quad 4.2$$

and the following parameters was used:

Density ρ	Infinite shear rate limit viscosity μ_{∞}	Zero shear rate limit viscosity μ_0	Relaxation time constant λ	Power law index n
1060 $\frac{kg}{m^3}$	0.0035 $\frac{kg}{m \cdot s}$	0.25 $\frac{kg}{m \cdot s}$	25 s	0.25

Table 4.2

Steady-state simulations were carried out using the software ANSYS Fluent (Ansys Inc., USA) based on the finite volume method.

4.5 Inflow conditions

In order to determine the ingoing flow rate, the following empirical law which relates the average hydraulic diameter to the flow rate, derived by van der Giessen et al. [42], was used:

$$q = 1.43 \cdot d^{2.55} \quad 4.3$$

where q is the flow rate expressed in $\frac{m^3}{s}$ and d is the hydraulic diameter in meters. Then for each model, 11 velocity profiles were generated in Python by means of analytical formulations, considering three-dimensional features such as secondary flow and peak displacement from the geometric centre of inlet surface. The through-plane components expressed in cylindrical coordinates (n, r, θ) were computed as follows:

$$\vec{v}_n(r, \theta) = \left\{ \left[1 - \left(\frac{r}{R} \right)^2 \right] + s \left[\left(\frac{r}{R} \right)^3 - \left(\frac{r}{R} \right) \right] \cos(\theta) \right\} \vec{u}_n \quad 4.4$$

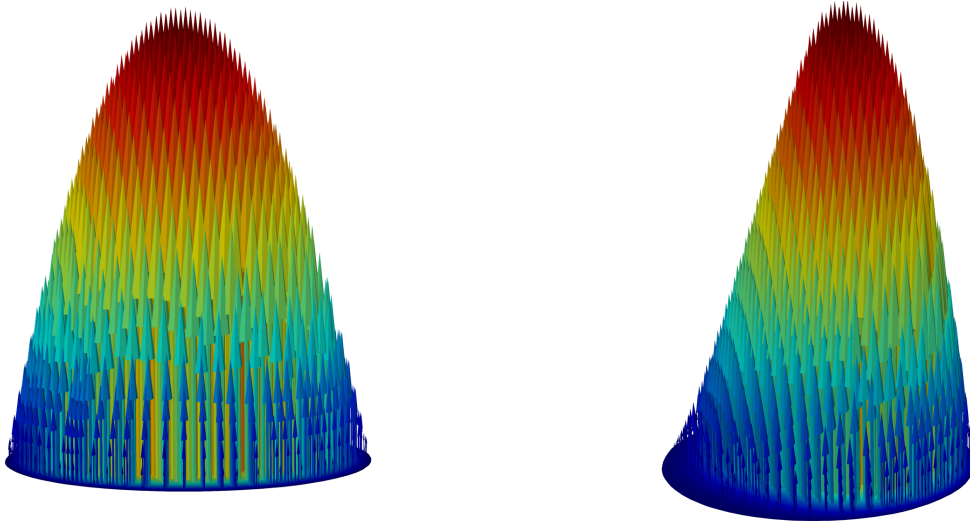


Figure 4.6 Through-plane components. From left to right: parabolic ($s=0$), skewed-peak parabolic ($s=1$)

As for the in-plane components, two different formulations were used taking in account the number of vortices:

- One vortex

$$\vec{v}_\vartheta(r, \theta) = \left(\frac{r}{R}\right) \left[1 - \left(\frac{r}{R}\right)^2\right] \vec{u}_\vartheta \quad 4.5$$

$$\vec{v}_r(r, \theta) = 0 \quad 4.6$$

$$\vec{v}_{ip}(r, \theta) = k \frac{\vec{v}_\vartheta(r, \theta) + \vec{v}_r(r, \theta)}{|\vec{v}_\vartheta(r, \theta) + \vec{v}_r(r, \theta)|_{mean}} (\vec{v}_n \cdot \vec{u}_n)_{mean} \quad 4.7$$

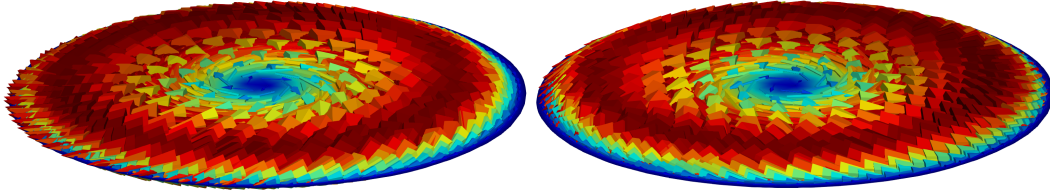


Figure 4.7 One vortex in-plane components. From left to right: clockwise ($k=0.25$), anti-clockwise ($k=-0.25$)

- Two vortices

$$\vec{v}_\vartheta(r, \theta) = \left[1 - \left(\frac{r}{R(\theta)}\right)^2\right] \left[4 - 23 \left(\frac{r}{R(\theta)}\right)^2 + 7 \left(\frac{r}{R(\theta)}\right)^4\right] \cos(\vartheta) \vec{u}_\vartheta \quad 4.8$$

$$\vec{v}_r(r, \theta) = \left[1 - \left(\frac{r}{R(\theta)}\right)^2\right]^2 \left[4 - \left(\frac{r}{R(\theta)}\right)^2\right] \sin(\vartheta) \vec{u}_r \quad 4.9$$

$$\vec{v}_{ip}(r, \theta) = k \frac{\vec{v}_\vartheta(r, \theta) + \vec{v}_r(r, \theta)}{|\vec{v}_\vartheta(r, \theta) + \vec{v}_r(r, \theta)|_{mean}} (\vec{v}_n \cdot \vec{u}_n)_{mean} \quad 4.10$$

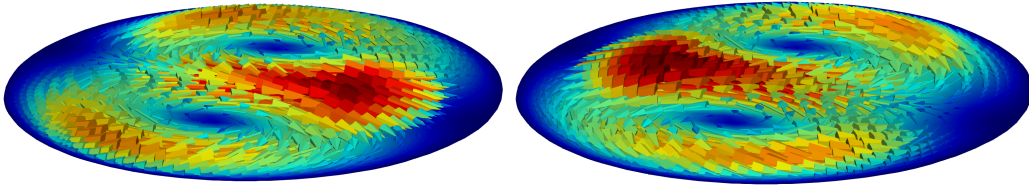


Figure 4.8 Two vortices in-plane components. From left to right: clockwise ($k=0.25$), anti-clockwise ($k=-0.25$)

In the end, the following 3D custom velocity profiles were obtained:

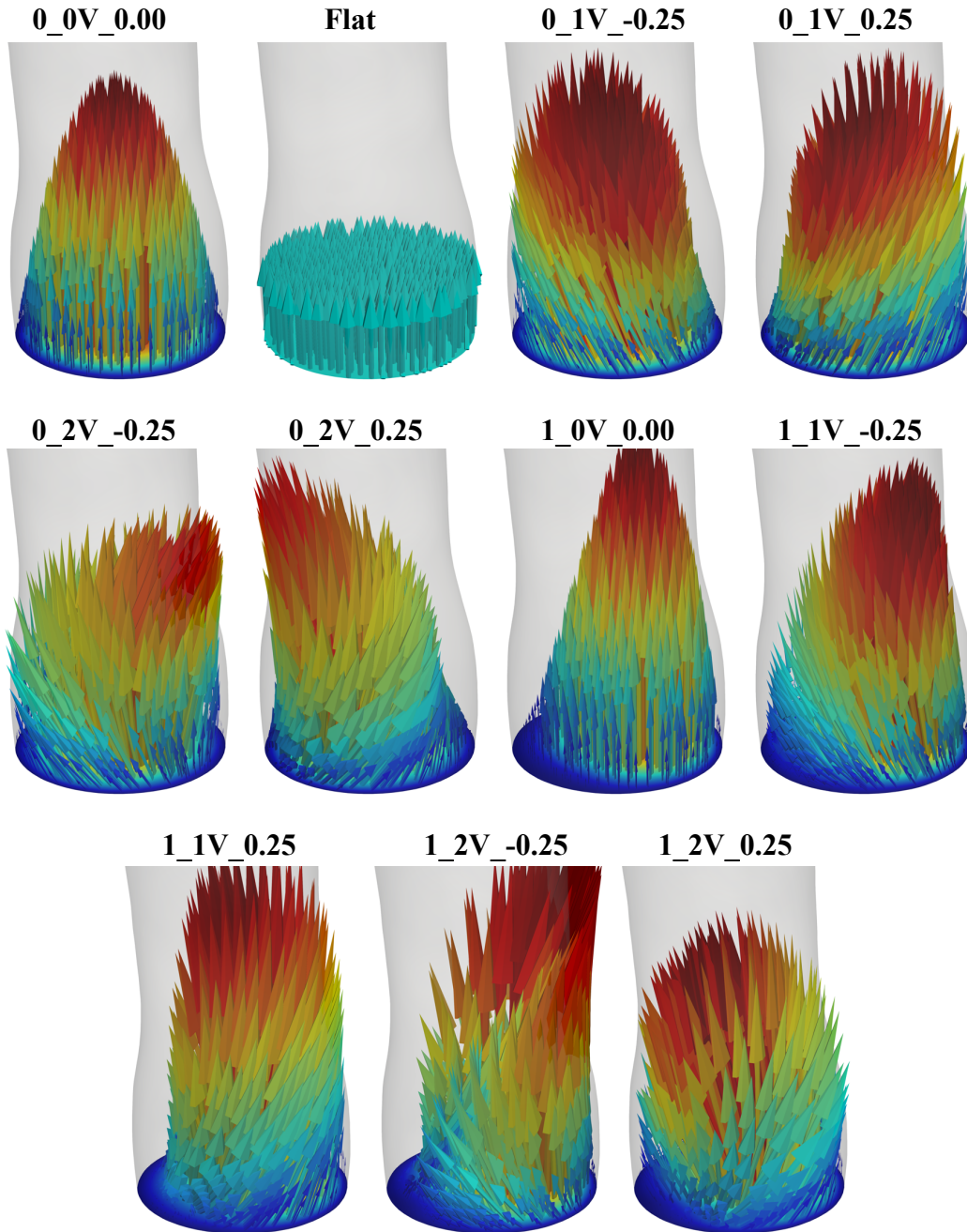


Figure 4.9 3D custom velocity profiles

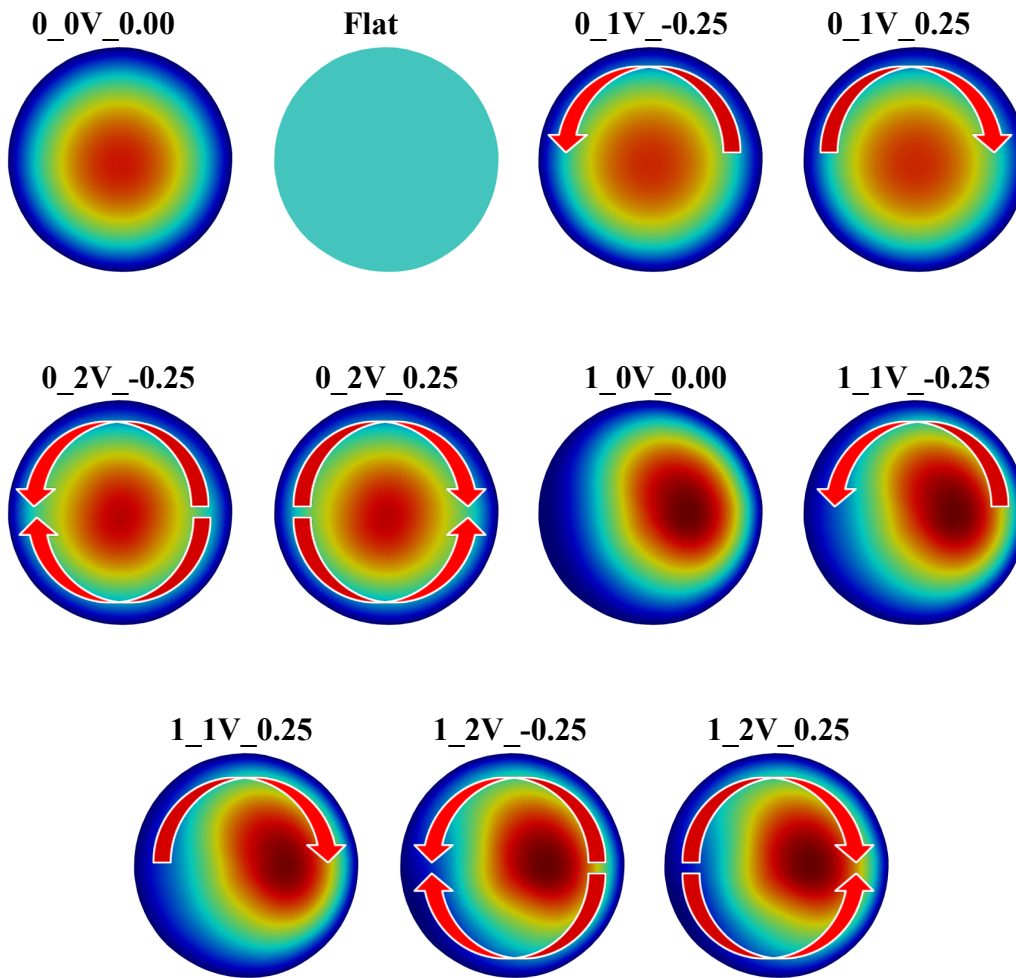


Figure 4.10 Top view of custom velocity profiles

Except for “Flat” profile which consists of the mean velocity magnitude along all the inlet surface, each custom profile was identified by a code having the form:

$$s_nV_k$$

where:

- s is 0 (1) if the peak of the velocity profile is centered (skewed) with respect to the inlet surface’s centroid
- n represents the number of vortices lying on the inlet surface
- k is +0.25 (-0.25) if vortices rotate clockwise (anti-clockwise)

Therefore, for each coronary model 11 different numerical simulations have been performed, totalling 66 simulations in all.

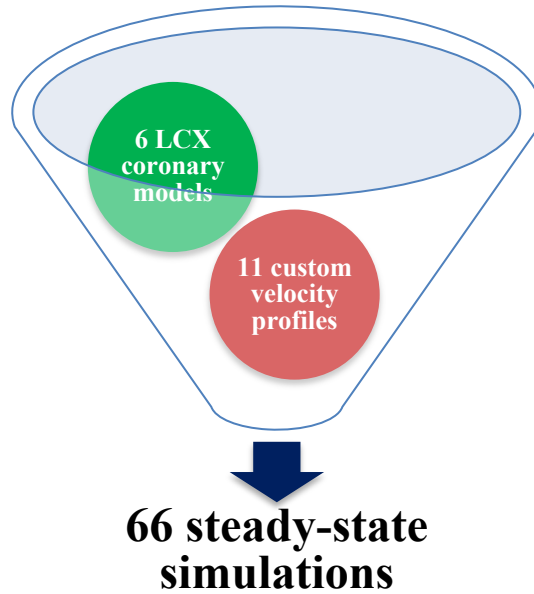


Figure 4.11 Sketch of the amount of simulations performed

4.6 Outflow conditions

As for the outlets, the flow ratio to the side branches were prescribed using the empirical relation derived by van der Giessen et al. [42]:

$$\frac{q_{b_2}}{q_{b_1}} = \left(\frac{d_{b_2}}{d_{b_1}} \right)^{2.27} \quad 4.11$$

based on the well-known Murray's law:

$$\frac{q_{b_2}}{q_{b_1}} = \left(\frac{d_{b_2}}{d_{b_1}} \right)^3 \quad 4.12$$

where q_{b_1} and q_{b_2} are the flow rates through two different branches and d_{b_1} and d_{b_2} their diameters. Since Murray's law seems to underestimate flow rate through

side branches, the equation 4.11 was preferred. The used algorithm computes the flow through each branch as a percentage of the flow rate prescribed at the inlet. As a result, flow splits were obtained:

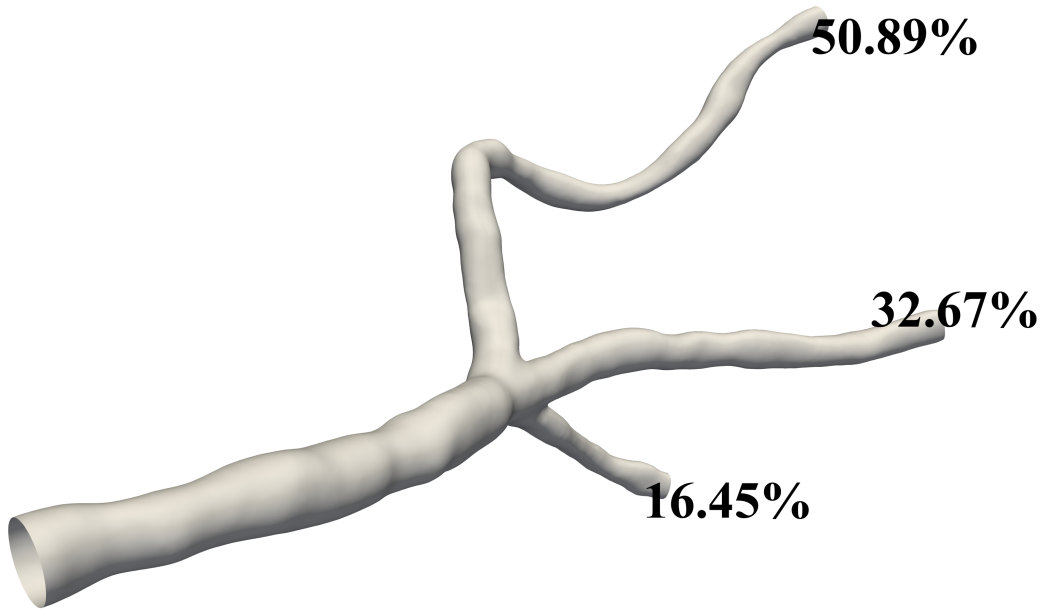


Figure 4.12 Example of flow split

4.7 Sensitivity analysis

The last step before proceeding with the numerical simulations was to carry out a sensitivity analysis aiming to understand if the results obtained with clipped models would differ with respect to those obtained with original models. To do so, the P23 LCX model and P23 LCX clipped model were both meshed as described in paragraph 4.3.

	P23 LCX	P23 LCX clipped	Percentage difference
Total elements	2125032	1651282	22,3%
Total nodes	548060	420283	23,3%

Table 4.3 Original and clipped model mesh features

As can be seen in the table above, there is a significant difference of total elements and total nodes between the two meshes, which leads to savings in terms of computational cost. For both models, a “Flat” velocity profile was prescribed at the inlet whereas outflow conditions based on equation 4.11 were prescribed at the outlets.

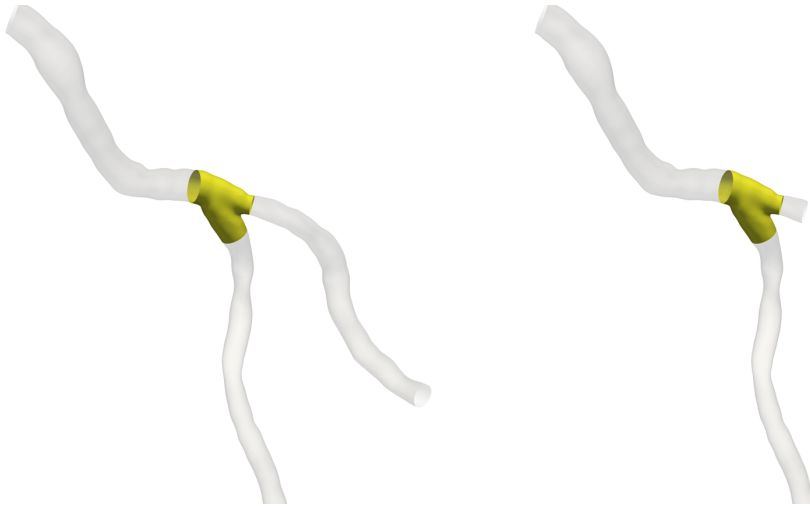


Figure 4.13 (Left) Shaded P23 LCX model and (Right) Shaded P23 LCX clipped model with highlighted bifurcations

Once isolated the bifurcation by clipping branches’ surfaces located more than 2 spheres away, the averaged wall shear stress (AWSS) was computed for both the bifurcations obtaining the following values:

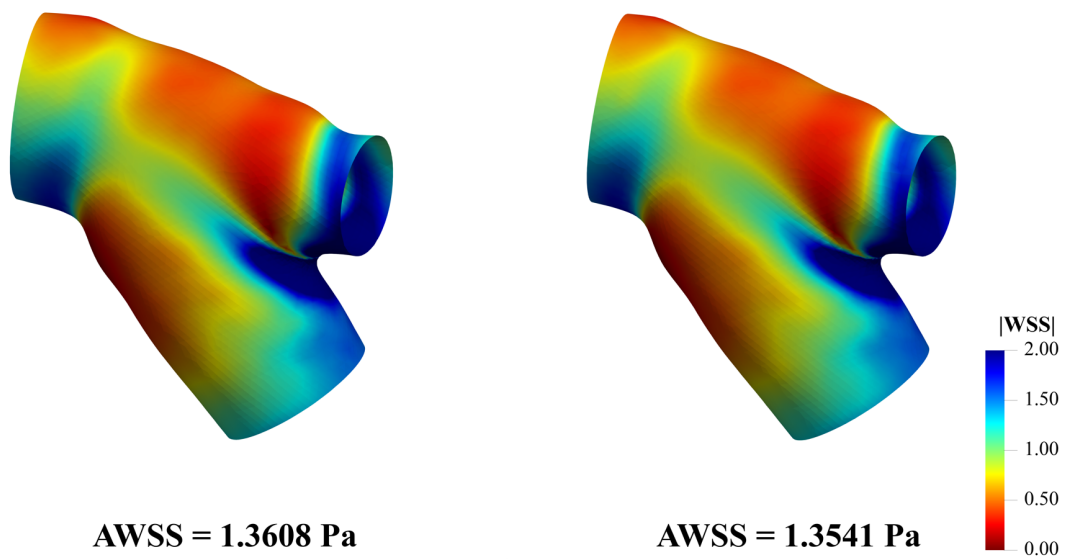


Figure 4.14 |WSS| color map for P23 model (Left) and P23 clipped model (Right)

where the AWSS was intended as:

$$AWSS = \frac{1}{n} \sum_{i=1}^n |\overrightarrow{WSS}_i| \quad 4.13$$

Since the percentage difference between the two values is 0.49%, it can be assumed that there are no differences.

4.8 Hemodynamic descriptors and data analysis

In order to evaluate the simulations' results, some hemodynamic descriptors have been considered and processed. Even though the American Heart Association (AHA) wrote a segmental classification for LCX coronary arteries based on some anatomical features, in this case a custom-made classification was used calling *proximal segment* the main branch part until the first bifurcation whereas all the main branch remaining portion was called *distal segment* (Figure 4.15). Then, since the conducted study aims to evaluate possible differences in hemodynamic behaviour due to the used custom velocity profiles, for each descriptor (x) the absolute percentage difference from the descriptor's value related to the profile "0_0V_0.00" (x_{ref}) has been computed as follows:

$$percentage\ difference = \left| \frac{x - x_{ref}}{x_{ref}} \right| \cdot 100 \quad 4.14$$

The following wall shear stress-based descriptors were used to describe the near-wall physical features. The first one is the *surface averaged wall shear stress* (SAWSS):

$$SAWSS = \frac{1}{Area} \int |\overrightarrow{WSS}| dA \quad 4.15$$

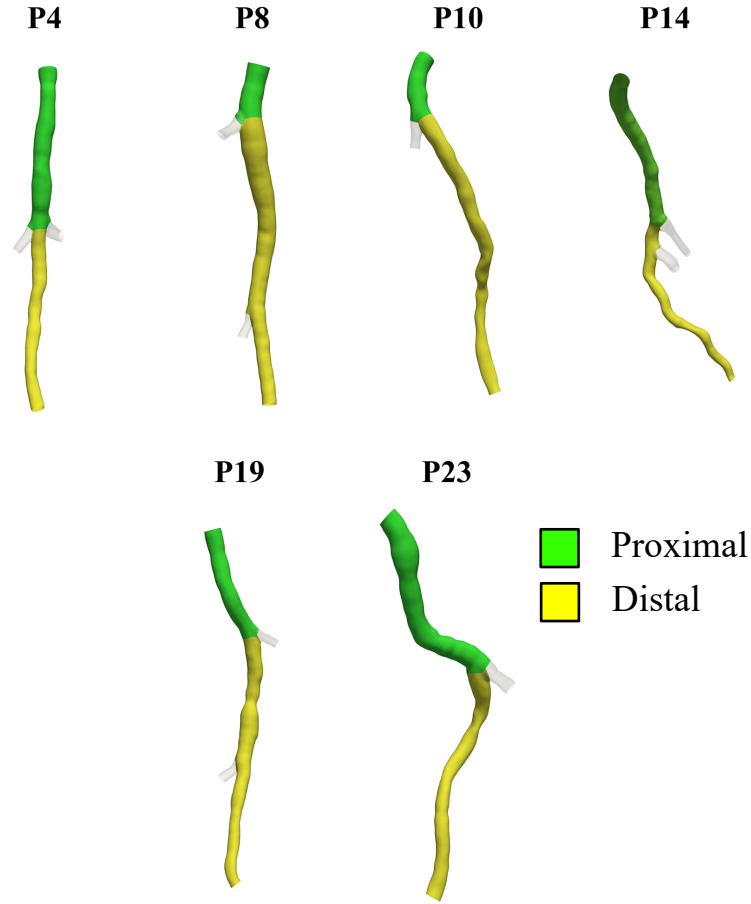


Figure 4.15 LCX classification

Then to analyze the multidirectional nature of WSS, the axial and secondary components of WSS were computed [43]. The axial projection called *axial wall shear stress* (WSS_{ax}) is defined as:

$$\overrightarrow{WSS}_{ax} = \frac{\overline{WSS} \cdot \vec{C}'}{|\vec{C}'|} \frac{\vec{C}'}{|\vec{C}'|} \quad 4.16$$

where \vec{C} represents the centerline of the vessel. The *secondary wall shear stress* (WSS_{sc}) was obtained as the projection of WSS along the direction of vector \vec{S} :

$$\overrightarrow{WSS}_{sc} = \frac{\overline{WSS} \cdot \vec{S}}{|\vec{S}|} \frac{\vec{S}}{|\vec{S}|} \quad 4.17$$

$$\vec{S} = \frac{\vec{C}' \times \vec{R}}{|\vec{C}'| |\vec{R}|}$$

where \vec{S} is the external product of \vec{C}' and vector \vec{R} , directed from the point of application of the centerline to a point on the vessel's surface.

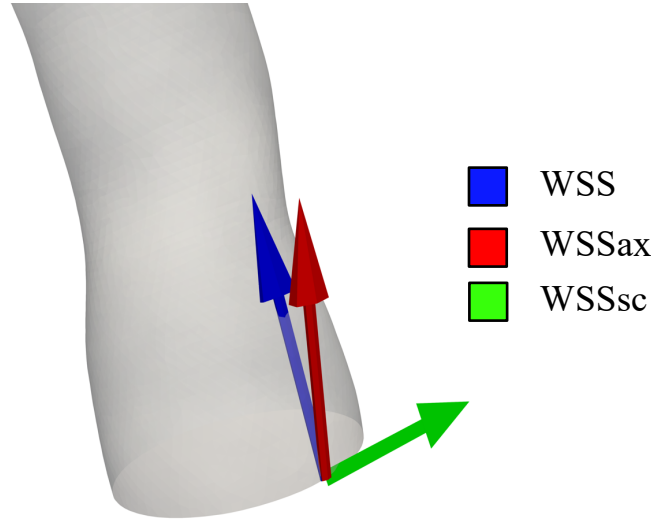


Figure 4.16 Directions of WSS components

Finally, to assess which WSS component prevails, the *wall shear stress ratio* (WSS_{ratio}) was estimated as:

$$WSS_{ratio} = \frac{|\overrightarrow{WSS_{sc}}|}{|\overrightarrow{WSS_{ax}}|} \quad 4.18$$

Even for WSS_{ax} , WSS_{sc} and WSS_{ratio} surface-averaged values were computed. As far as bulk flow is concerned, all the considered descriptors are based on *helicity density* which roughly speaking, gives a measure of alignment of velocity \vec{v} and vorticity $\vec{\omega}$:

$$\vec{h} = \vec{v} \cdot \vec{\omega} \quad 4.19$$

For the visualization of helical flow patterns, the quantity *local normalized helicity* (LNH) has been used [44]:

$$\overline{LNH} = \frac{\vec{v} \cdot \vec{\omega}}{|\vec{v}| |\vec{\omega}|} \quad 4.20$$

which is the cosine of the angle between the velocity and vorticity vectors. Positive (negative) values of LNH indicates the presence of right-handed (left-handed) rotating structures. Instead, to quantitative analyze helical flow structures, the following descriptors were used [44]:

$$h_1 = \frac{1}{T V_i} \iint \vec{h} dV dt \quad 4.21$$

h_1 equals 0 if the flow arrangement consists of two symmetric counter-rotating structures or in case of absence of helicity. Descriptor h_2 is an indicator of the total amount of helical flow in the considered domain irrespective of direction:

$$h_2 = \frac{1}{T V_i} \iint |\vec{h}| dV dt \quad 4.22$$

Then there is h_3 which is a non-dimensional indicator ranging between -1, when there are only left-handed structures, and 1 in the opposite case:

$$h_3 = \frac{h_1}{h_2} \quad 4.23$$

The last descriptor is h_4 , ranging between 0 and 1 defined as:

$$h_4 = |h_3| = \frac{|h_1|}{h_2} \quad 4.24$$

All the calculations discussed in this section were performed combining tailor-made Python scripts and VMTK.

5 Results and discussion

In this chapter, all the obtained results for every single LCX coronary model are presented dividing them into surface results, related to what happens on the vessel wall, and volume results related to the behaviour of bulk flow.

5.1 Surface results

5.1.1 Wall shear stress (WSS)

Firstly, the WSS magnitude related to custom velocity profiles was mapped for each LCX model:

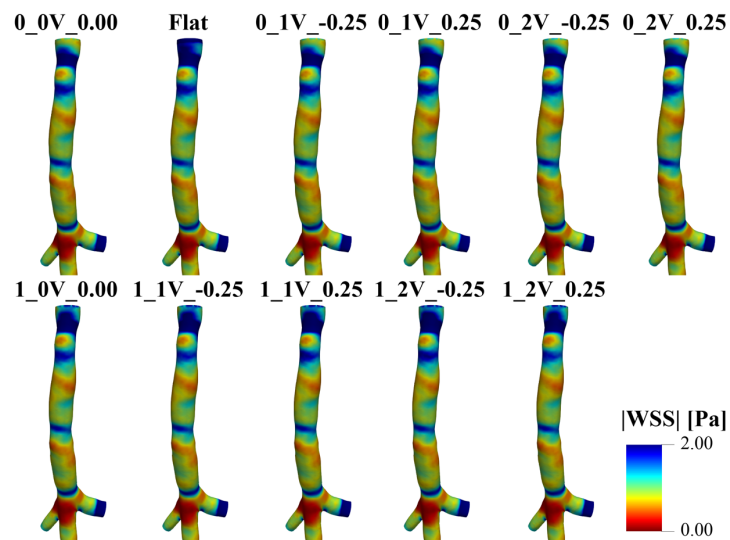


Figure 5.1 P4 |WSS| surface maps

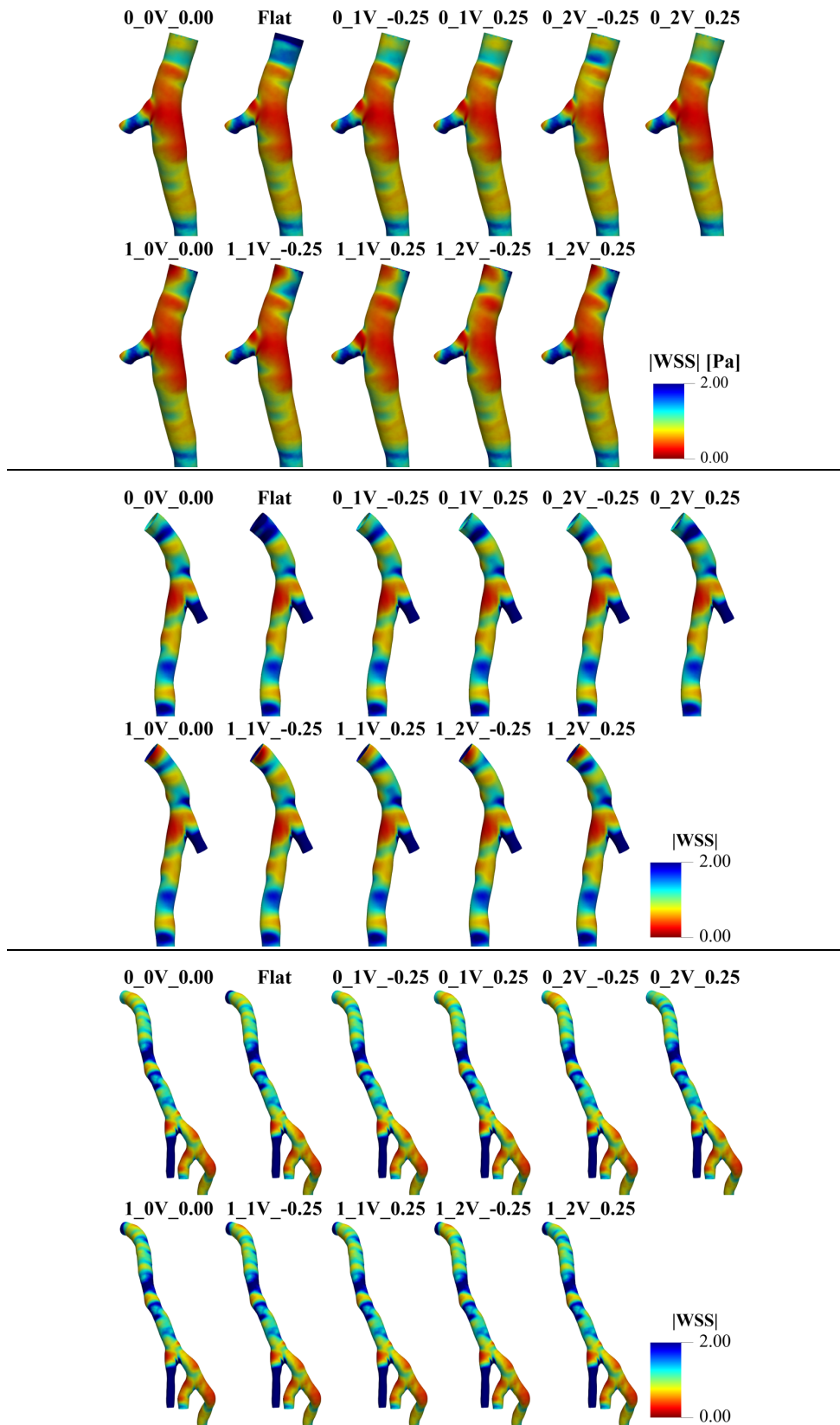


Figure 5.2 P8 (Top), P10 (Middle) and P14 (Bottom) |WSS| surface maps

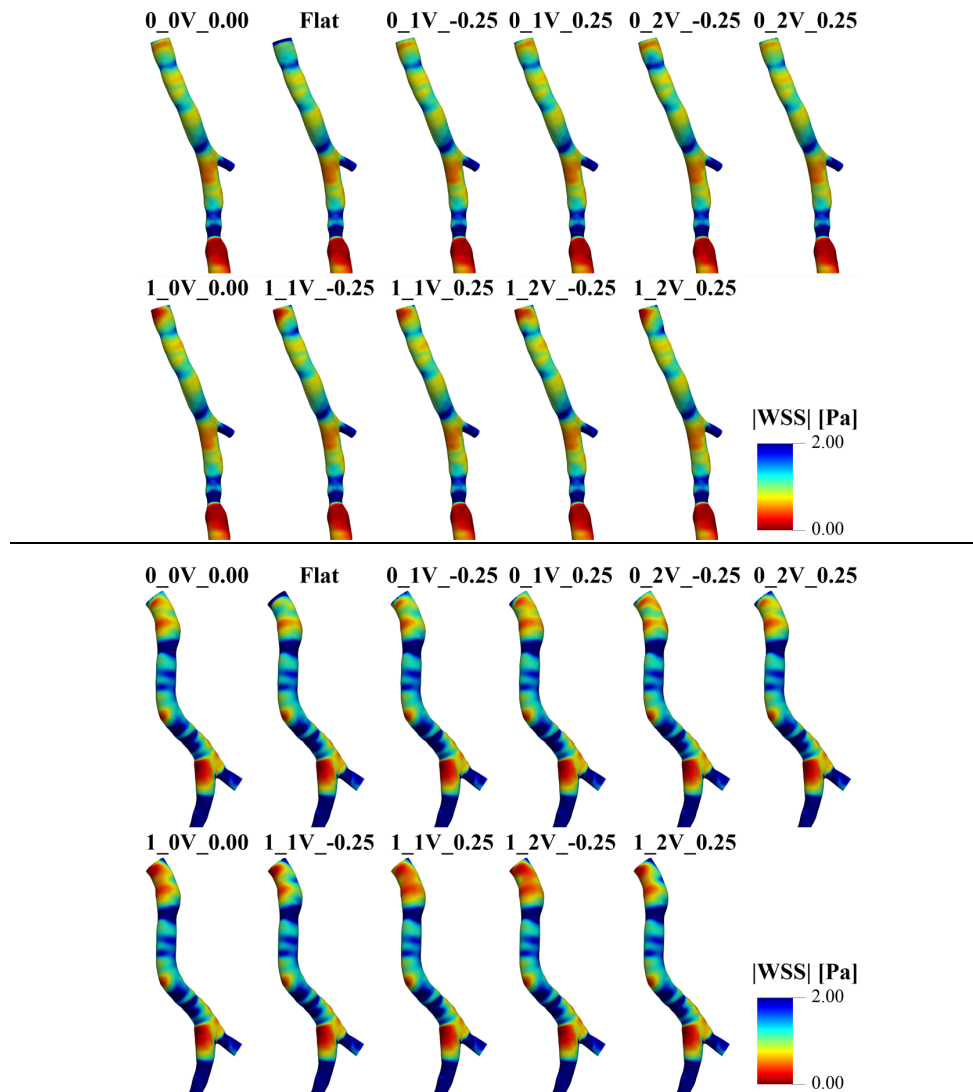


Figure 5.3 P19 (Top) and P23 (Bottom) |WSS| surface maps

To better observe low WSS regions, which coincide with atheroprone regions, the range was selected between 0 and 2 Pa. As expected, all the previously seen WSS magnitude color maps have in common lower values in correspondence of bifurcations and curved tracts, since in those vessel's regions secondary flows usually appear causing a decrease in WSS as already discussed in section 2.6. Furthermore, WSS seems to present more or less the same values among the considered profiles for all the LCX coronary models under consideration. To further quantitatively describe WSS, surface averaged WSS (SAWSS) corresponding to each custom velocity profile prescribed at the inlet surface was computed for the main branch, proximal and distal segment.

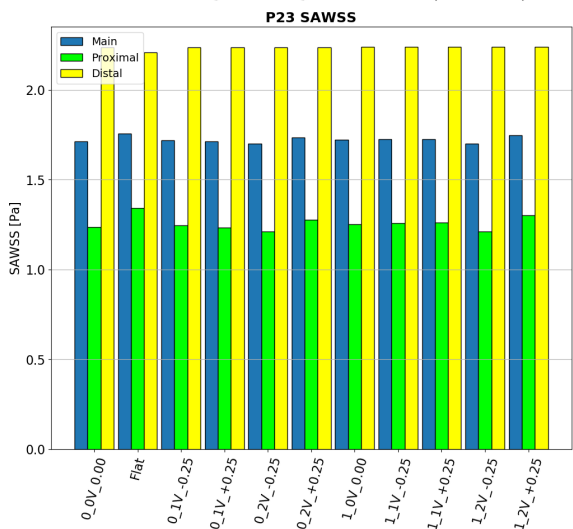
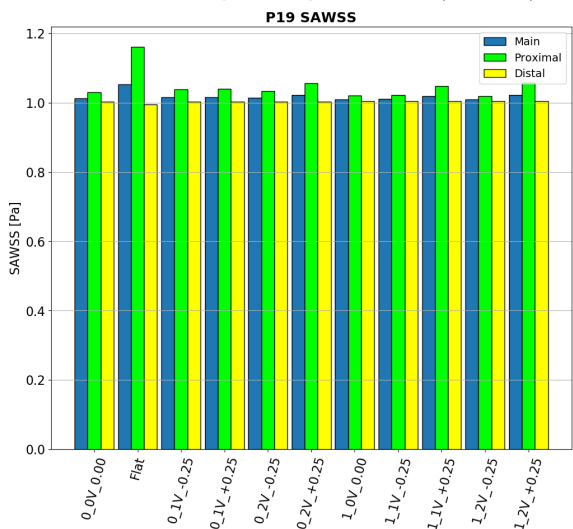
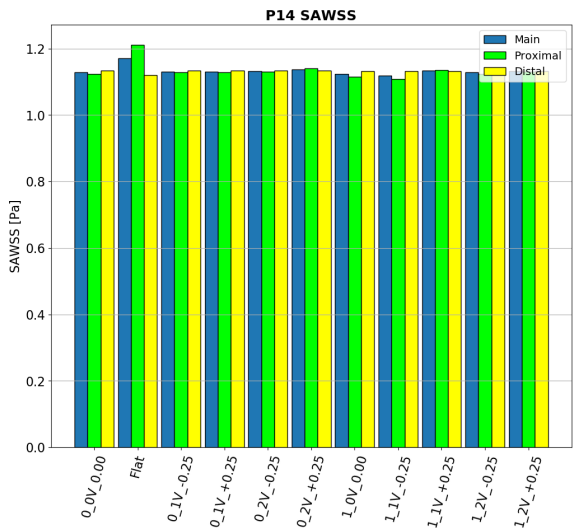
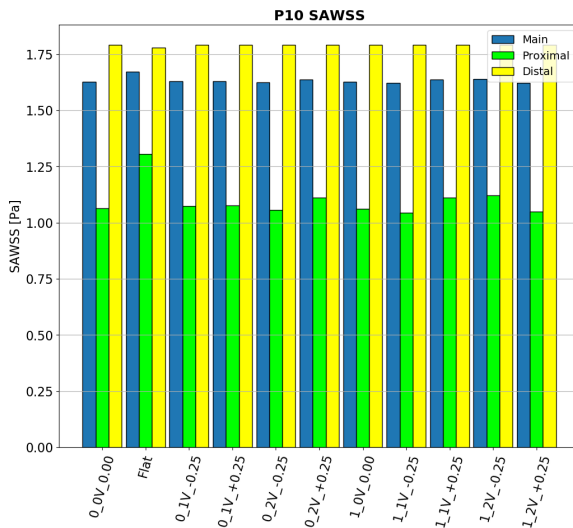
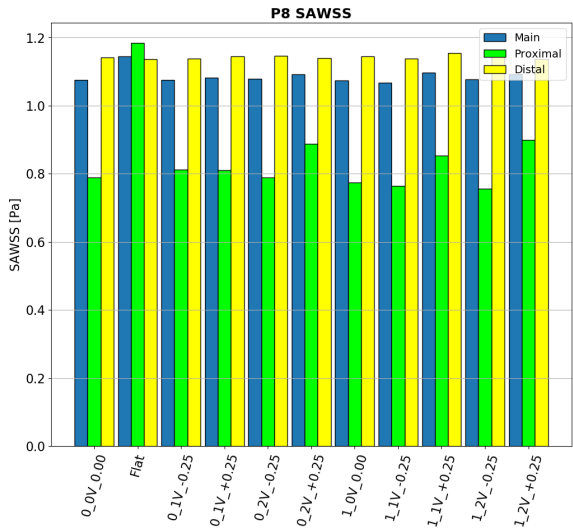
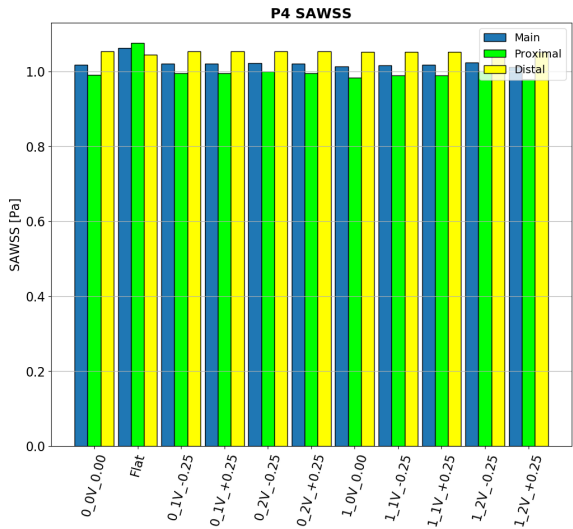


Figure 5.4 Models' SAWSS

As can be seen in the previous bar plots, SAWSS presents values of the same order of magnitude among the custom-made profiles. Models having a more curved inlet regions, present distal segment's values usually greater than those of proximal segment. Then, the percentage differences were computed using a range between 0 and 10% to highlight differences. In the following figures the color map named "0_0V_0.00" represents the reference WSS magnitude surface distribution from which differences were computed.

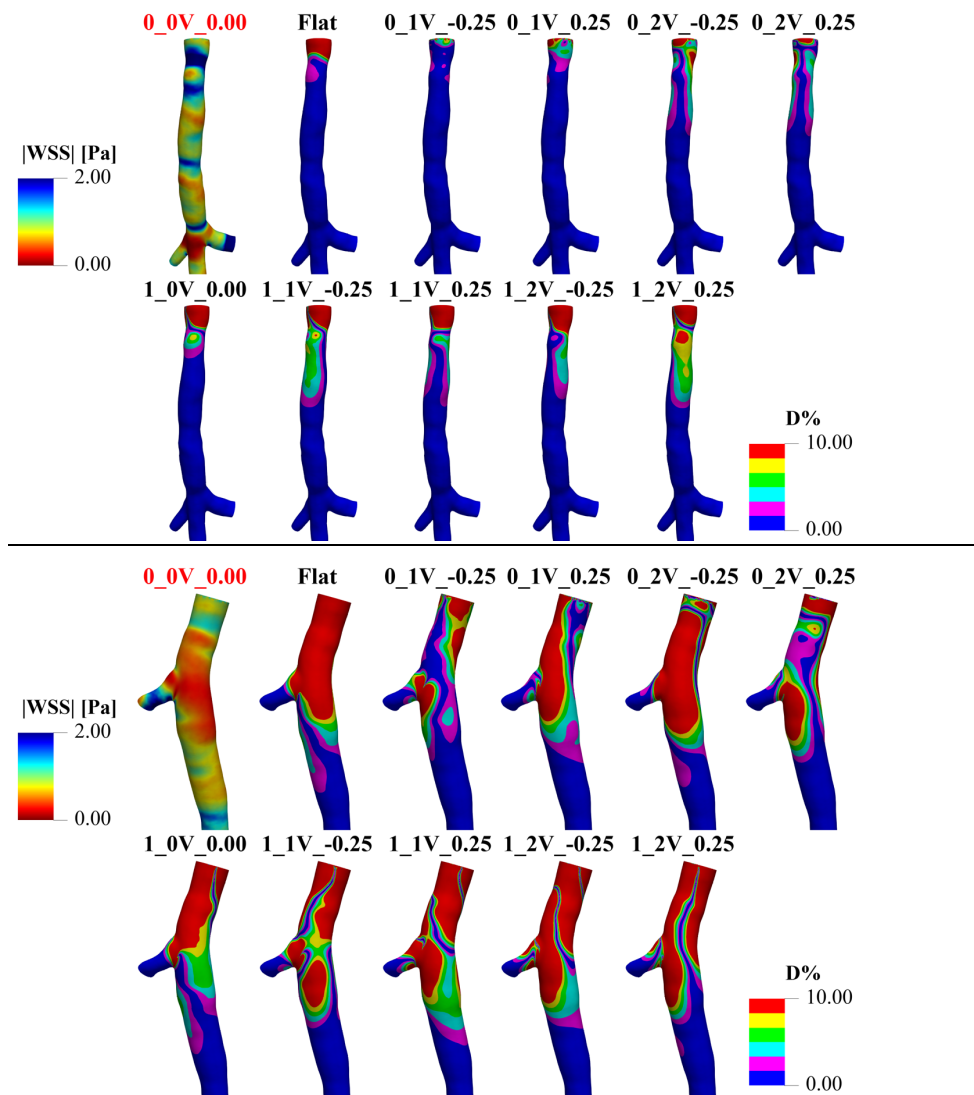


Figure 5.5 P4 (Top) and P8 (Bottom) |WSS| percentage difference surface maps

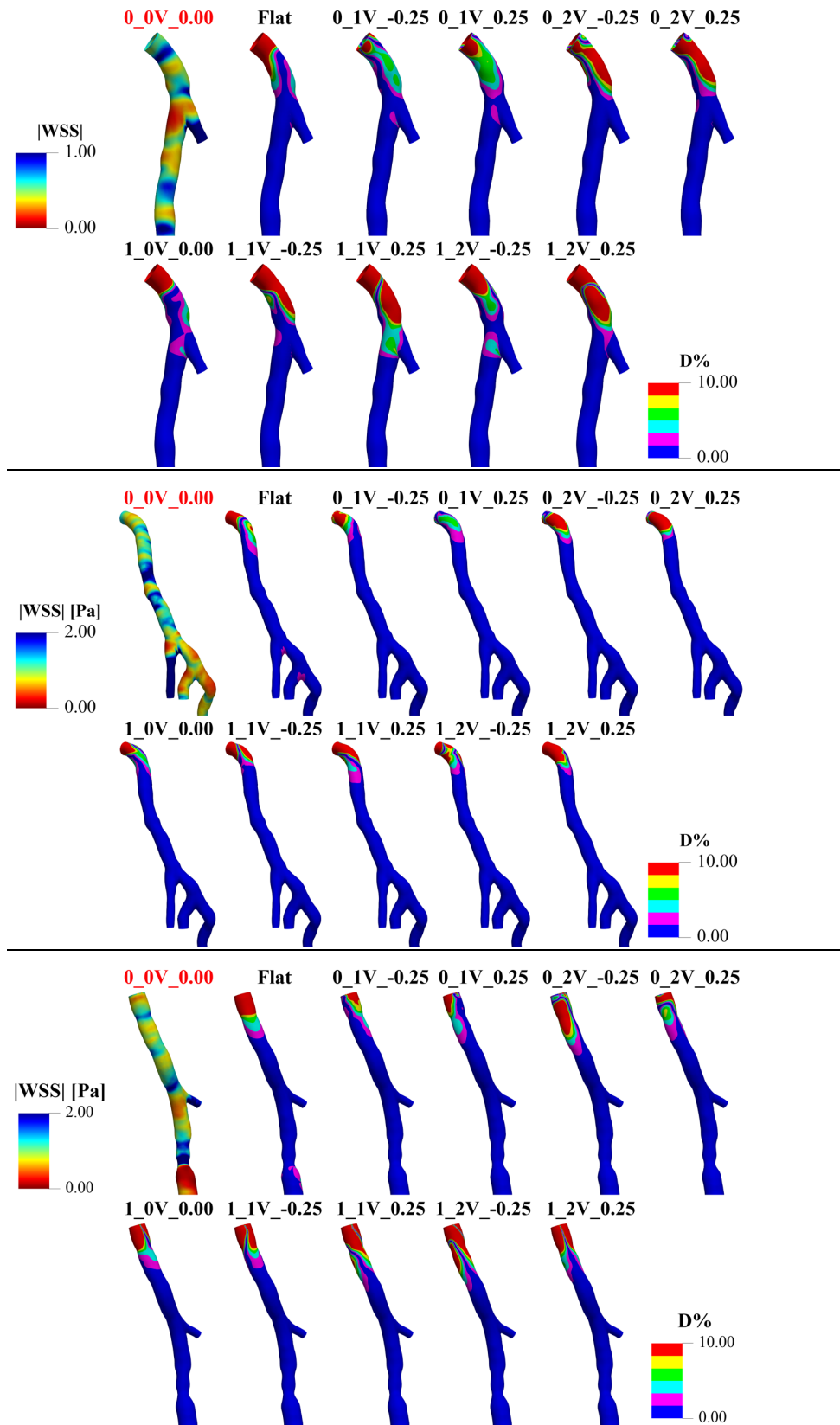


Figure 5.6 P10 (Top), P14 (Middle) and P19 (Bottom) |WSS| percentage difference surface maps

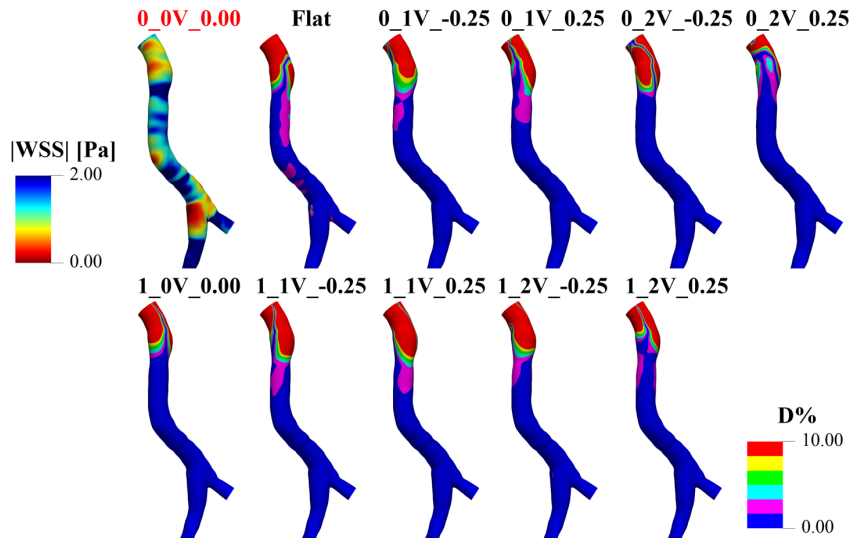


Figure 5.7 P23 |WSS| percentage difference surface maps

From percentage differences surface maps, it can be noticed the same phenomenon for all the examined models: percentage differences from the reference velocity profile are mainly located near the inlet region and after a certain length they decrease steeply to 0%. Such spatial distributions suggest that the shape of velocity profiles influences the WSS results only until a certain distance from the inlet surface, probably due to the disturbance induced by the velocity profile. After that, the hemodynamics settles down and the WSS results are no more influenced by the profile's shape.

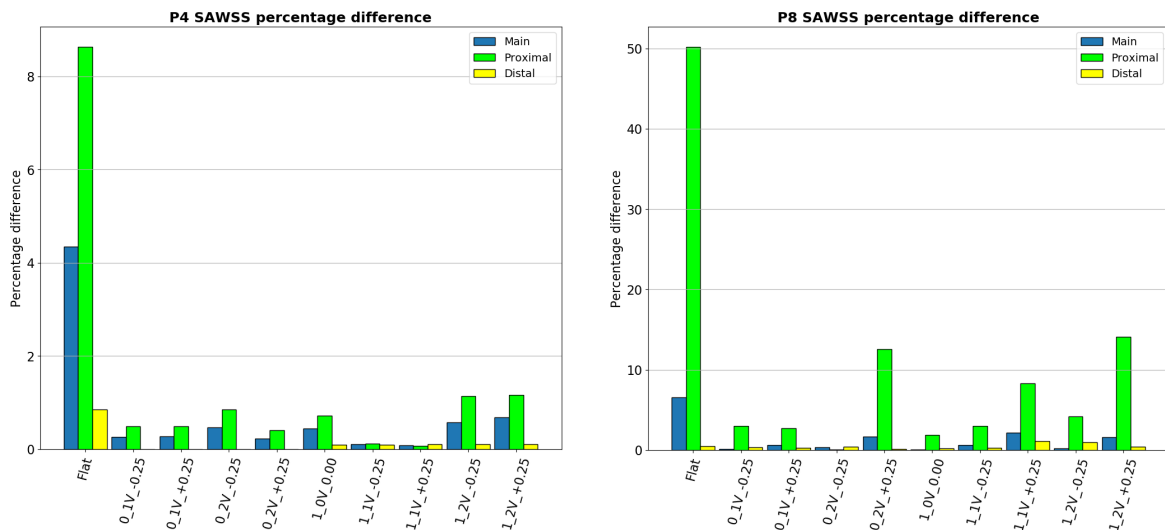


Figure 5.8 Models' SAWSS percentage difference (1)

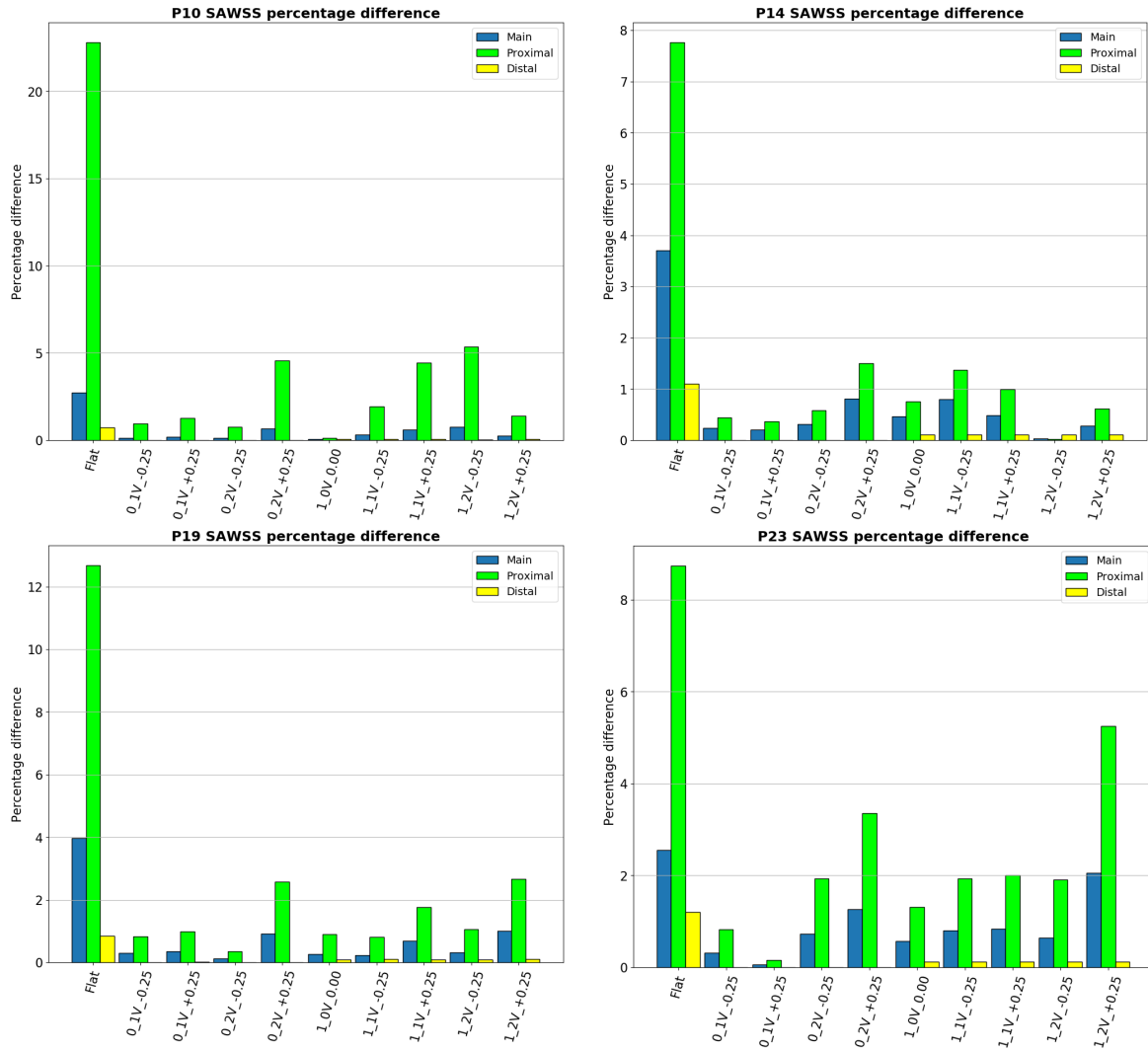


Figure 5.9 Models' SAWSS percentage difference (2)

Surface-averaged WSS percentage difference bar plots show higher differences in proximal segments especially for “Flat” profiles, probably due to its non-physiological shape and its spatial velocity value equal to the average velocity along the whole inlet surface. Such profile presents higher differences in distal segments as well. P8 LCX coronary model shows surface averaged differences even higher than 50% in the proximal segment. In order to summarize the results related to WSS, the following boxplots representing all the considered models distinguishing between the custom-made profiles have been made.

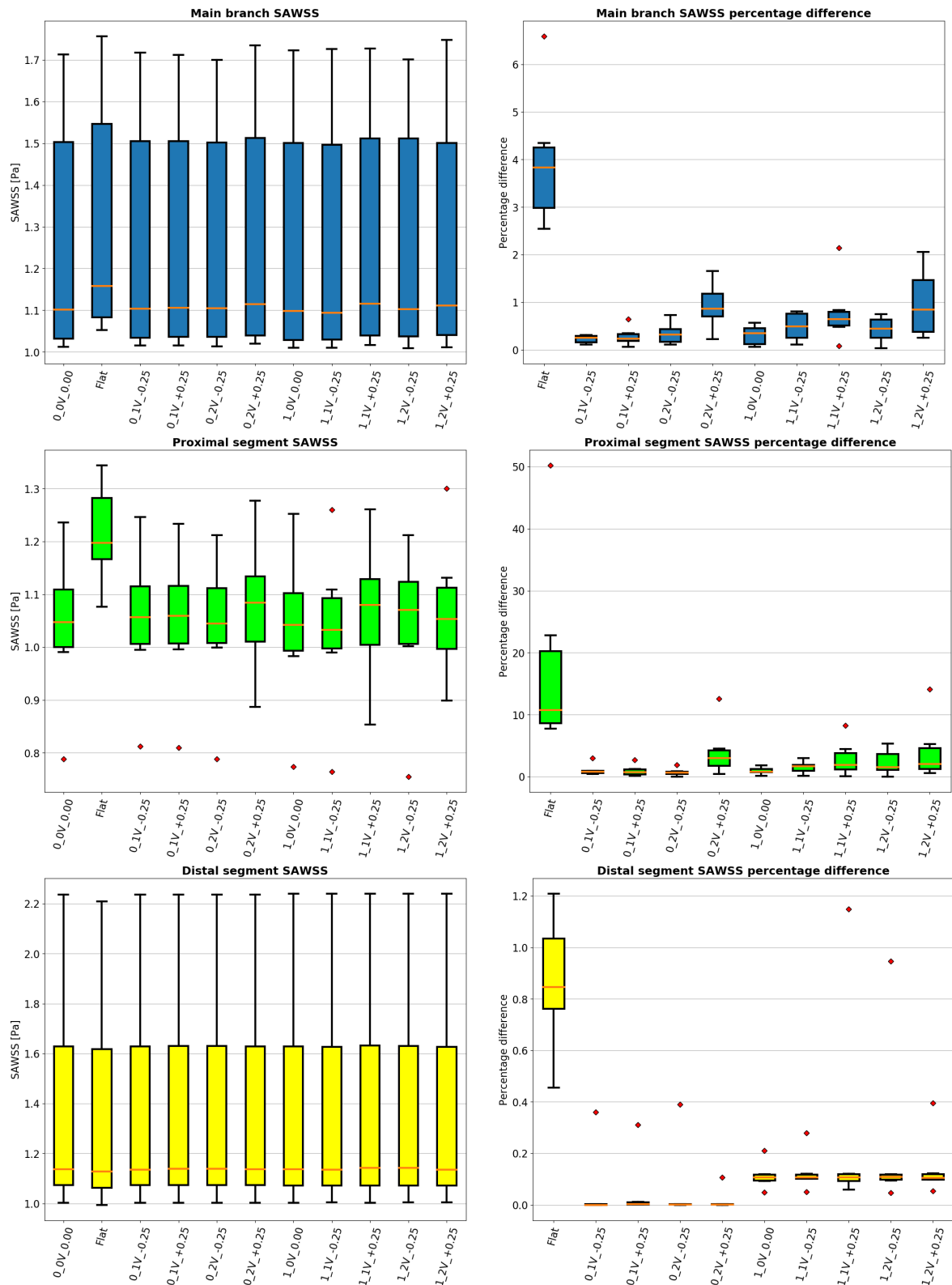


Figure 5.10 WSS summarizing boxplots

Unlike distal segment SAWSS, proximal segment shows a different behaviour related to “Flat” profile which has a higher median and interquartile range. Furthermore, proximal segment’ boxplots present some outliers and variable-length whiskers which means that SAWSS values are differently distributed. The same situation is represented from the percentage difference boxplots where differences are higher for “Flat” profiles and especially in proximal segment.

5.1.2 Axial wall shear stress (WSSax)

The same steps were used to analyze WSSax and WSSsc (discussed later):

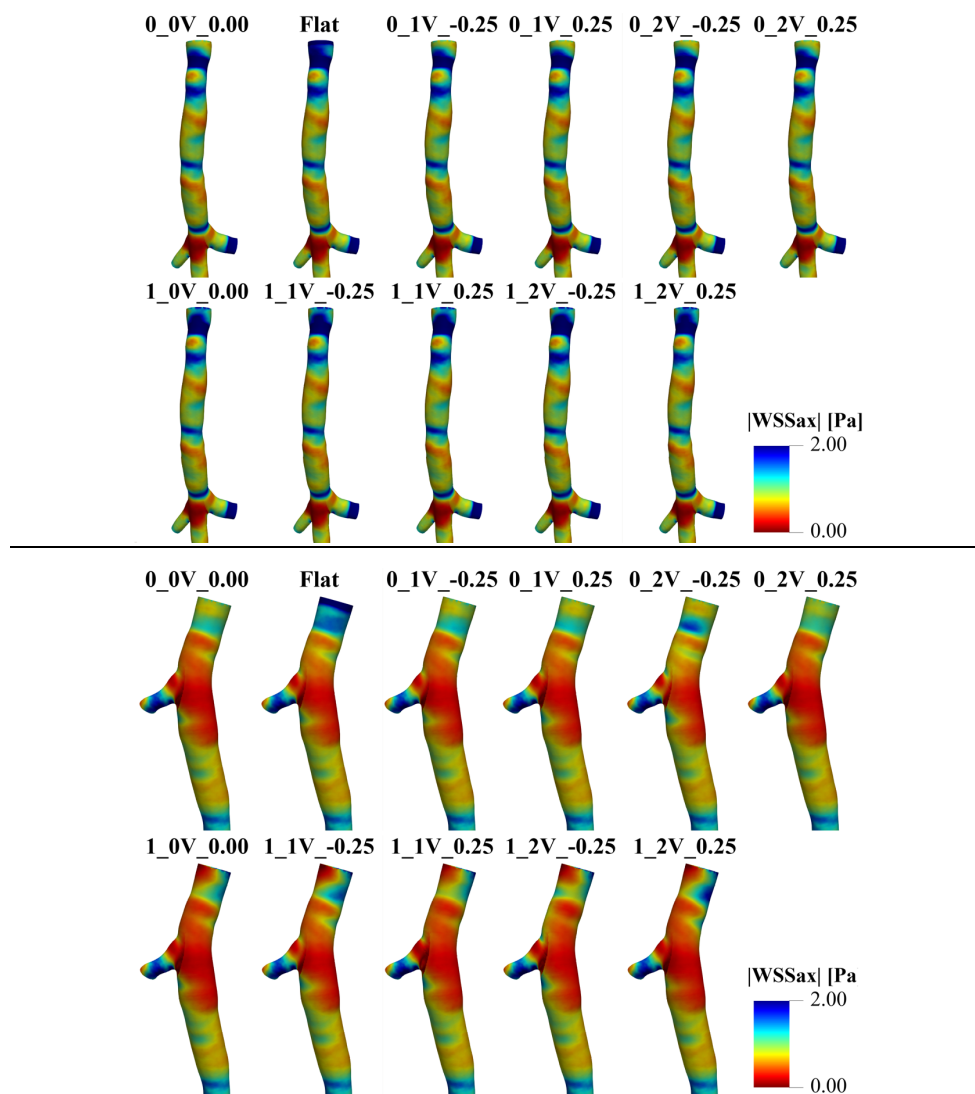


Figure 5.11 P4 (Top) and P8 (Bottom) |WSSax| surface maps

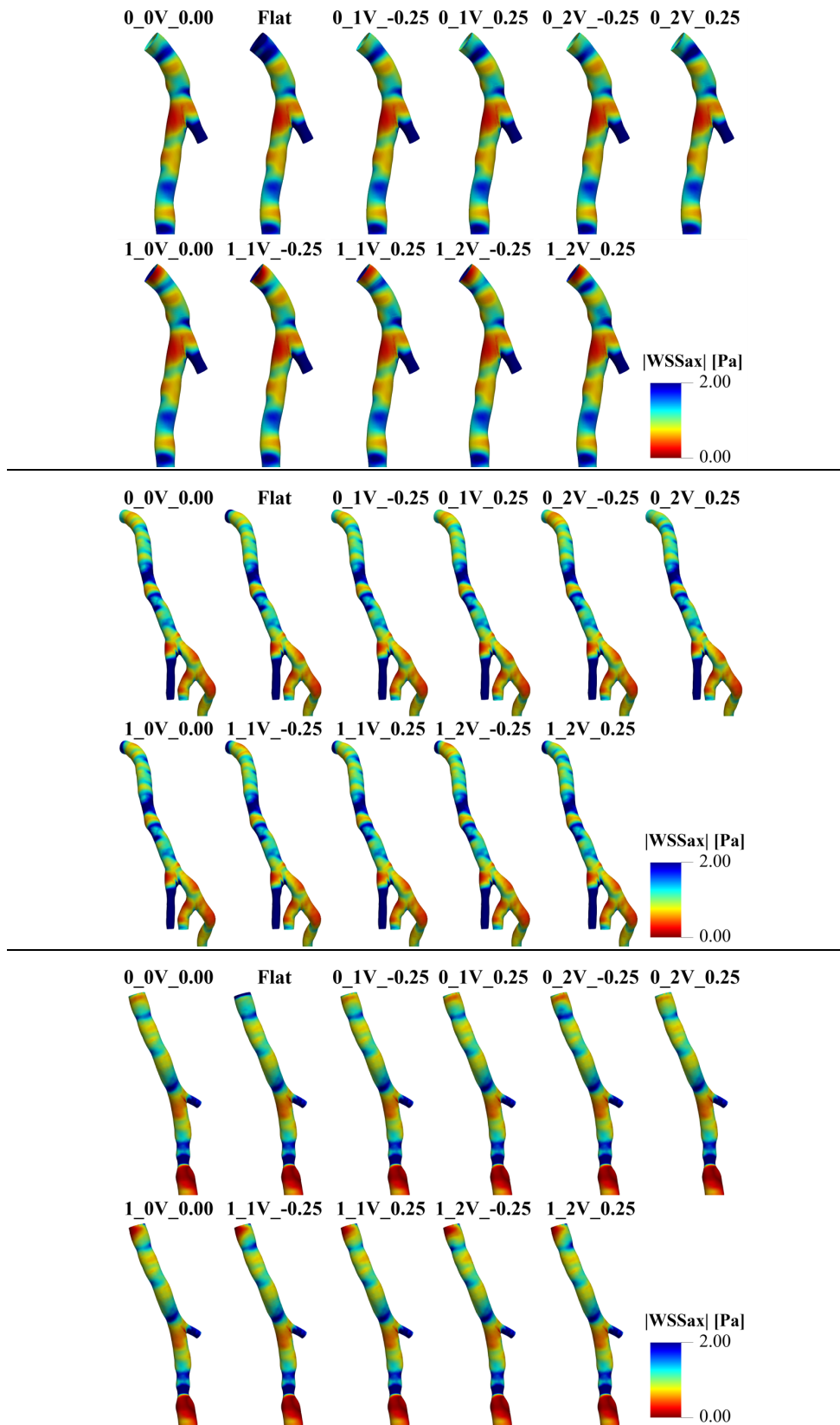


Figure 5.12 P10 (Top), P14 (Middle) and P19 (Bottom) |WSSax| surface maps

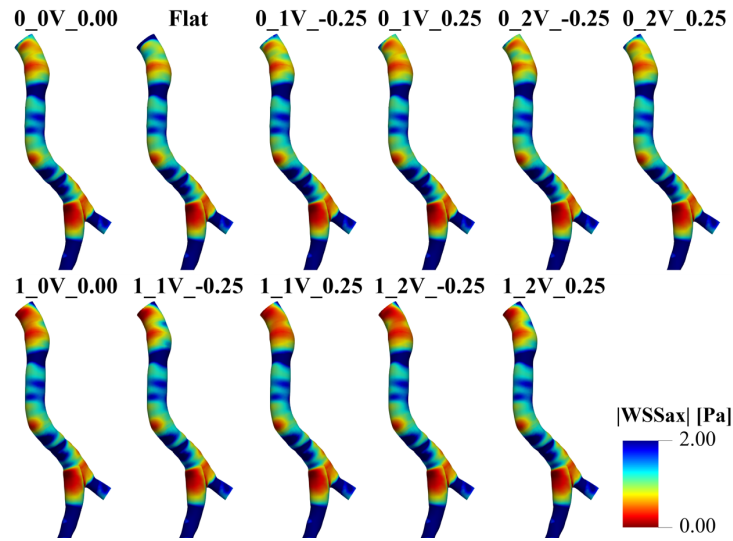


Figure 5.13 P23 |WSSax| surface maps

The WSS_{ax} magnitude color maps are very similar to those related to WSS, probably because hemodynamic forces acting on the vascular wall are mainly influenced by the axial component of the velocity. Also in this case, lower values are located next to bifurcations, branching sites and curved tracts. Further information is given by the surface averaged values depicted in the following figures.

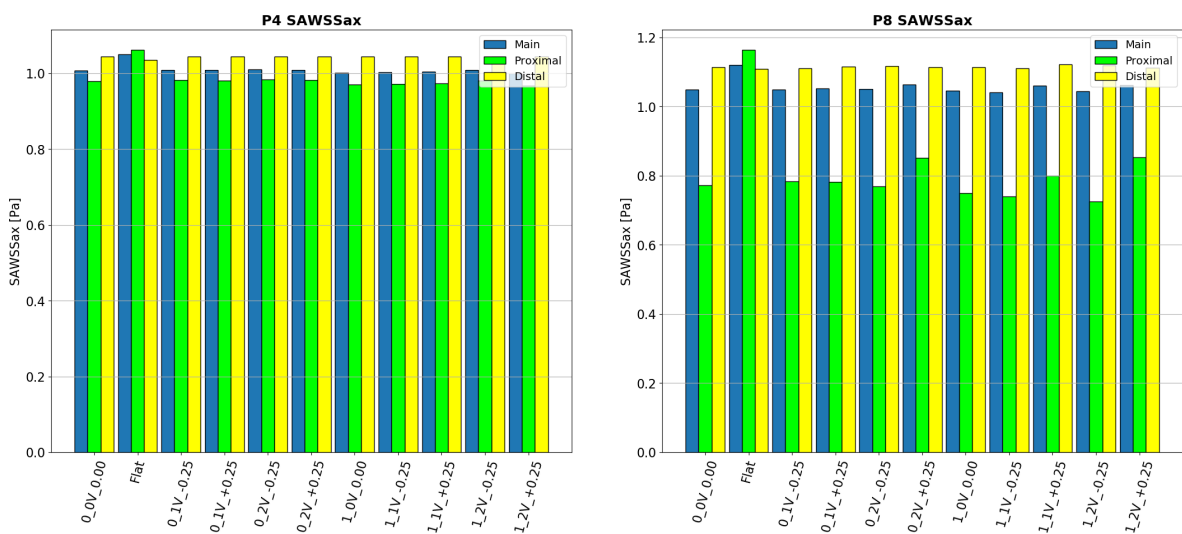


Figure 5.14 Models' SAWSSax (1)

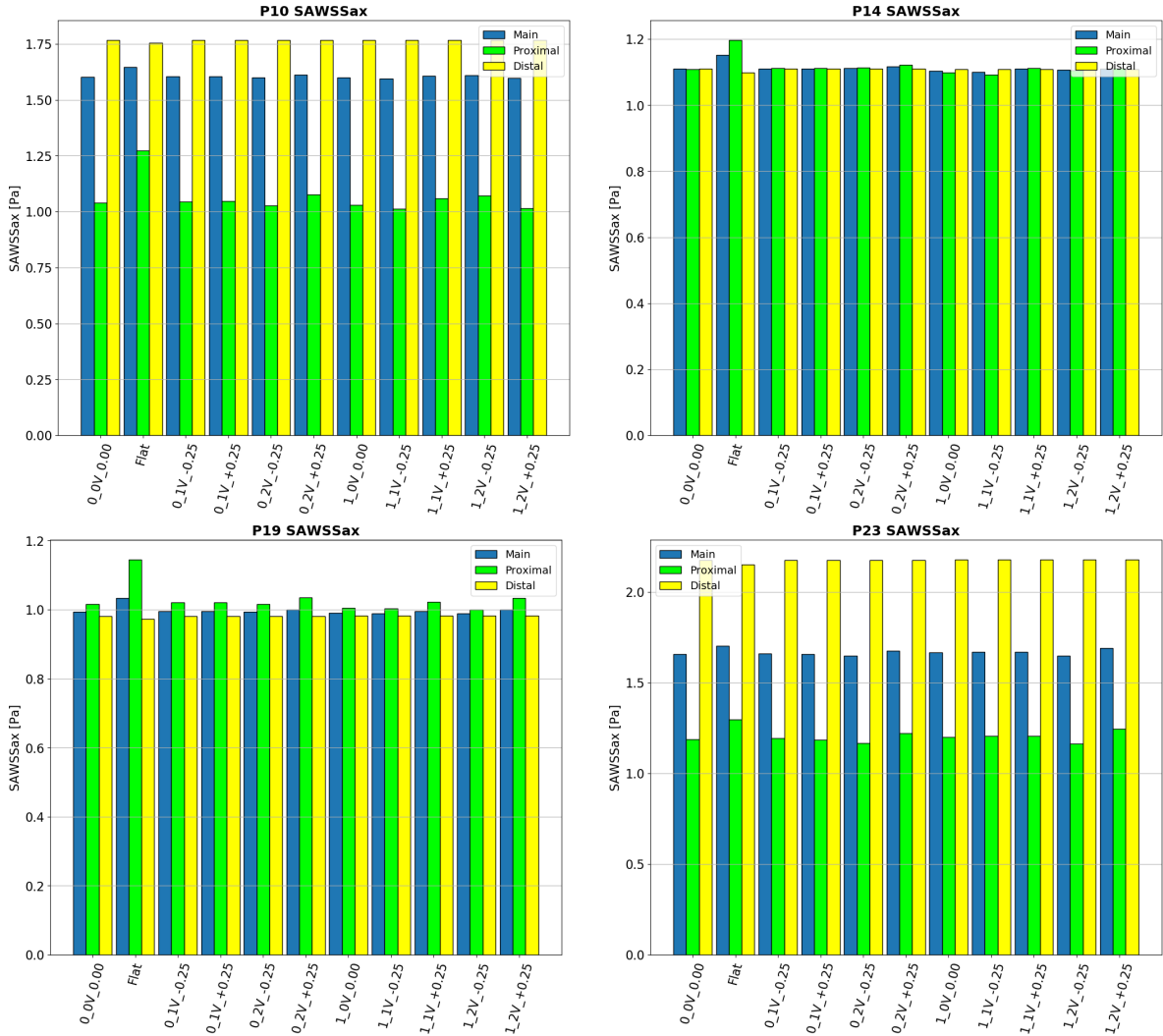


Figure 5.15 Figure 5.14 Models' SAWSSax (2)

SAWSSax behaves alike SAWSS as well. This trend apparently suggests that the the blood flow is mostly dominated by the axial component of velocity which mainly impacts on the hemodynamic results.

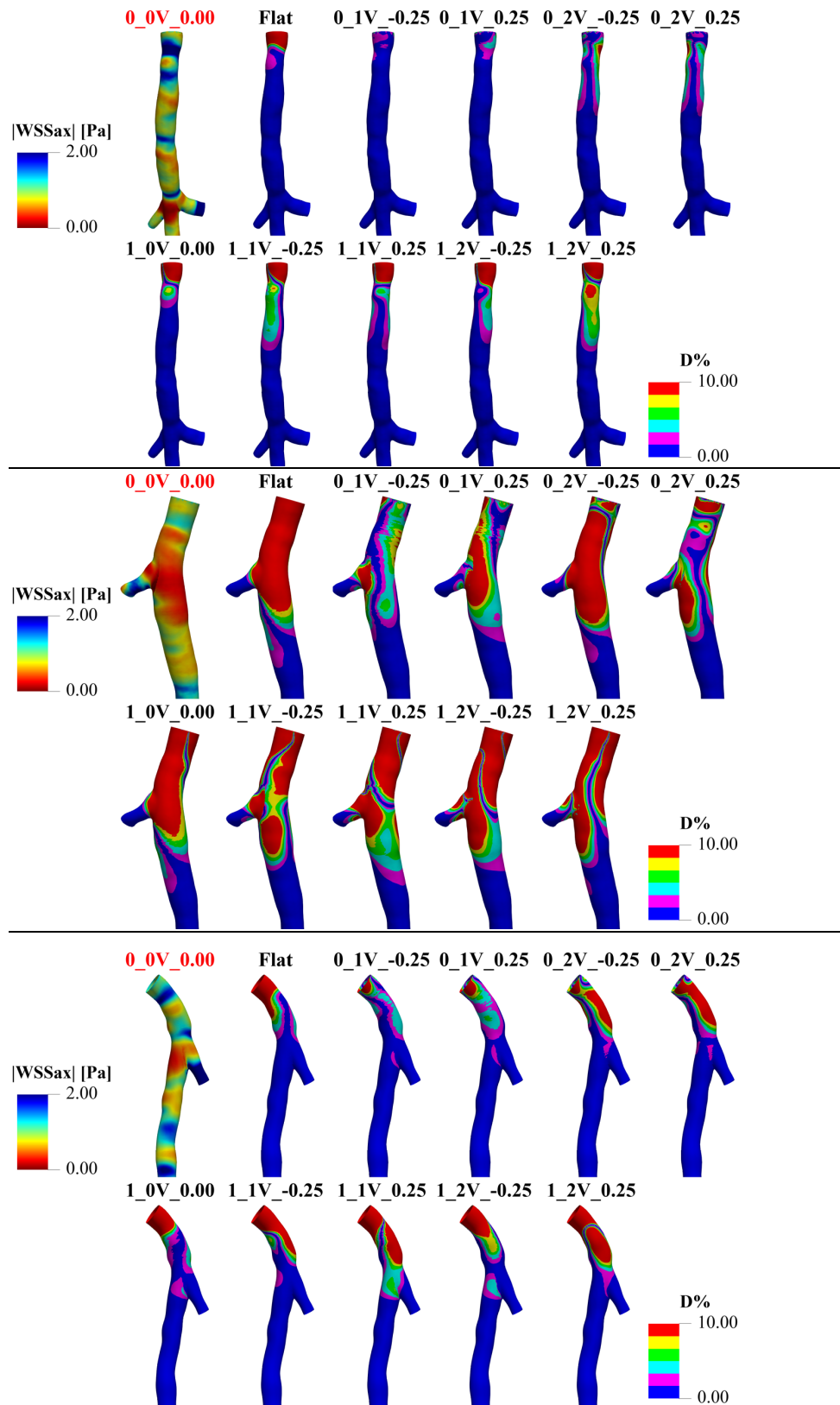


Figure 5.16 P4 (Top), P8 (Middle) and P10 (Bottom) |WSSax| percentage difference surface maps

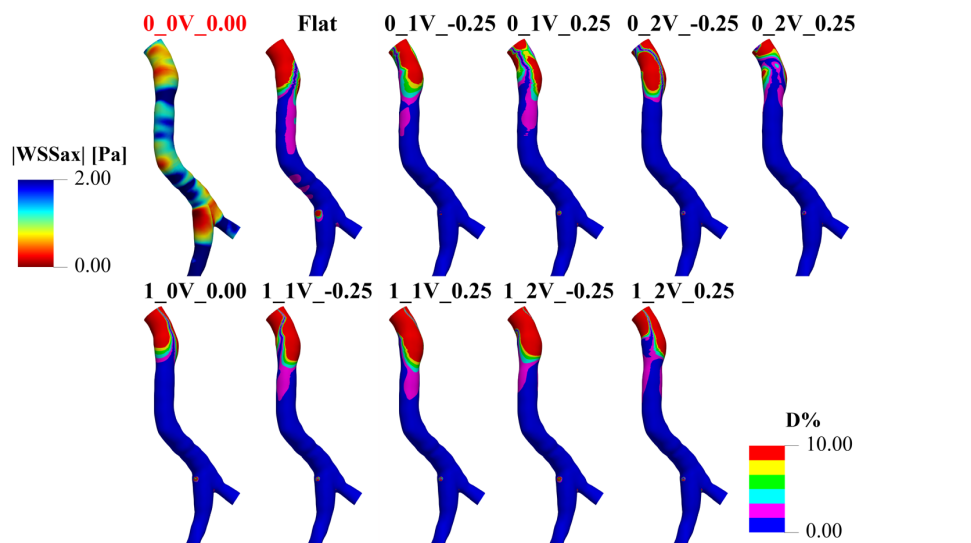
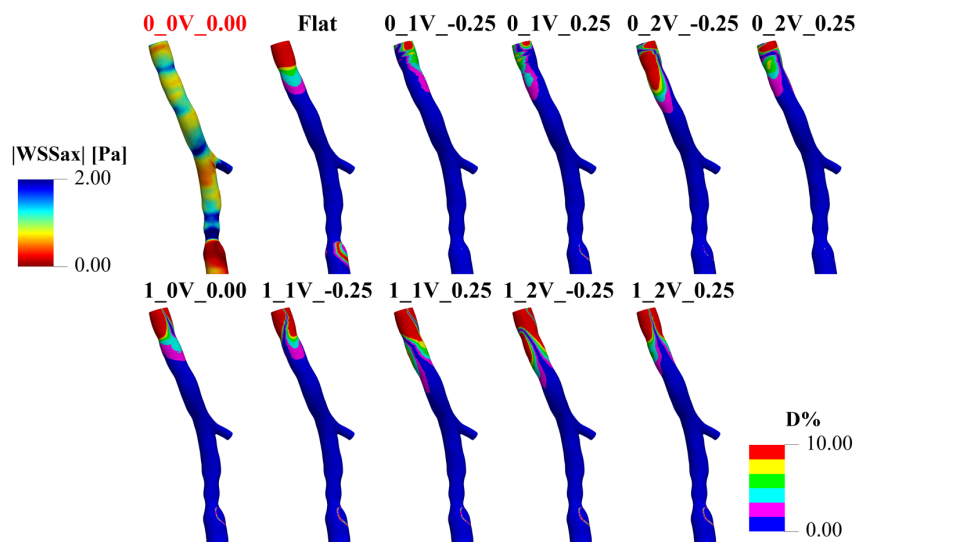
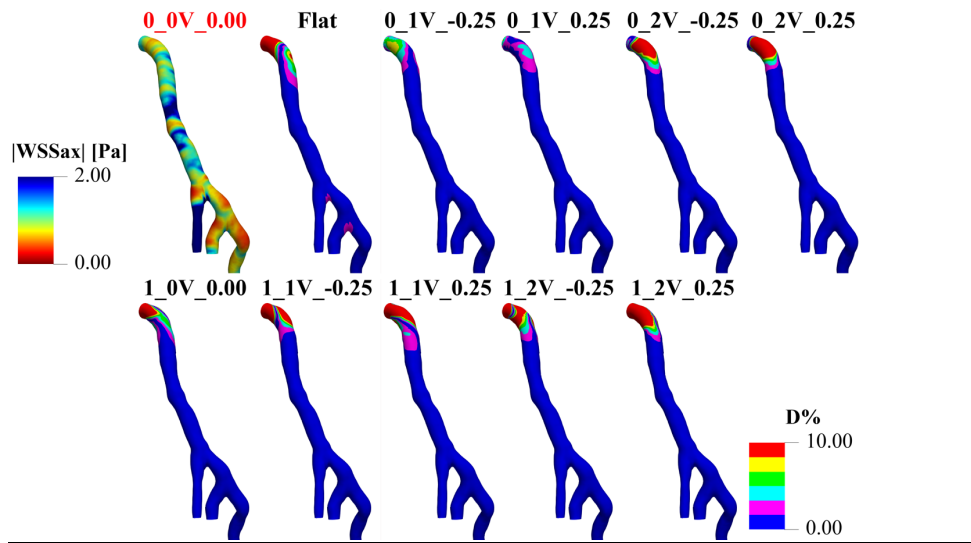


Figure 5.17 P14 (Top), P19 (Middle) and P23 (Bottom) $|WSS_{ax}|$ percentage difference surface maps

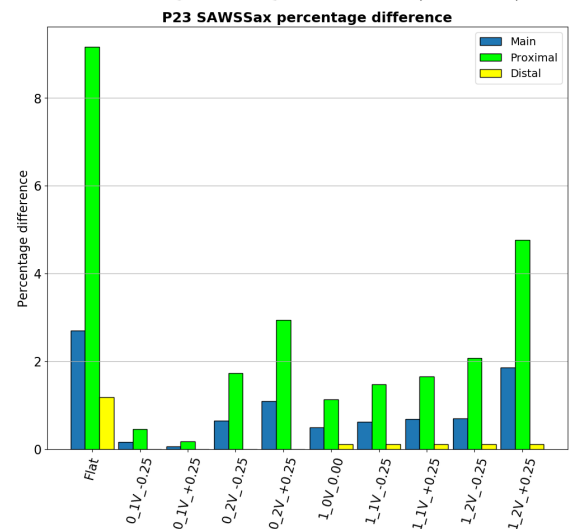
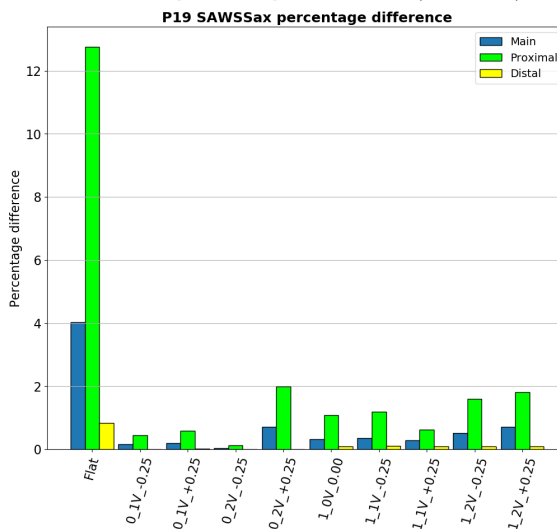
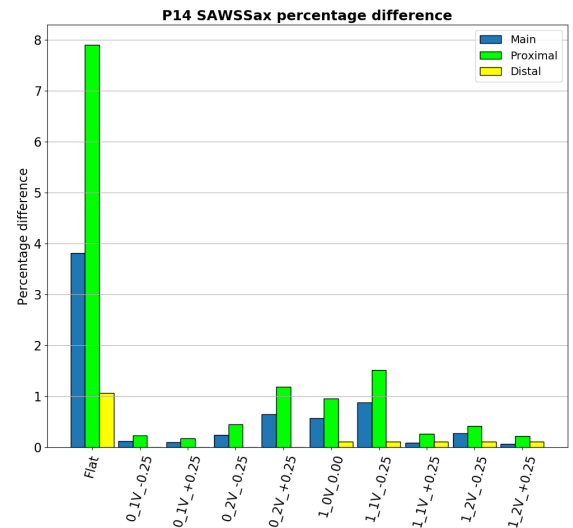
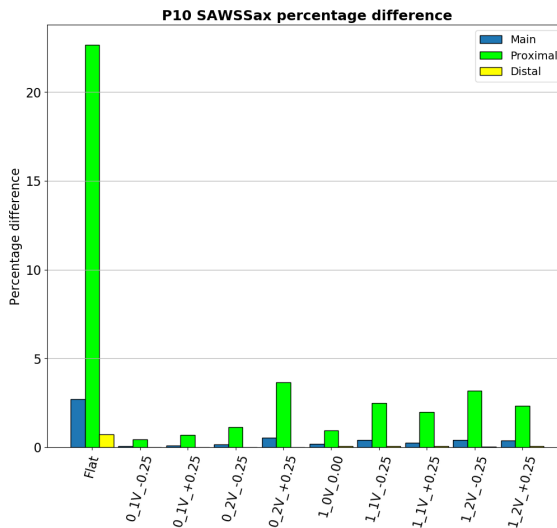
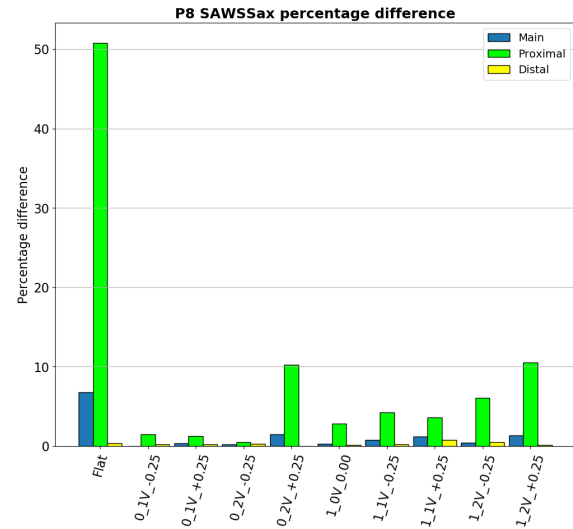
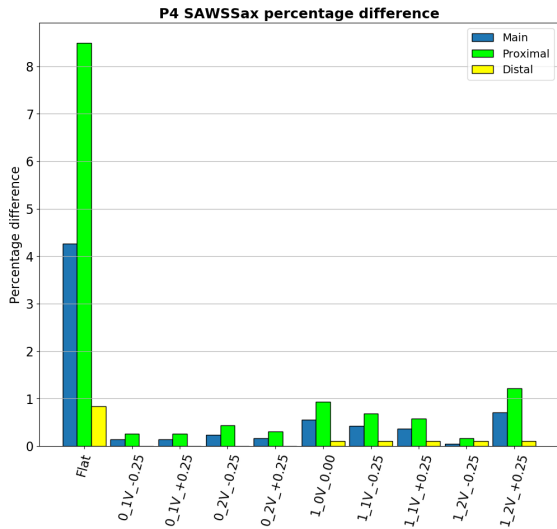


Figure 5.18 Models' SAWSSax percentage difference

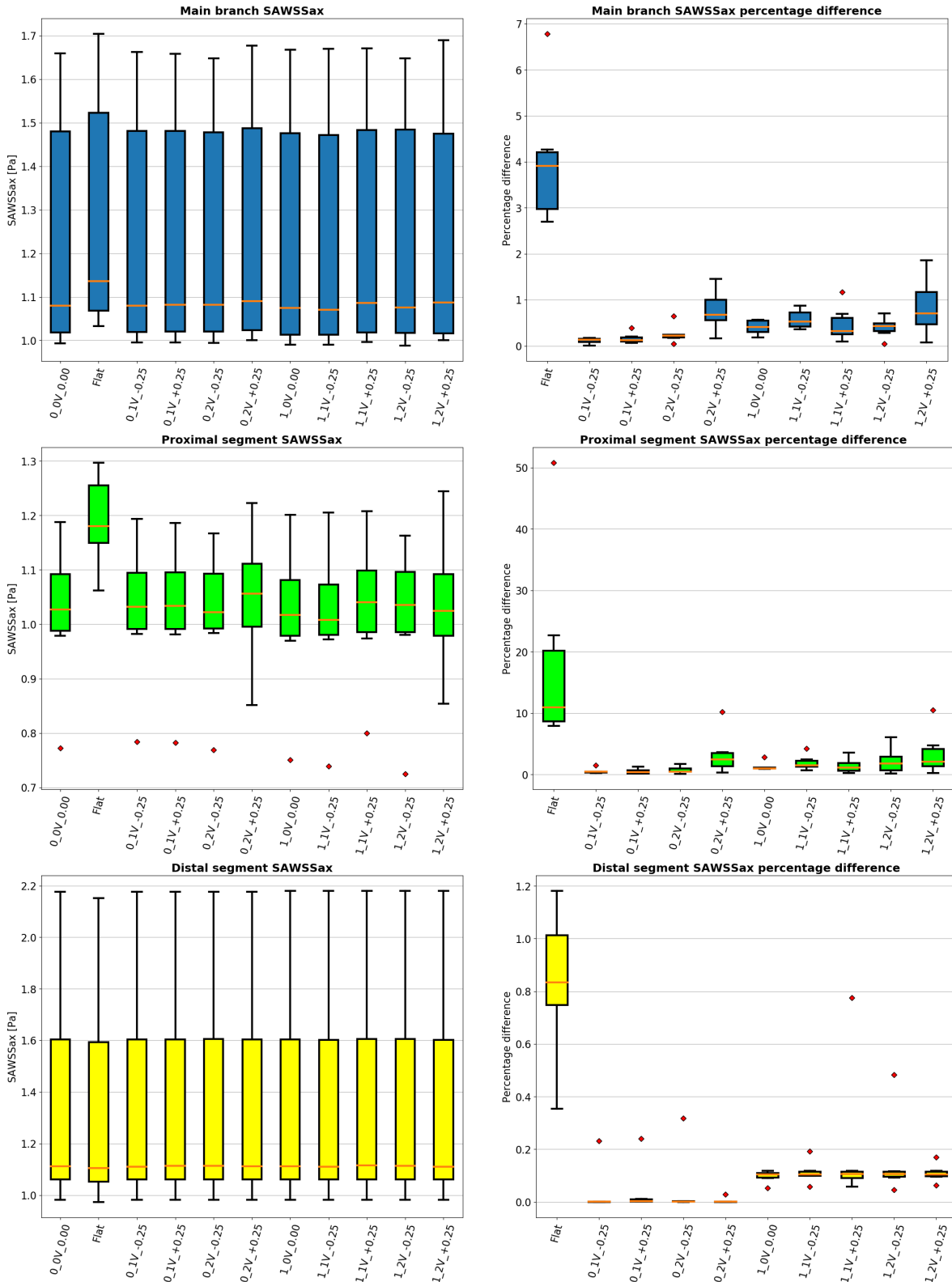


Figure 5.19 WSSax summarizing boxplots

All WSSax results are consistent with those of WSS magnitude.

5.1.3 Secondary wall shear stress (WSSsc)

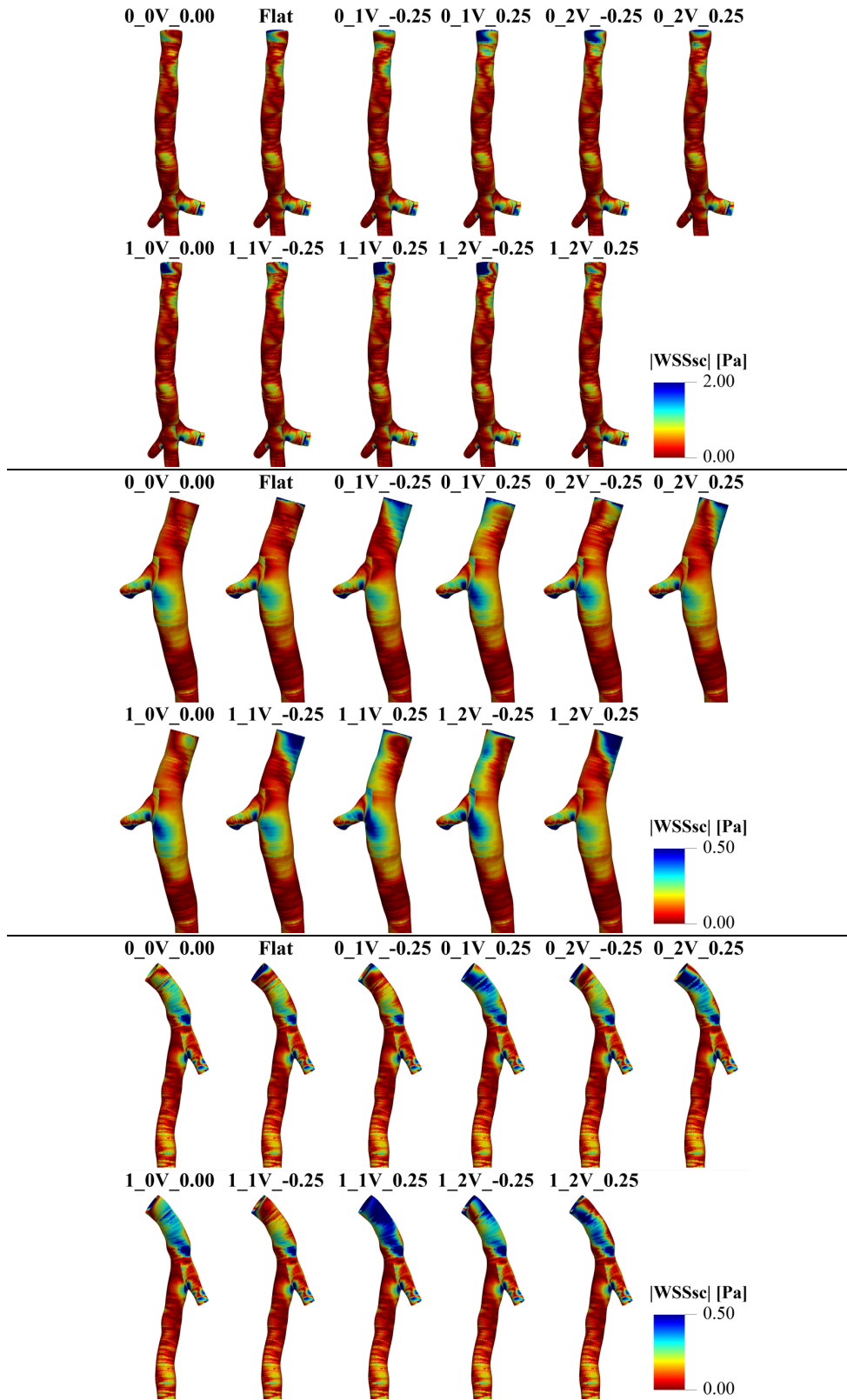


Figure 5.20 P4 (Top), P8 (Middle) and P10 (Bottom) |WSSsc| surface maps

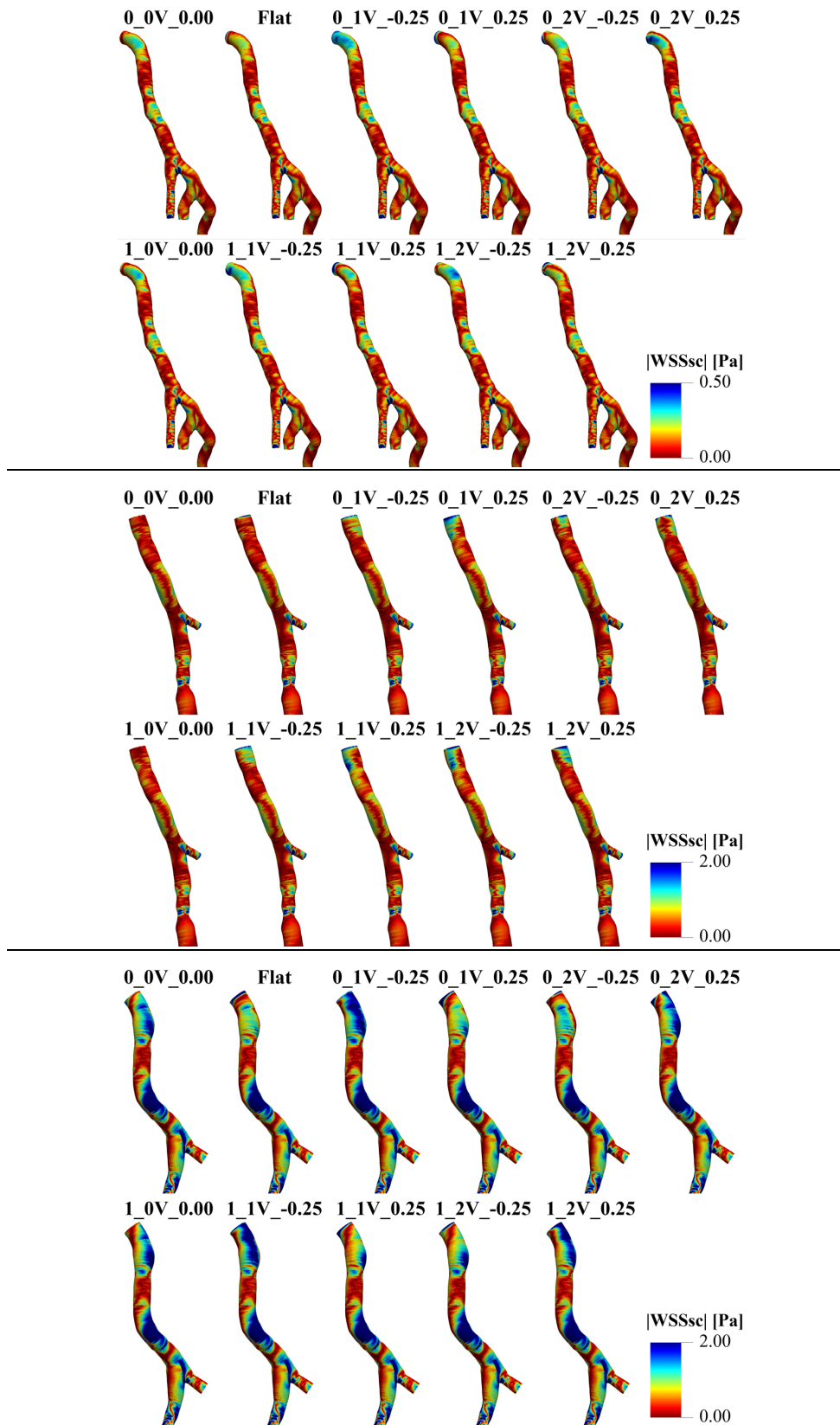


Figure 5.21 P14 (Top), P19 (Middle) and P23 (Bottom) |WSSsc| surface maps

WSSsc magnitude surface maps depict a complementary situation with respect to those of WSSax magnitude. WSSsc magnitude takes lower values than WSSax and in correspondence of not-curved sections of the vessels takes lower values whereas in curved tracts, bifurcations and branching sites assumes higher values due to the occurrence of vortices and complex flows. In fact, paying attention to P23 model surface maps, it can be noticed that since P23 has the most winding morphology between the examined models, presents higher values of WSSsc along the whole vessel. Such consideration is supported by SAWSSsc bar plots.

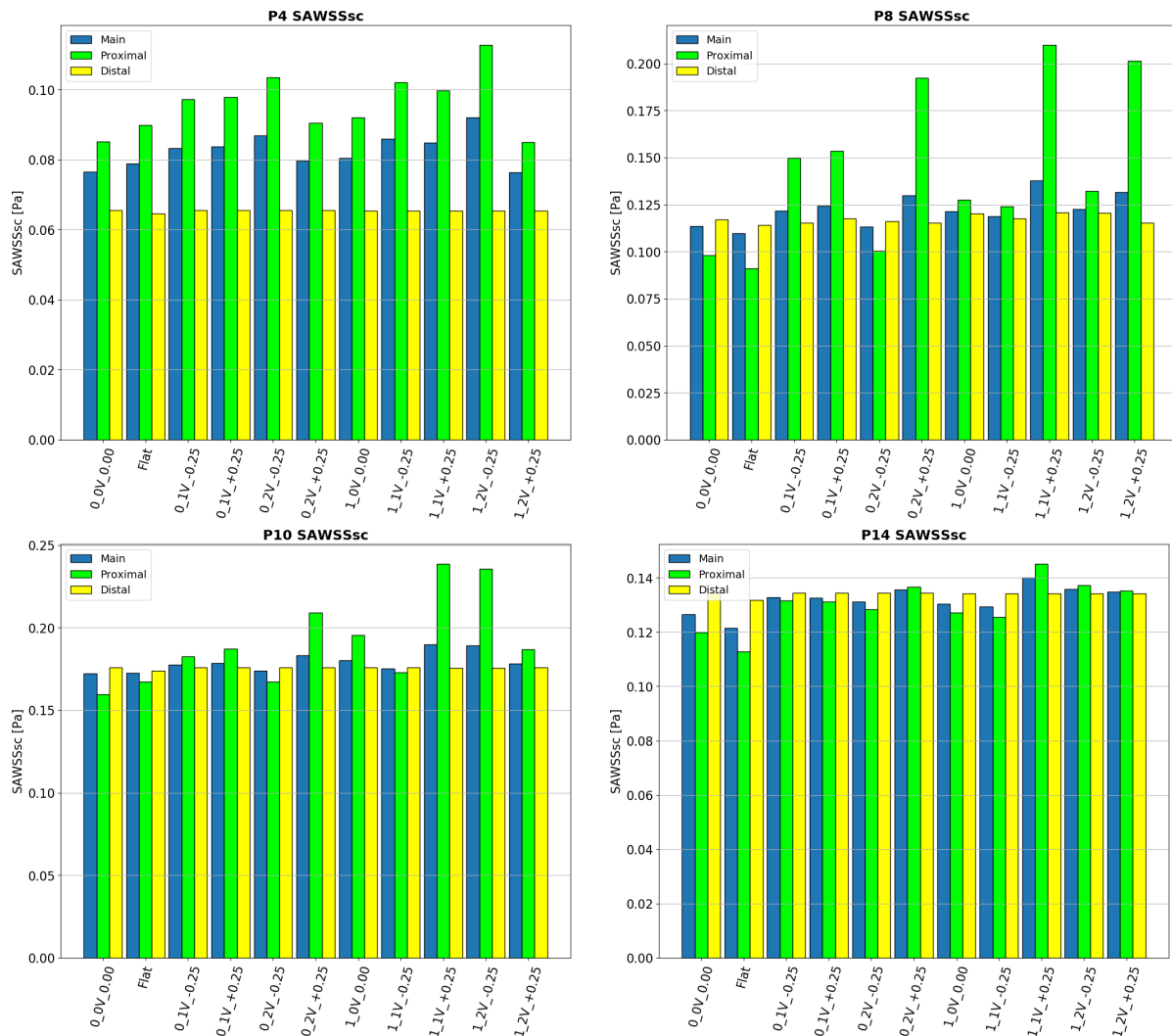


Figure 5.22 Models' SAWSSsc (1)

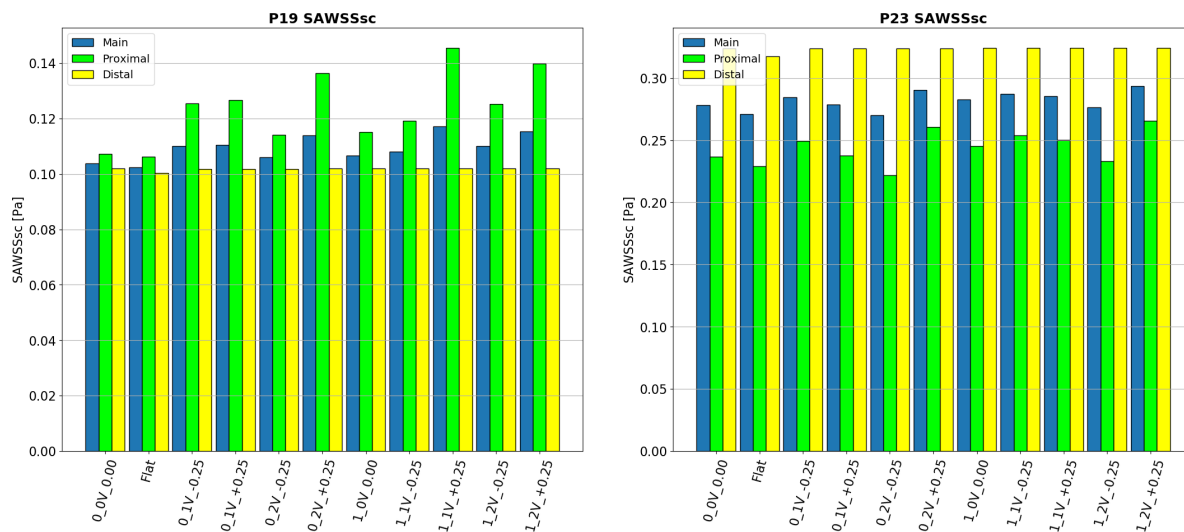


Figure 5.23 Figure 5.22 Models' SAWSSsc (2)

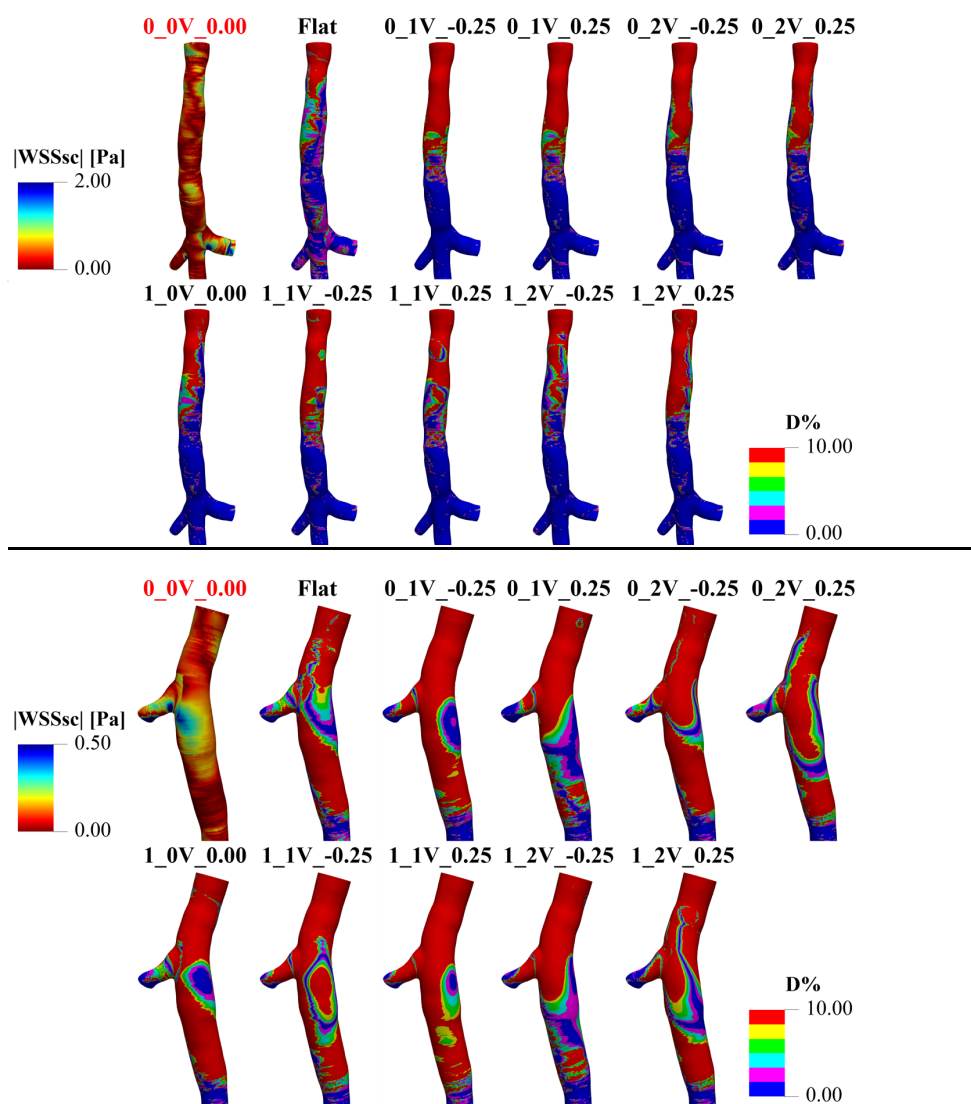


Figure 5.24 P4 model (Top) and P8 (Bottom) |WSSsc| percentage difference surface maps

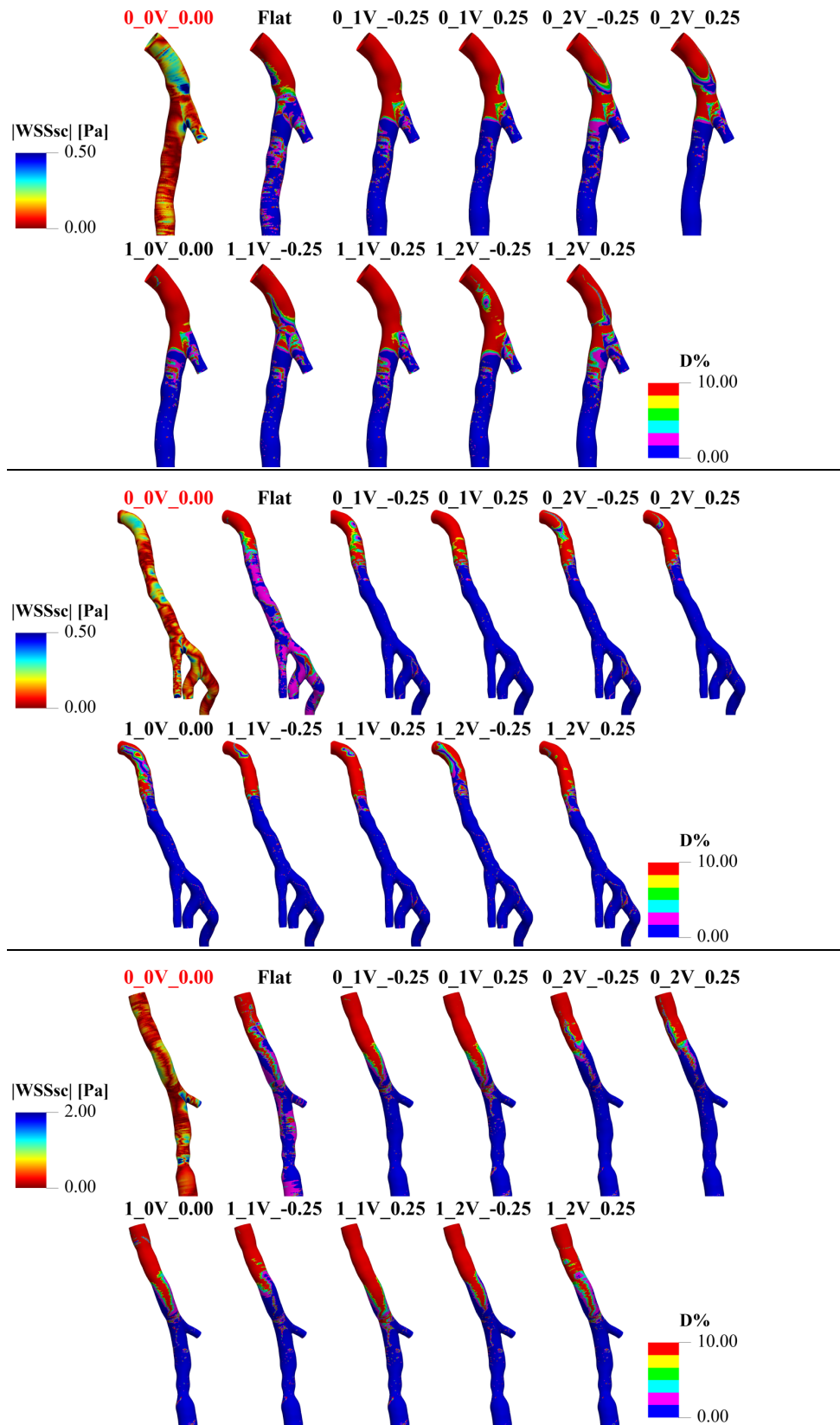


Figure 5.25 P10 (Top), P14 (Middle) and P19 (Bottom) $|WSSsc|$ percentage difference surface maps

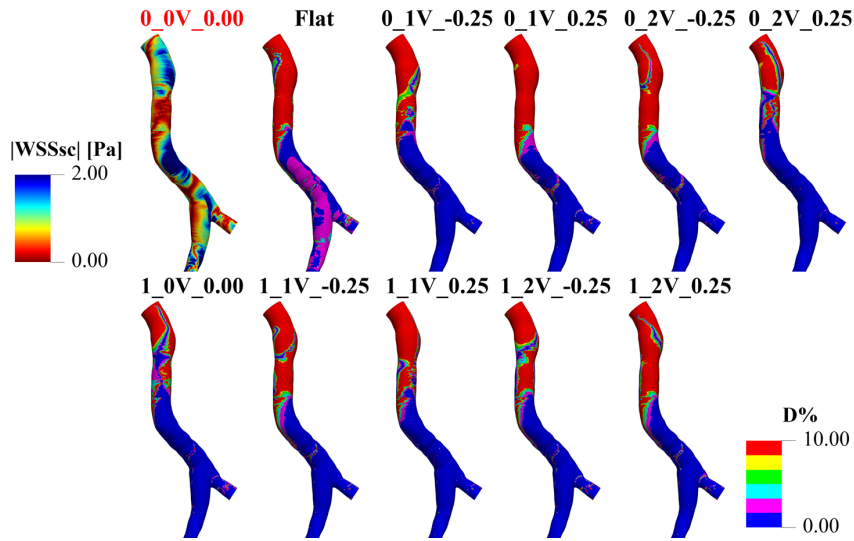


Figure 5.26 P23 |WSSsc| percentage difference surface maps

The WSSsc magnitude percentage difference surface maps present the same phenomenon seen for WSS and WSSax: differences from reference profile “0_0V_0.00” are located near by the inlet region of the model, until the decrease to 0% after a certain distance from the inlet surface. “Flat” profile, also in this case takes differences greater than 0% in the remaining part of the vessel.

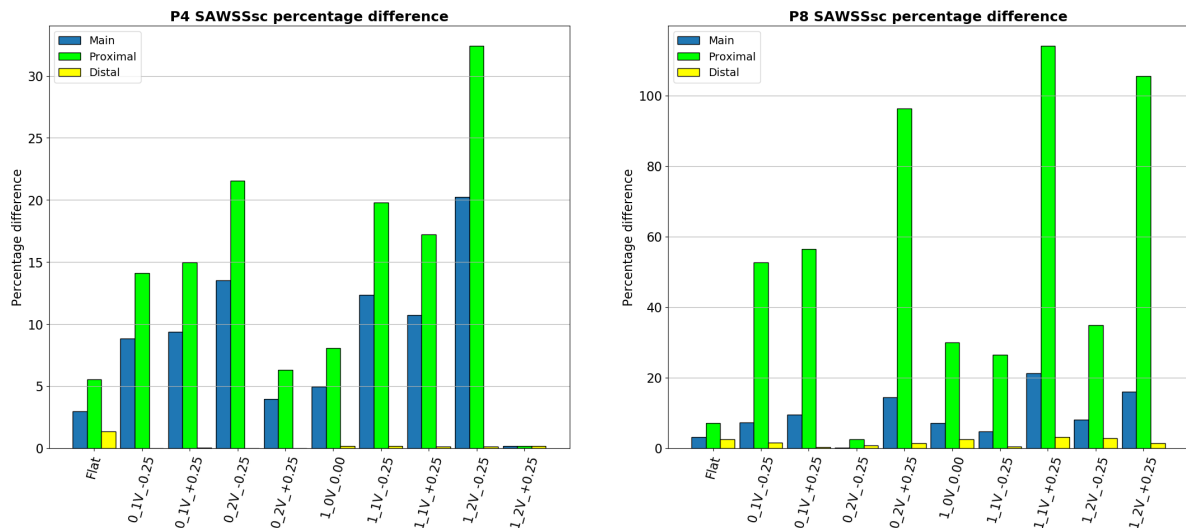


Figure 5.27 Models' SAWSSsc percentage difference (1)

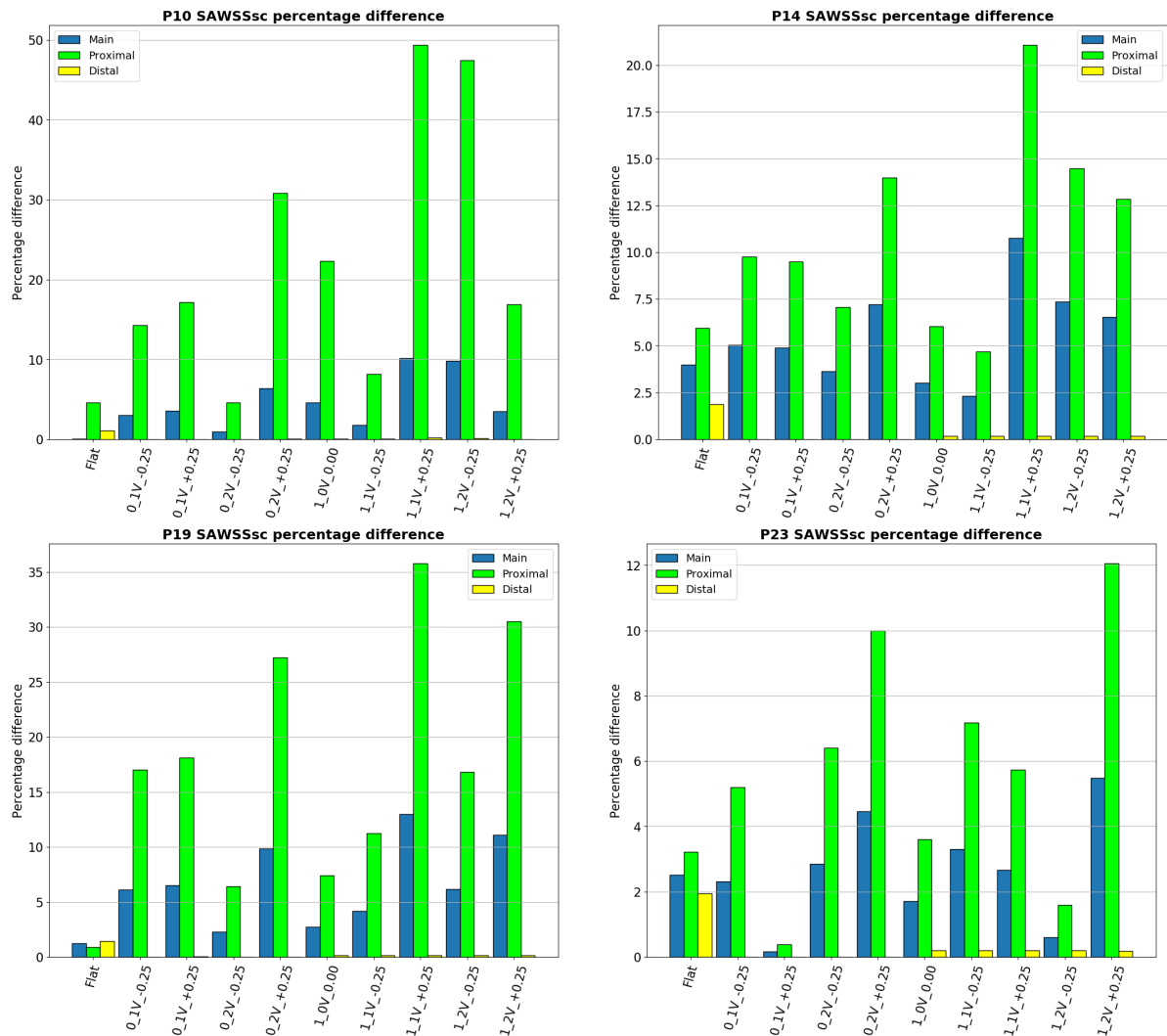


Figure 5.28 Figure 5.27 Models' SAWSSsc percentage difference (2)

As can be seen from SAWSSsc percentage difference bar plots, differences are not low as for SAWSS and SAWSSax. “Flat” profile is not the one that gives back the highest differences anymore. It is logical to suppose that WSSsc is more influenced from the geometry of the vessel since differences are highly changeable between the models. Differences are displayed in the proximal segment whereas in the distal one they are nearly always negligible. The following summarizing boxplot highlight what has been said so far.

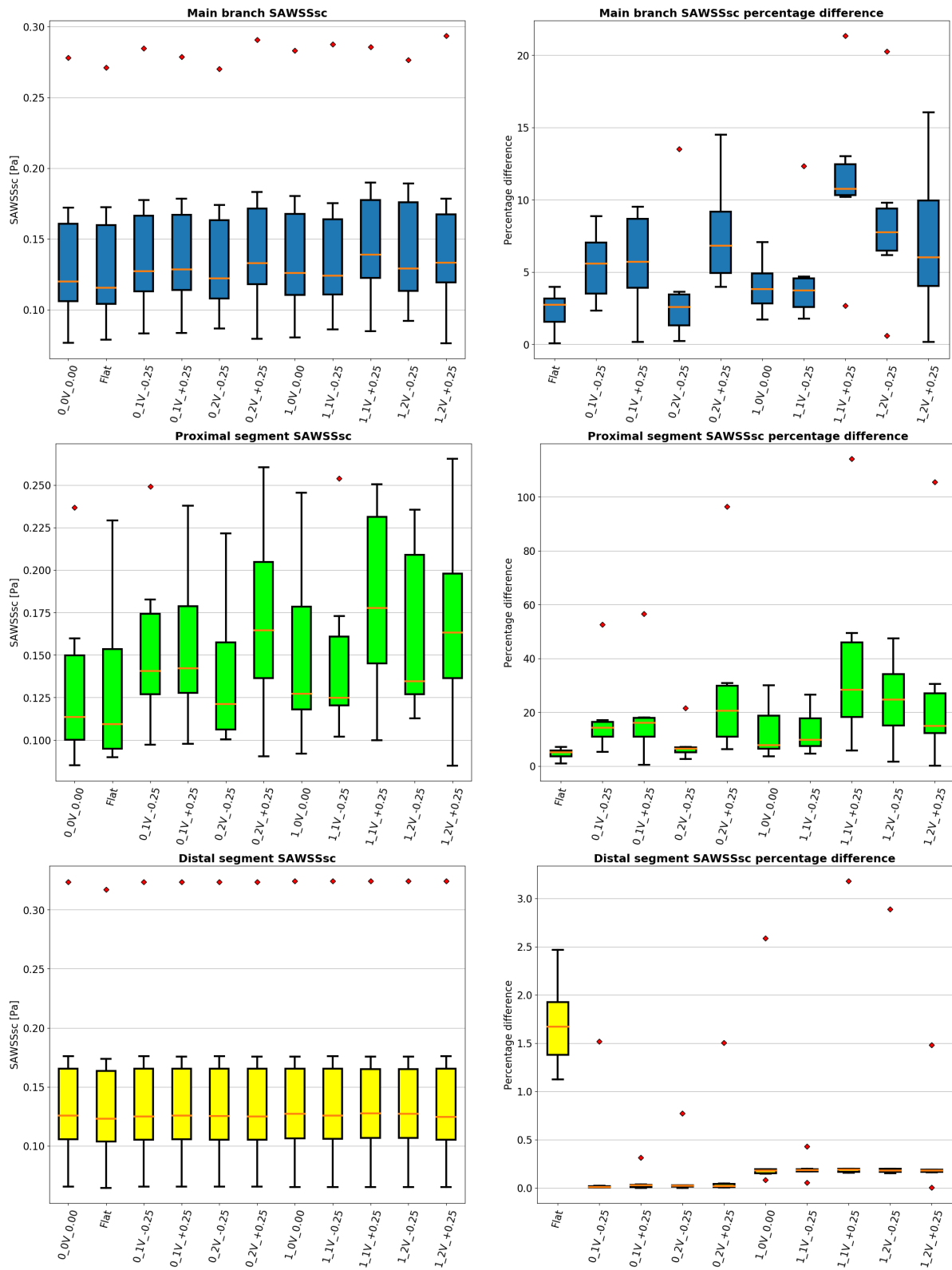


Figure 5.29 WSSc summarizing boxplots

5.1.4 Wall shear stress ratio (WSSratio)

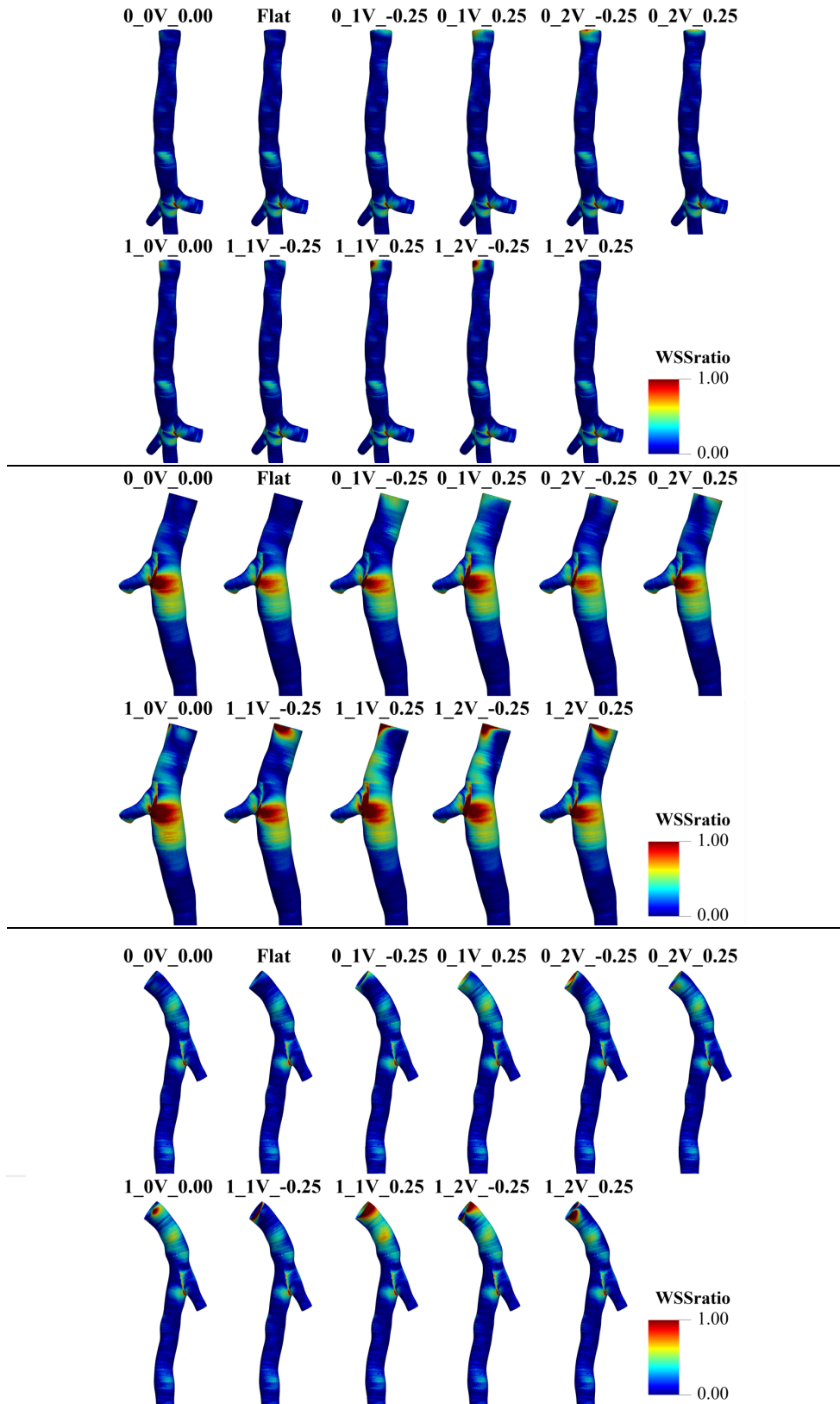


Figure 5.30 P4 (Top), P8 (Middle) and P10 (Bottom) WSSratio surface maps

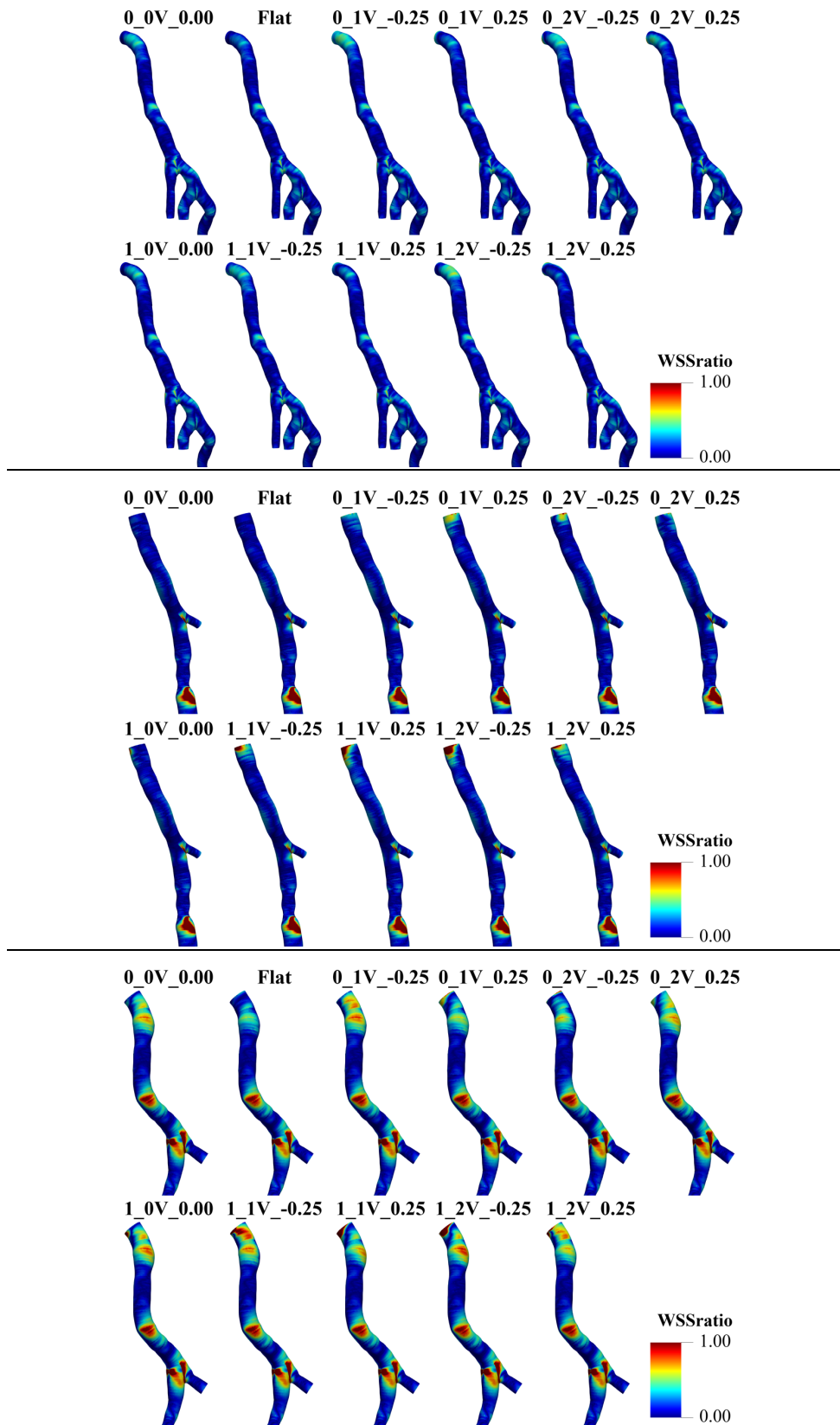


Figure 5.31 P14 (Top), P19 (Middle) and P23 (Bottom) WSSratio surface maps

As expected, WSSratio assumes higher values in those regions of the vessel corresponding to curved tracts and bifurcations, where the secondary WSS is more relevant. Furthermore, for profiles provided with in-plane component, WSSratio surface maps present higher values at the inlet than those provided only with through-plane component of velocity. In the remaining part of the vessels, WSSratio decreases to 0, which means that the axial component of WSS is dominant.

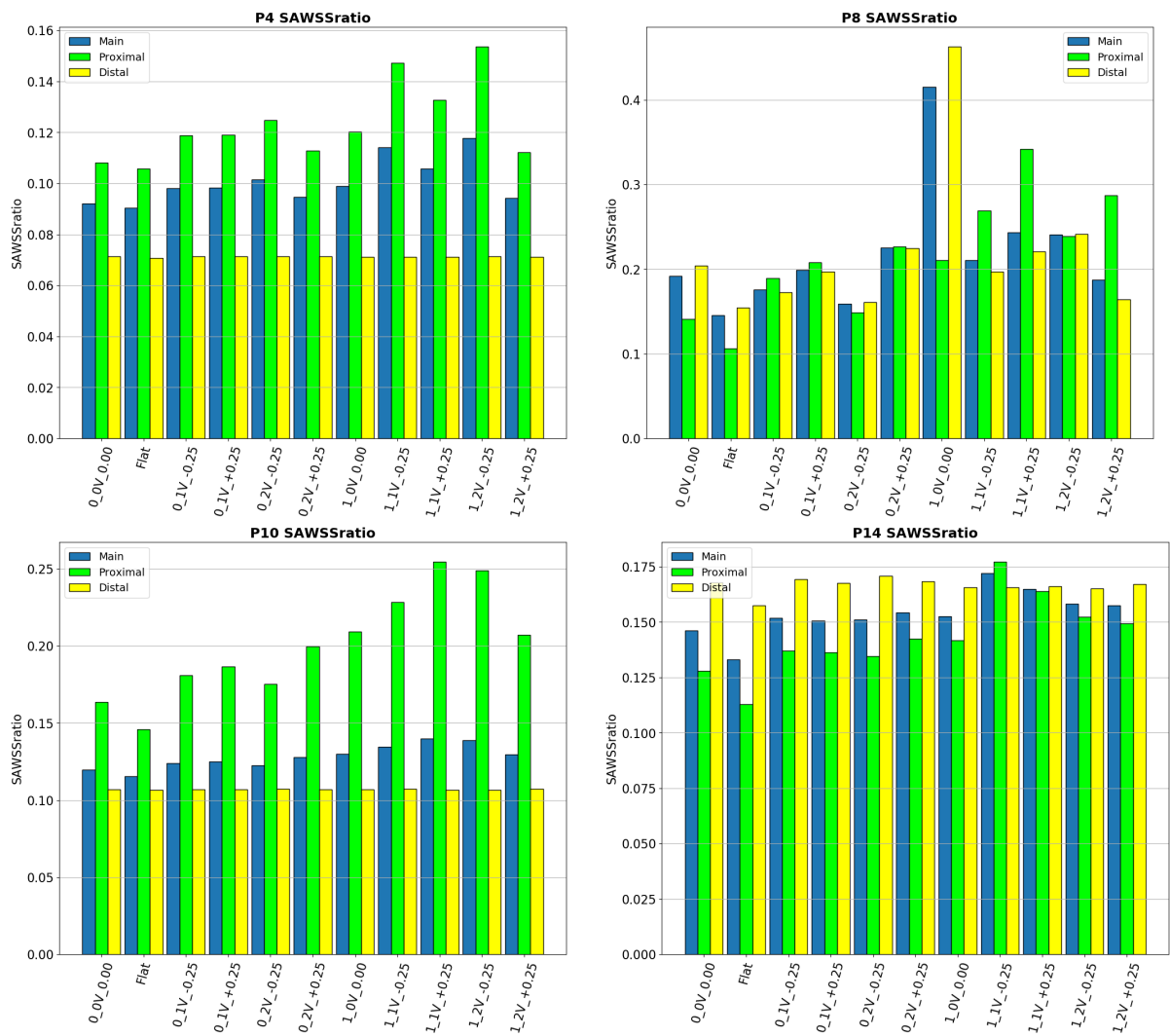


Figure 5.32 Models' SAWSSratio (1)

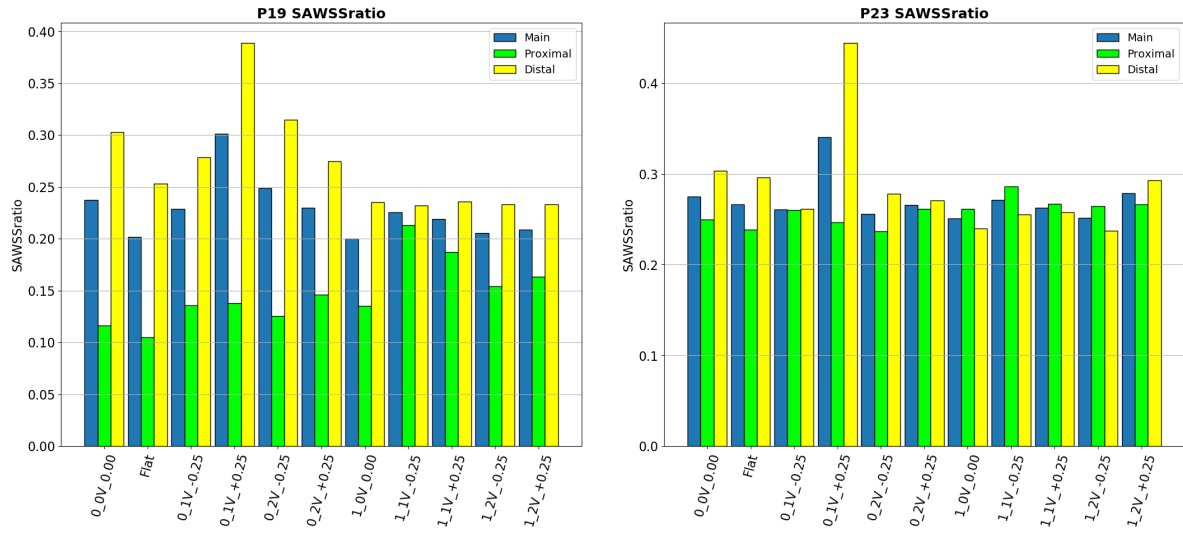


Figure 5.33 Models' SAWSSratio (2)

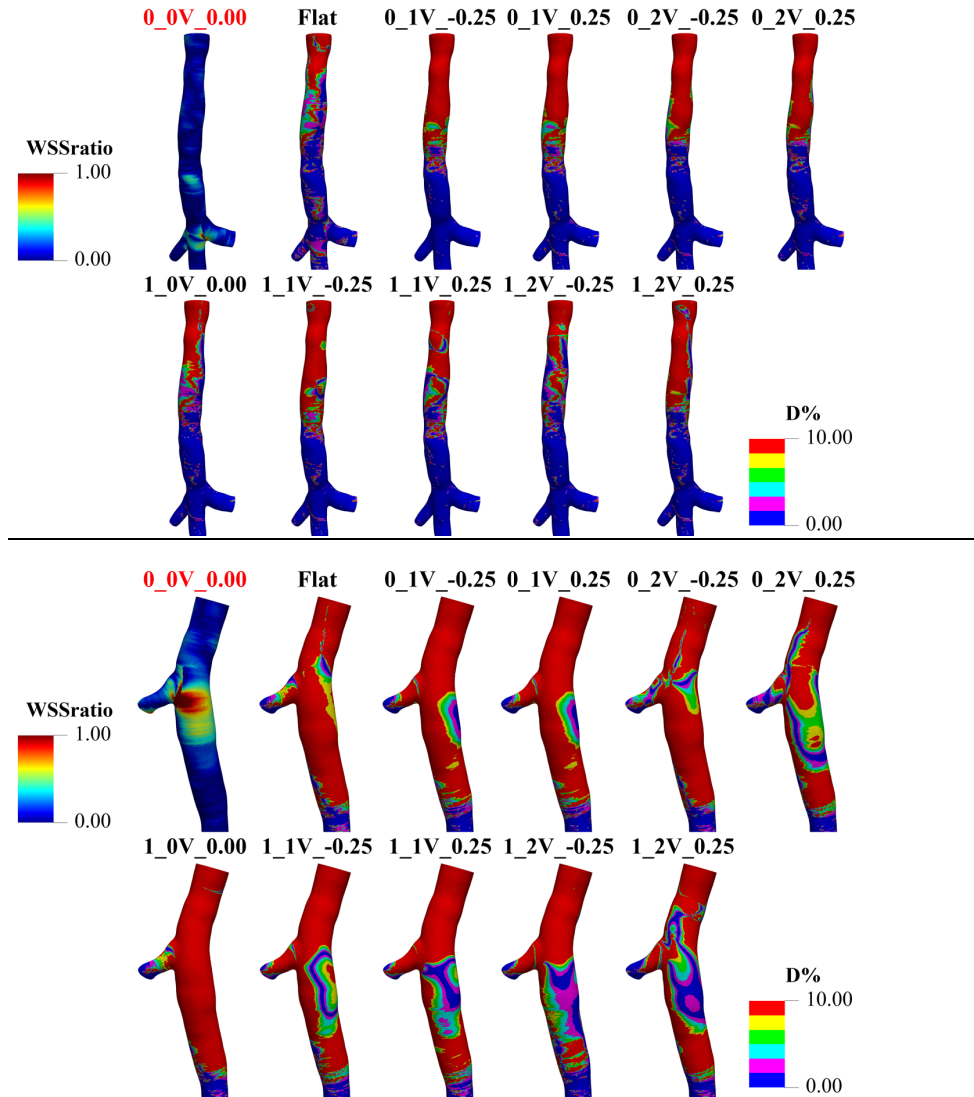


Figure 5.34 P4 (Top) and P8 (Bottom) WSSratio percentage difference surface maps

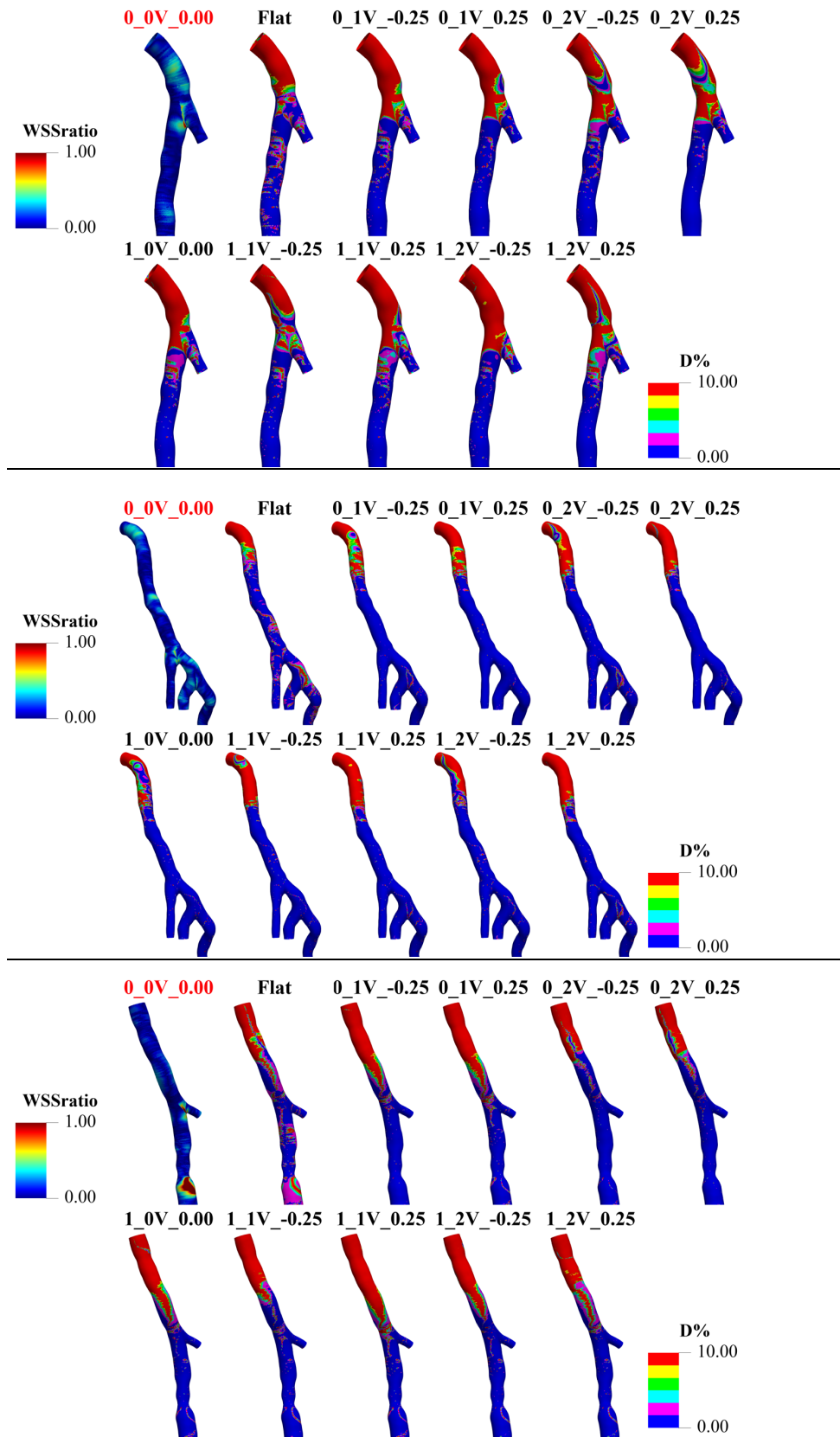


Figure 5.35 P10 (Top), P14 (Middle) and P19 (Bottom) WSSratio percentage difference surface maps

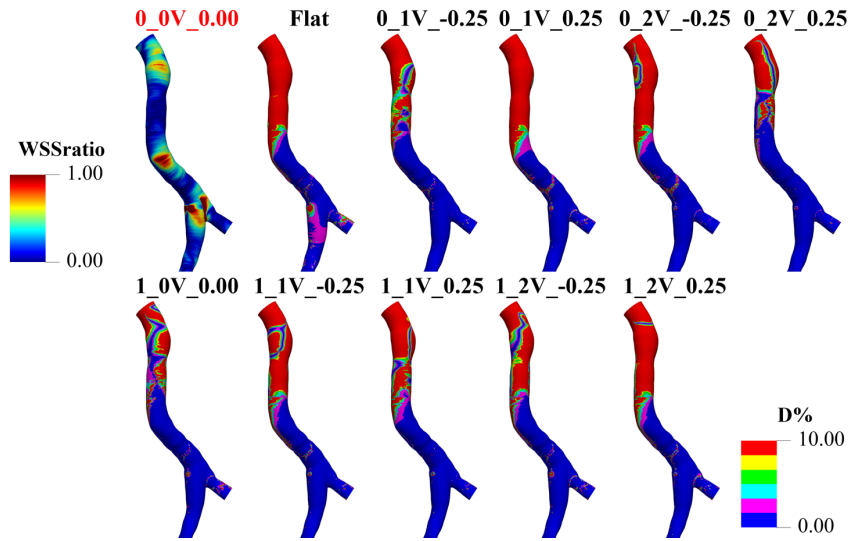


Figure 5.36 P23 WSSratio percentage difference surface maps

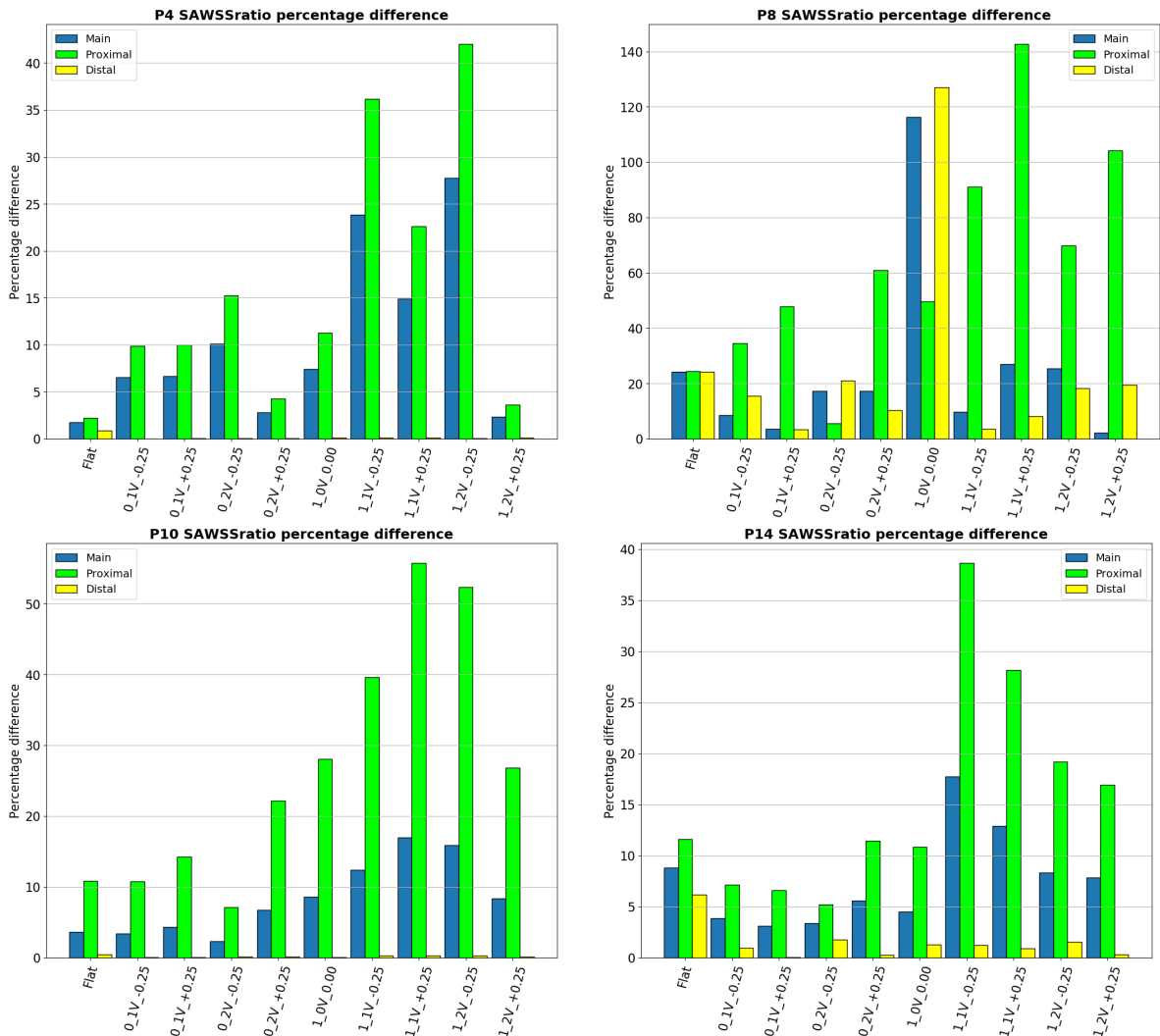


Figure 5.37 Models' SAWSSratio percentage difference (1)

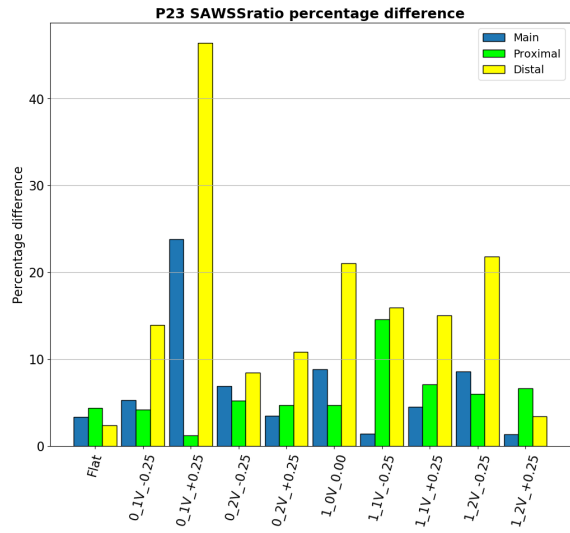
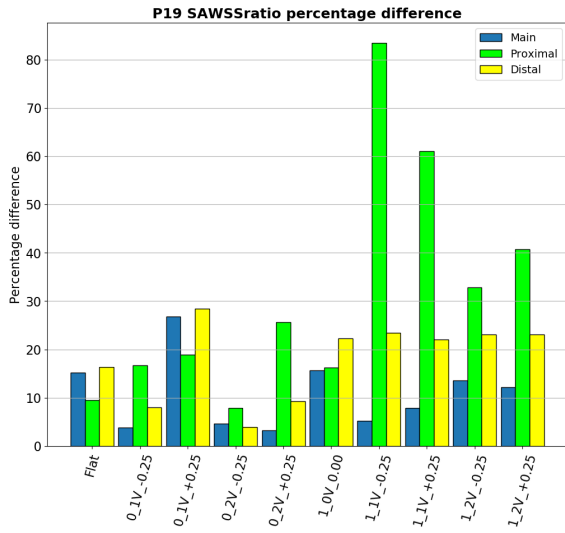


Figure 5.38 Figure 5.37 Models' SAWSSratio percentage difference (2)

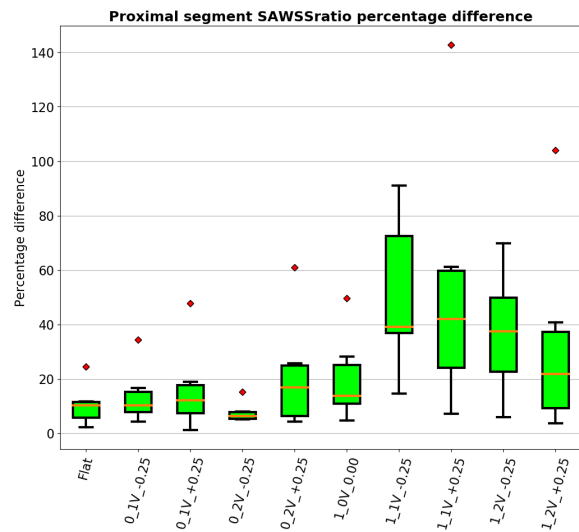
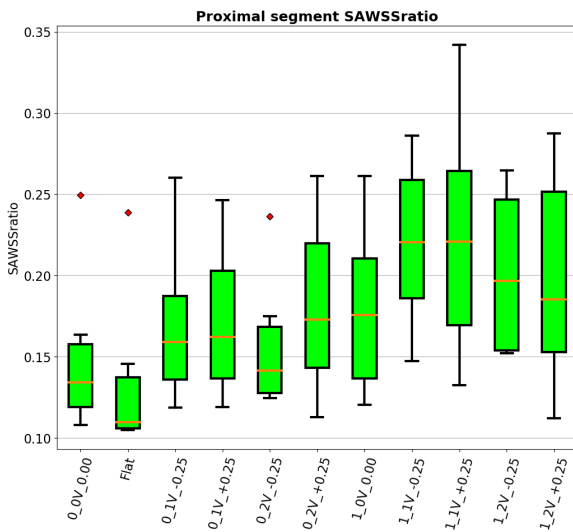
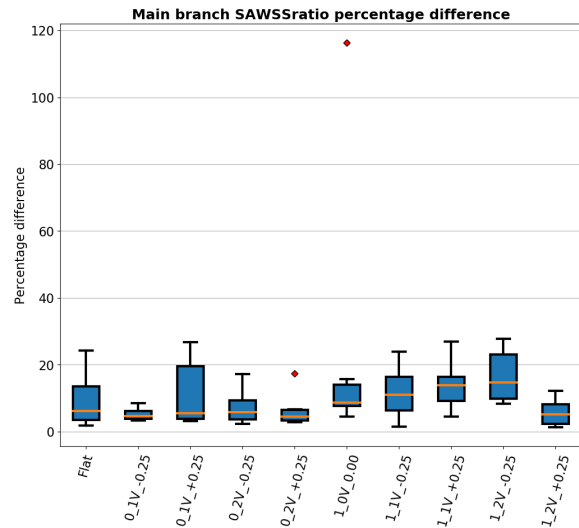
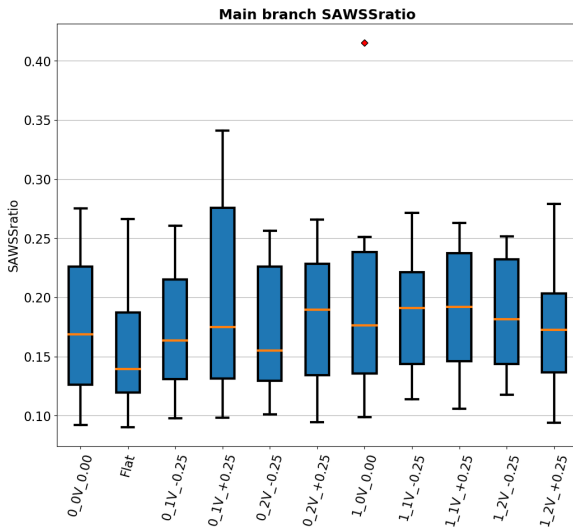


Figure 5.39 WSSratio summarizing boxplots (1)

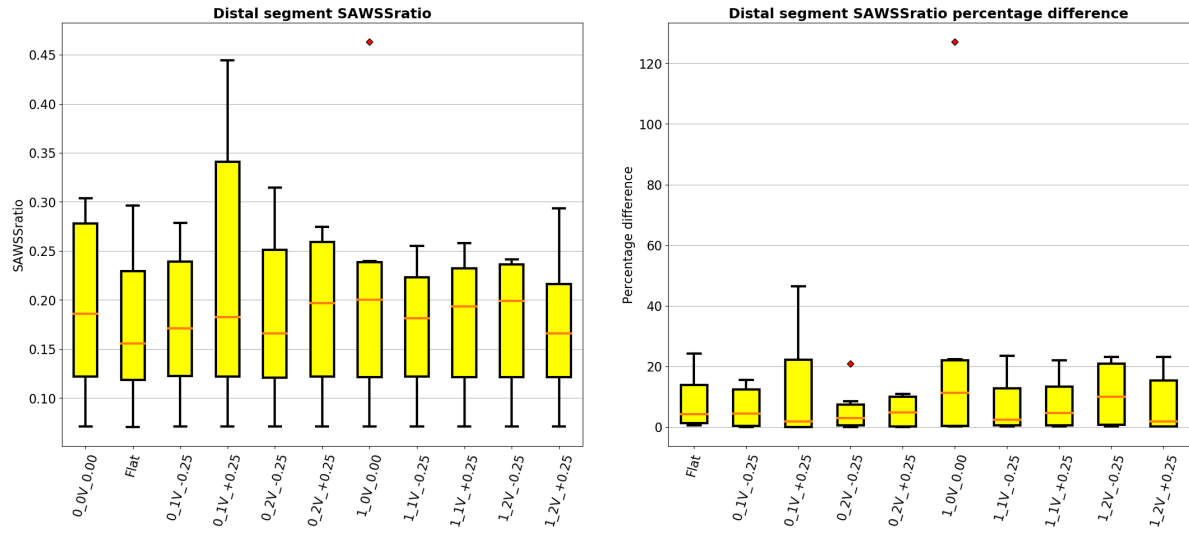


Figure 5.40 WSSratio summarizing boxplots (2)

5.2 Volume results

In this section the results related to bulk flow are presented using the volume hemodynamic descriptors discussed in paragraph 4.8

5.2.1 Local normalized helicity (LNH)

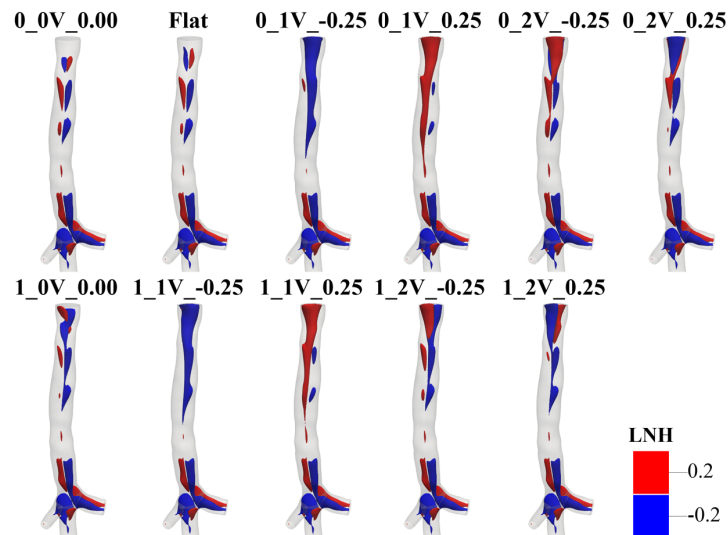


Figure 5.41 P4 LNH isosurfaces

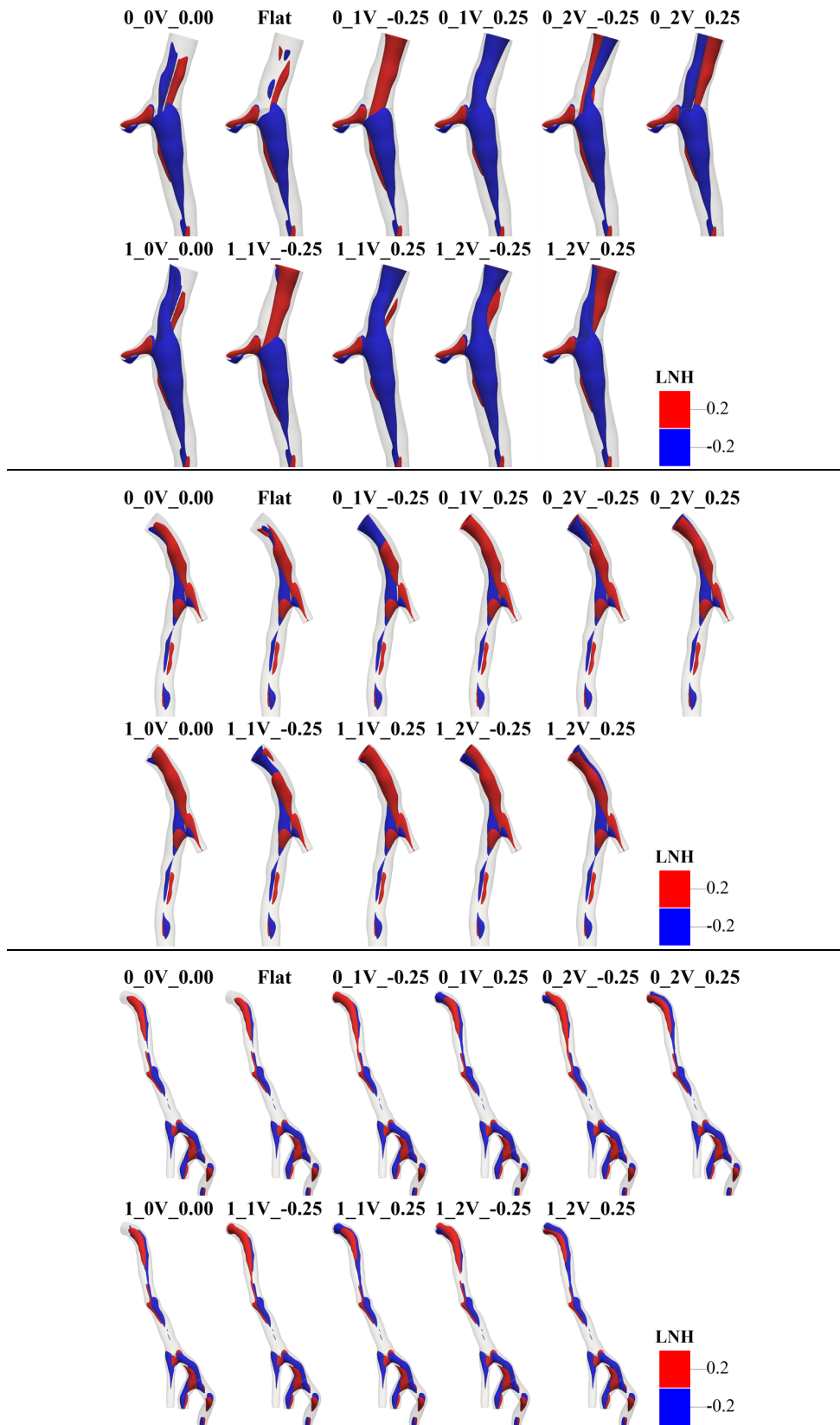


Figure 5.42 P8 (Top), P10 (Middle) and P14 (Bottom) LNH isosurfaces

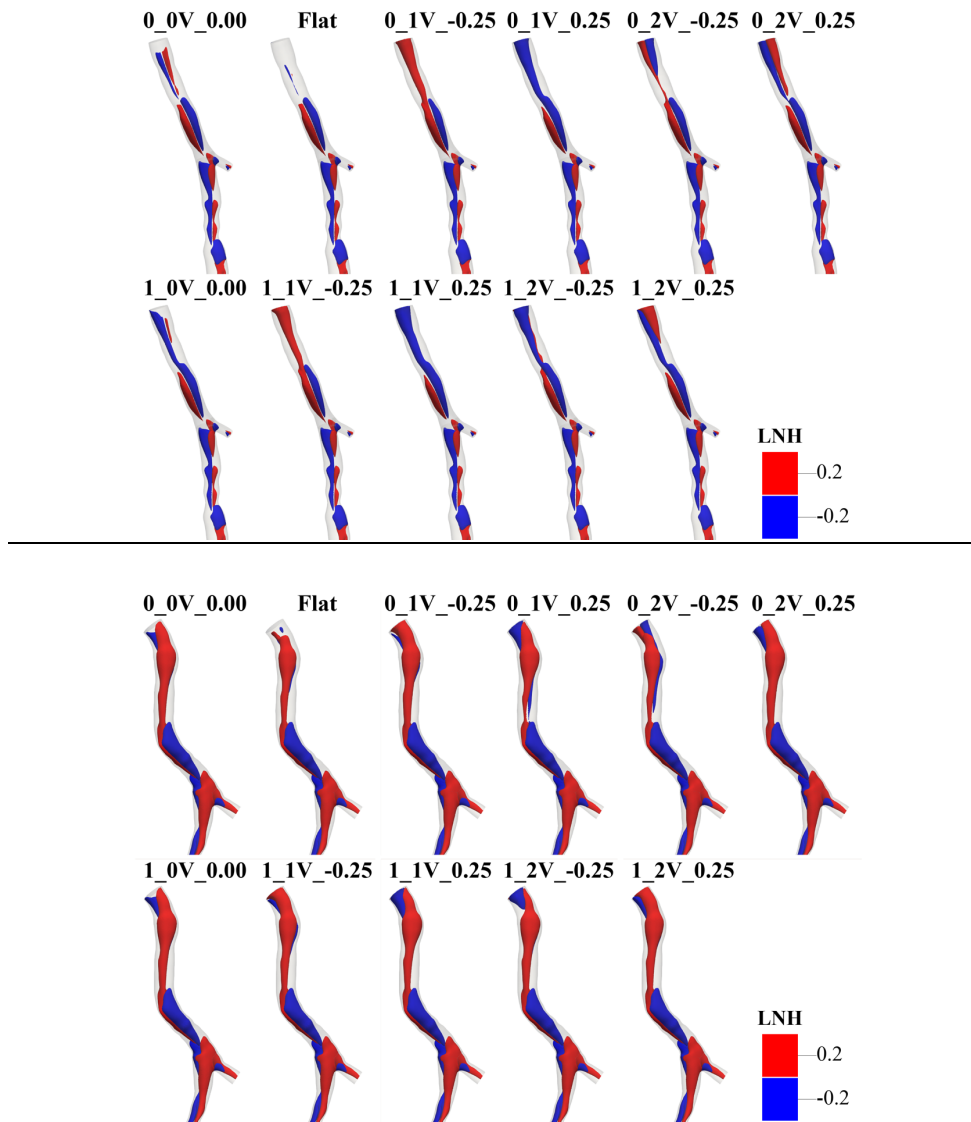


Figure 5.43 P19 (Top) and P23 (Bottom) LNH isosurfaces

The LNH isosurfaces show, as expected, the well-known helical pattern previously discussed. The isosurfaces seem to be influenced by the different shapes of the custom velocity profiles only near by the inlet surface of the vessels then, as already seen for wall descriptors, the flow pattern is no more shape varying.

5.2.2 Quantification of helicity

To quantitative characterize the helical flow features, the helicity-based descriptors mentioned in paragraph 4.8 were used. The results are depicted in the following summarizing boxplots.

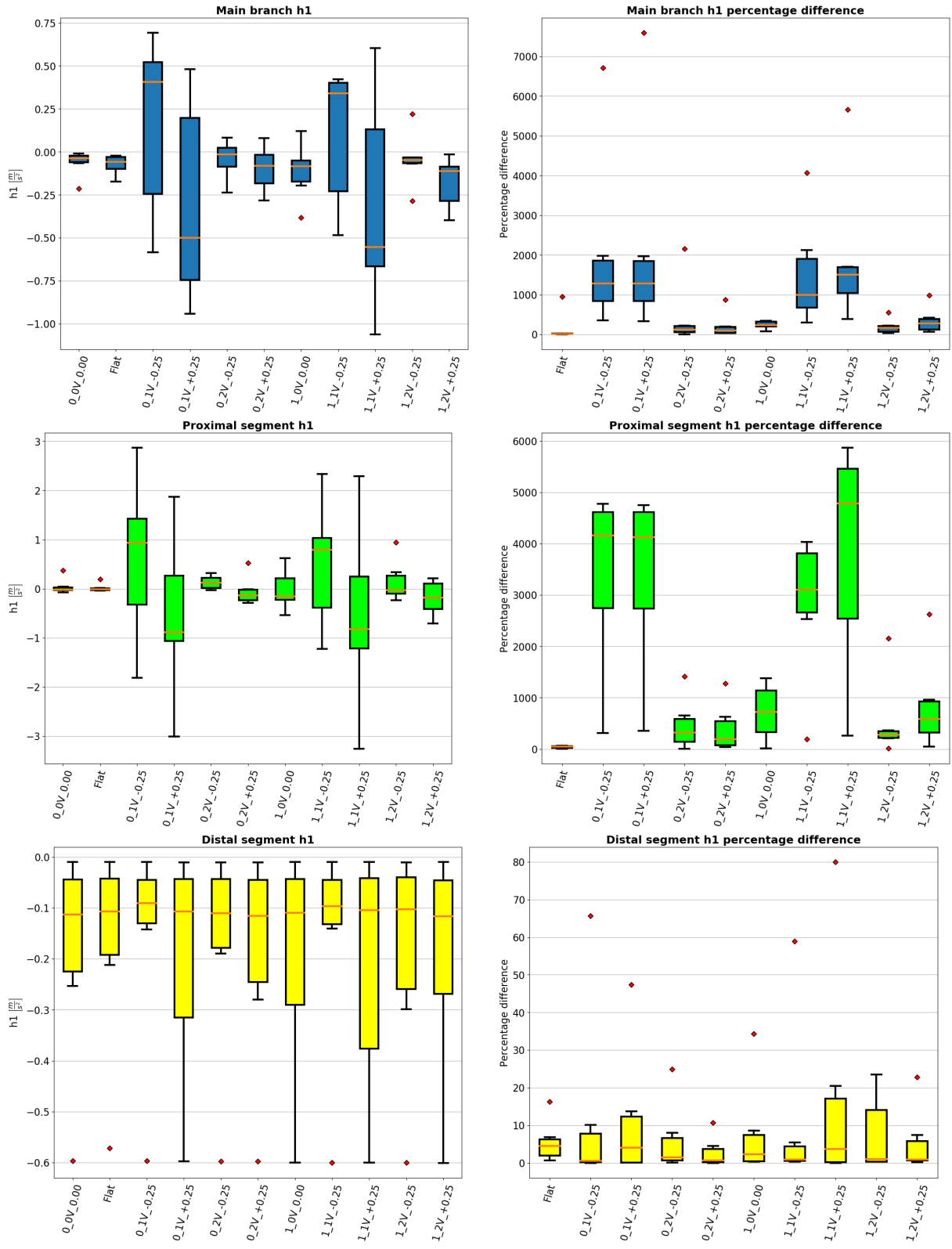


Figure 5.44 $h1$ summarizing boxplots

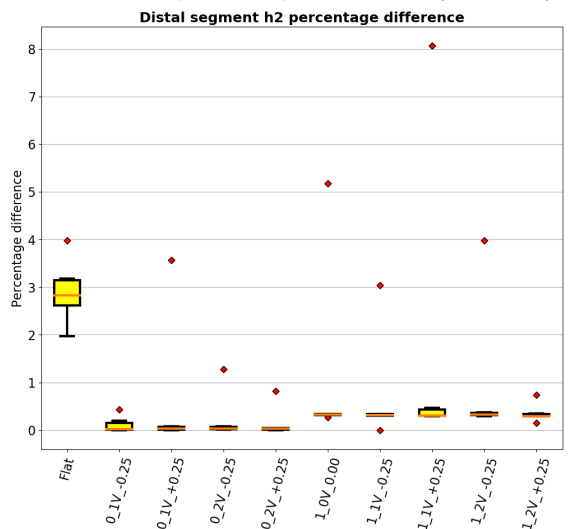
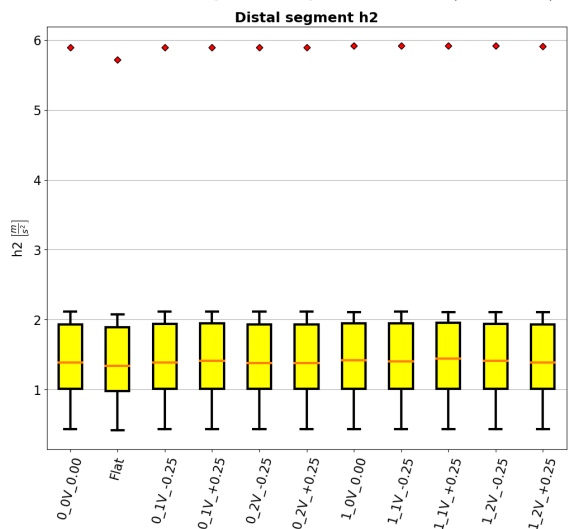
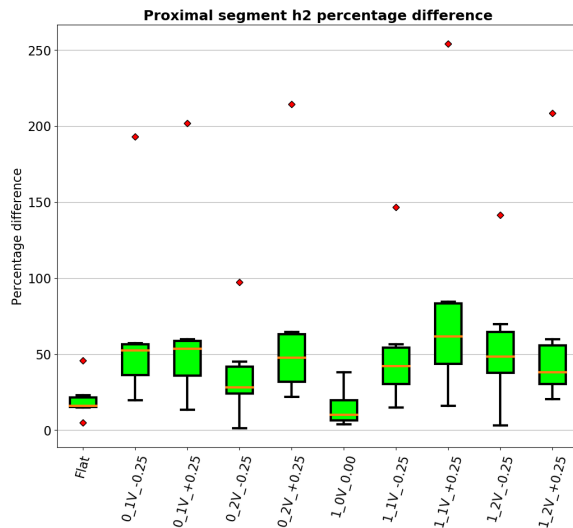
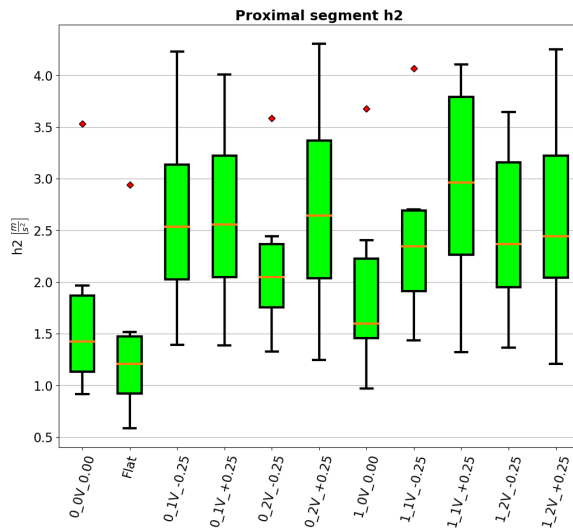
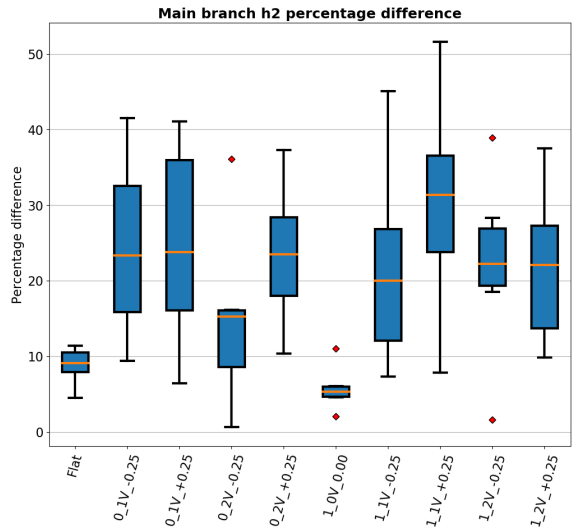
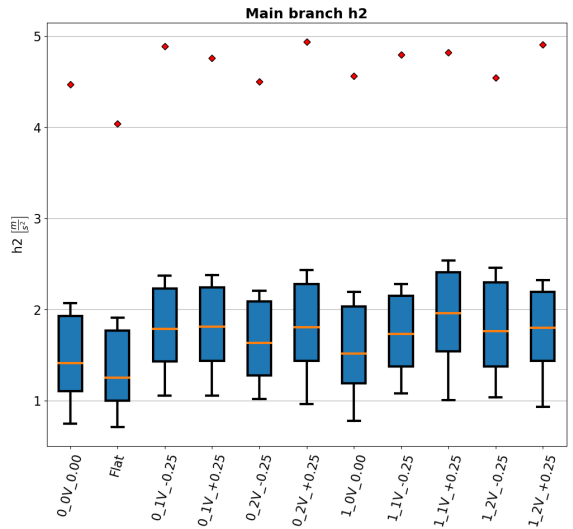


Figure 5.45 h2 summarizing boxplots

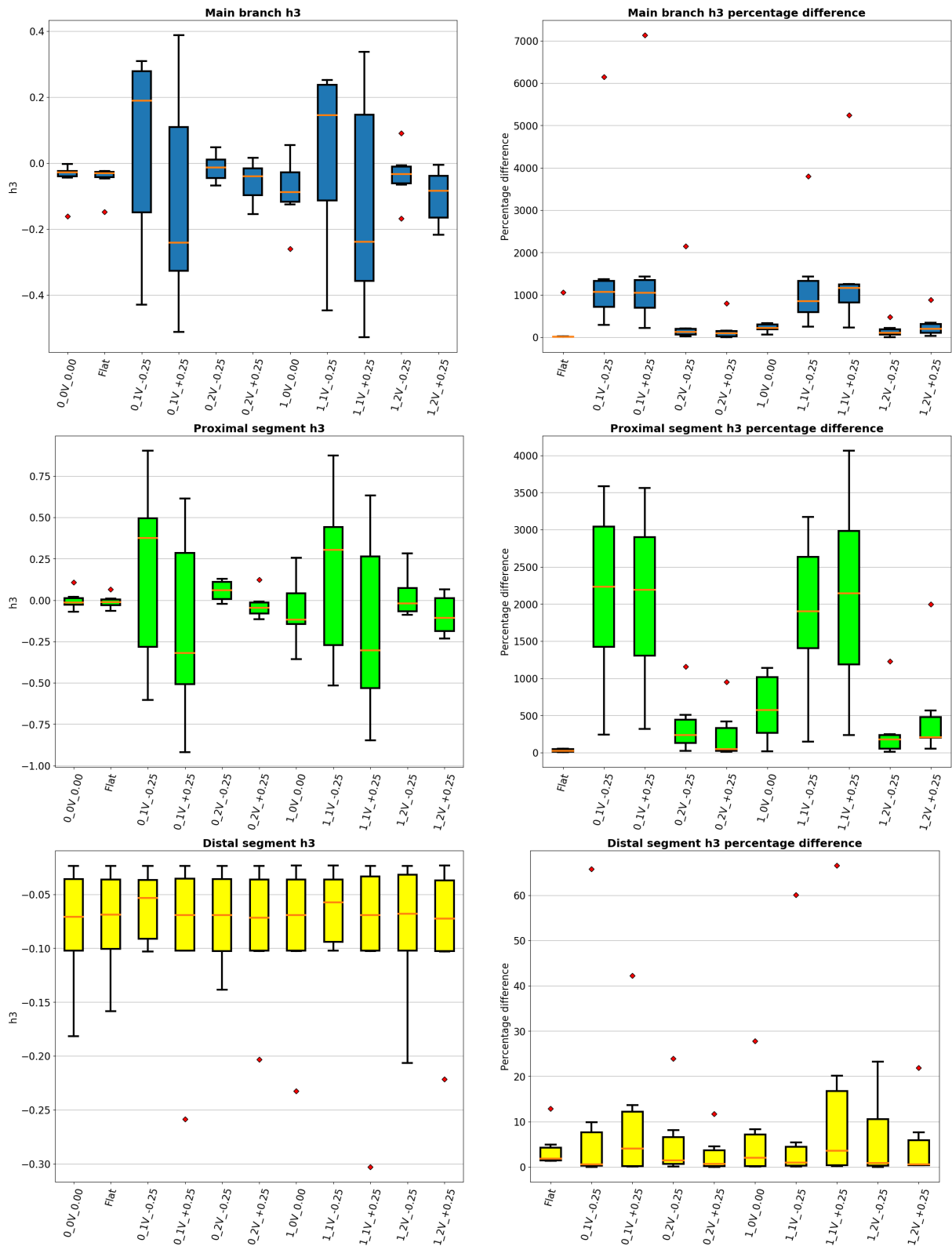


Figure 5.46 h3 summarizing boxplots

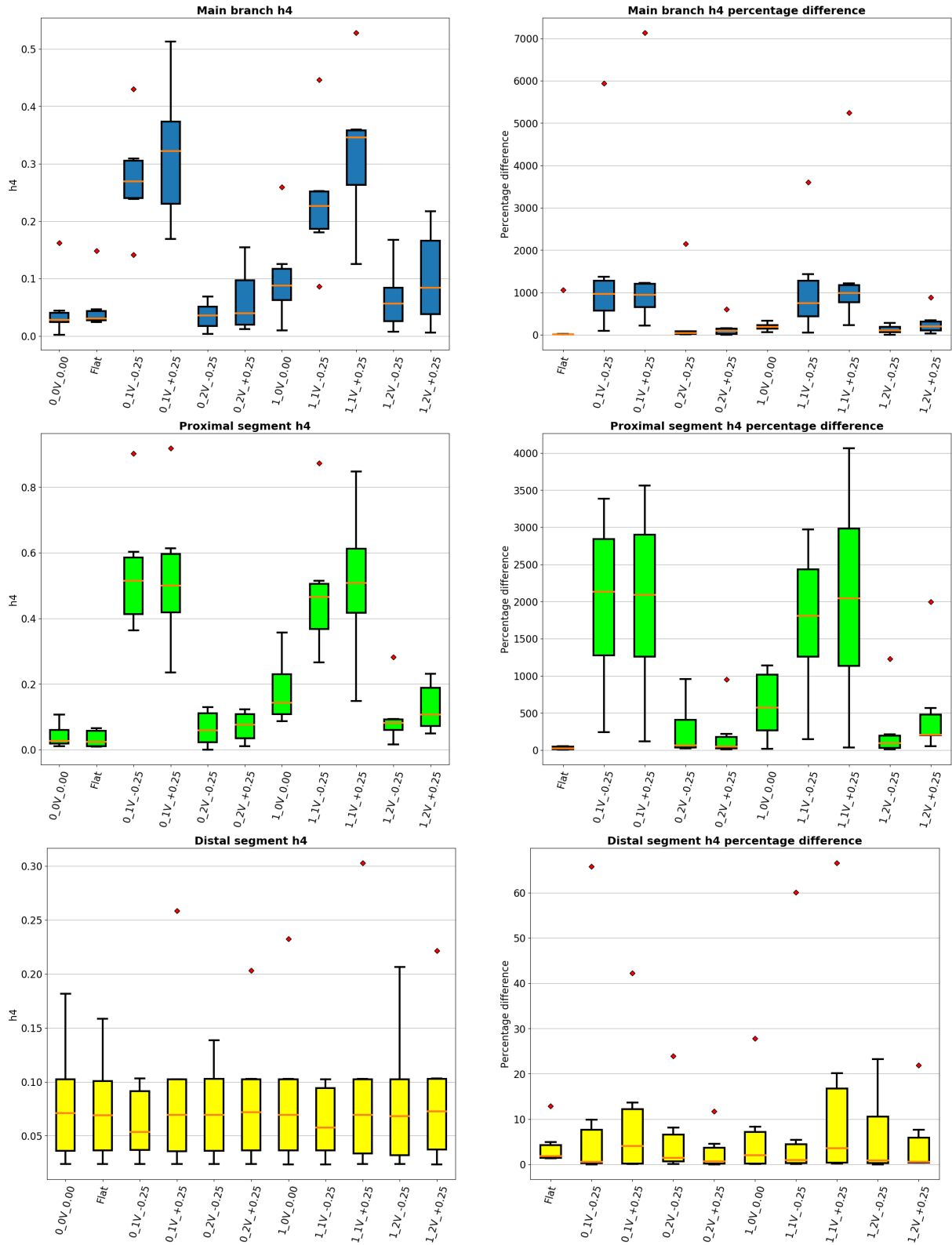


Figure 5.47 h4 summarizing boxplots

According to boxplots in Figure 5.44, flow pattern is dominated mostly by left-rotating structures since h_1 takes mainly negative values. Differences are many orders of magnitude higher in proximal segments than distals, where the medians are close to 0 which means that the fluid domain is characterized by two approximately symmetrical counter-rotating structures. The total amount of helical flow irrespective of direction, h_2 , is identically distributed in distal segments (Figure 5.45), in fact percentage differences take values close to 0. Instead, h_2 in proximal segments appears to be influenced by the shape of the profiles. The same considerations can be applied for h_3 and h_4 since those descriptors are non-dimensional quantities derived by h_1 and h_2 .

6 Conclusions

The aim of this thesis was to evaluate the impact that inflow velocity profile shape has on computational hemodynamic results. To do that, clinical images of left circumflex coronary arteries with no sign of atherosclerosis of 6 subjects that underwent heart transplant were considered. For each vessel, the three-dimensional geometrical model was reconstructed and meshed, and after some pre-processing steps of the model, steady-state simulations were performed prescribing 11 different velocity profiles based on analytical formulations. Then, near-wall and intravascular flow hemodynamic descriptors were obtained and processed. First, WSS results were examined. For all the considered LCXs, percentage differences color maps qualitatively show that differences between $0_0V_0.00$ (parabolic, reference velocity profile) and other profiles are greater near the inlet of the models and after a short vessel tract, percentage differences decrease near to 0%. Quantitatively, SAWSS percentage difference bar plots show that the differences in the proximal segments are greater than those in the distal segments (near to 0%) confirming qualitative visualization. For all the models, Flat velocity profile presenting higher values of WSS magnitude and a more pronounced difference probably due to its non-physiological shape. Also, axial (WSSax) and secondary (WSSsc) components of WSS were examined. As expected, WSSax presented similar values with respect to WSS magnitude, demonstrating that the axial component of velocity is predominant. As for the WSSsc, it takes lower values than WSSax and behaves in a complementary way: in not-curved sections takes lower values whereas in curved tracts, bifurcations and branching sites assumes higher values due to the onset of vortices and complex flows. Even in this case differences are remarkable only near the inlet zone, mostly for those three-dimensional velocity profiles having also the in-plane component of velocity represented by one or two vortices lying on the cross-sectional plane.

Near-wall analysis was concluded analyzing the WSS ratio, which presents percentage differences higher in the proximal segments near the inlet surface whereas they are close to 0 elsewhere as observed for the other WSS-based descriptors. As for intravascular flow results, LNH isosurfaces qualitatively show the well-known two counter-rotating structures very similar between the different profiles, except for the proximal regions where the shape of prescribed velocity profiles dictates the flow pattern. Helicity-based descriptors quantitatively show higher differences in the proximal segments, whereas in the remaining part of the arteries there are comparable situations. In conclusion this study was conducted aiming to investigate hemodynamic differences in left circumflex coronary arteries simulations due to the shape of the inlet velocity profile. From obtained results can be deduced that differences are mainly located near to the inlet of the vessel due to the “disturbance” induced by the velocity profile. After a short length along the artery, the flow pattern is no more influenced from the shape of the velocity profile which does not impact the computational hemodynamic results.

Bibliography

- [1] P. Buddiga, “Cardiovascular System Anatomy,” *Medscape*, pp. 1–2, 2014, [Online]. Available: <https://emedicine.medscape.com/article/1948510-overview>.
- [2] “anatomy-of-the-heart.” [Online]. Available: <https://qcg.com.au/sites/default/files/anatomy-of-the-heart.jpg>.
- [3] R. E. Klabunde, “Cardiovascular Physiology Concepts,” 2003, [Online]. Available: <http://www.cvphysiology.com/index.html>.
- [4] P. R. Hoskins, P. V. Lawford, and B. J. Doyle, *Cardiovascular Biomechanics*. 2017.
- [5] L. Formaggia, A. Quarteroni, and A. Veneziani, *Cardiovascular Mathematics*, vol. 53, no. 9. 2009.
- [6] K. Saladin, *Anatomy & Physiology: The Unity of Form and Function*, Third. 2003.
- [7] Oregon State University, “20.1 Structure and Function of Blood Vessels.” <https://open.oregonstate.edu/aandp/chapter/20-1-structure-and-function-of-blood-vessels/>.
- [8] M. R. Roach and A. C. Burton, “The reason for the shape of the distensibility curves of arteries,” *Can. J. Biochem. Physiol.*, vol. 35, no. 8, pp. 681–690, 1957, doi: 10.1139/o57-080.
- [9] T. Azuma and M. Hasegawa, “Distensibility of the vein: From the architectural point of view,” *Biorheology*, vol. 10, no. 3, pp. 469–479, 1973, doi: 10.3233/BIR-1973-10323.
- [10] “Coronary arteries.” [Online]. Available:

<https://www.google.com/url?sa=i&url=https%3A%2F%2Fwww.pinterest.com%2Fpin%2F556405728936521022%2F&psig=AOvVaw1pBFrhWVMO f92OnDD9-2BS&ust=1588751137302000&source=images&cd=vfe&ved=0CAIQjRxq FwoTCODJy6ydnOkCFQAAAAAdAAAAABAD>.

- [11] A. D. Villa, E. Sammut, A. Nair, R. Rajani, R. Bonamini, and A. Chiribiri, “Coronary artery anomalies overview: The normal and the abnormal,” *World J. Radiol.*, vol. 8, no. 6, p. 537, 2016, doi: 10.4329/wjr.v8.i6.537.
- [12] S. Kastellanos, K. Aznaouridis, C. Vlachopoulos, E. Tsiamis, E. Oikonomou, and D. Tousoulis, “Overview of coronary artery variants, aberrations and anomalies,” *World J. Cardiol.*, vol. 10, no. 10, pp. 127–140, 2018, doi: 10.4330/wjc.v10.i10.127.
- [13] U. Morbiducci, “Il tessuto ematico, lecture of the course ‘Biomeccanica del sistema cardiovascolare.’” 2017.
- [14] Wikipedia, “Atherosclerosis.” https://en.wikipedia.org/wiki/Atherosclerosis#Signs_and_symptoms.
- [15] E. Falk, “Pathogenesis of Atherosclerosis,” *J. Am. Coll. Cardiol.*, vol. 47, no. 8 SUPPL., pp. 0–5, 2006, doi: 10.1016/j.jacc.2005.09.068.
- [16] D. P. Faxon *et al.*, “Atherosclerotic vascular disease conference. Writing group III: Pathophysiology,” *Circulation*, vol. 109, no. 21, pp. 2617–2625, 2004, doi: 10.1161/01.CIR.0000128520.37674.EF.
- [17] T. W. Secomb, “Hemodynamics,” *Compr. Physiol.*, vol. 6, no. 2, pp. 975–1003, 2016, doi: 10.1002/cphy.c150038.
- [18] D. Gallo, “Fondamenti per lo studio della Biomeccanica dei Fluidi, lecture notes of the course ‘Biomeccanica dei fluidi.’” 2017.
- [19] F. M. Montecvecchi, “Bilanci di strato e nei continui, lecture notes of the course ‘Biomeccanica dei fluidi.’” pp. 1–42.

- [20] C. R. Ethier and C. A. Simmons, *Introductory Biomechanics From Cells to Organisms*. 2007.
- [21] P. Vennemann, R. Lindken, and J. Westerweel, “In vivo whole-field blood velocity measurement techniques,” *Exp. Fluids*, vol. 42, no. 4, pp. 495–511, 2007, doi: 10.1007/s00348-007-0276-4.
- [22] Wikipedia, “Hagen–Poiseuille equation.” https://en.wikipedia.org/wiki/Hagen–Poiseuille_equation.
- [23] A. Ostadfar, *Biofluid Mechanics: Principles and Applications*. 2016.
- [24] U. Morbiducci, “Meccanica dei fluidi cardiovascolari, lecture notes of the course ‘Biomeccanica del sistema cardiovascolare.’” 2011.
- [25] W. R. Dean, “Note on the motion of fluid in a curved pipe,” 1927.
- [26] G. De Nisco *et al.*, “The Atheroprotective Nature of Helical Flow in Coronary Arteries,” *Ann. Biomed. Eng.*, vol. 47, no. 2, pp. 425–438, 2019, doi: 10.1007/s10439-018-02169-x.
- [27] E. J. Topol *et al.*, “Textbook of Cardiovascular Medicine,” no. March, 2002.
- [28] C. G. Caro, J. M. Fitz-Gerald, and R. C. Schroter, “Atheroma and arterial wall shear. Observation, correlation and proposal of a shear dependent mass transfer mechanism for atherogenesis.,” *Proc. R. Soc. London. Ser. B. Biol. Sci.*, vol. 177, no. 46, pp. 109–159, 1971, doi: 10.1098/rspb.1971.0019.
- [29] A. M. Malek, S. L. Alper, and S. Izumo, “Hemodynamic Shear Stress and Its Role in Atherosclerosis,” *Am. Med. Assoc.*, vol. 282, no. 21, pp. 2035–2042, 1999.
- [30] R. M. Nerem, “Vascular fluid mechanics, the arterial wall, and atherosclerosis,” *J. Biomech. Eng.*, vol. 114, no. 4, pp. 274–282, 1992, doi: 10.1115/1.2891384.

- [31] U. Morbiducci, A. M. Kok, B. R. Kwak, P. H. Stone, D. A. Steinman, and J. J. Wentzel, “Atherosclerosis at arterial bifurcations: Evidence for the role of haemodynamics and geometry,” *Thromb. Haemost.*, vol. 115, no. 3, pp. 484–492, 2016, doi: 10.1160/TH15-07-0597.
- [32] J. Tu, K. Inthavong, and K. L. K. Wong, *Computational Hemodynamics-Theory, Modelling and Applications*. 2015.
- [33] H. K. Versteeg and W. Malalasekera, *An introduction to computational fluid dynamics*. 2007.
- [34] C. A. Taylor and C. A. Figueroa, “Patient-Specific Modeling of Cardiovascular Mechanics,” *Annu. Rev. Biomed. Eng.*, vol. 11, no. 1, pp. 109–134, 2009, doi: 10.1146/annurev.bioeng.10.061807.160521.
- [35] U. Morbiducci, R. Ponzini, D. Gallo, C. Bignardi, and G. Rizzo, “Inflow boundary conditions for image-based computational hemodynamics: Impact of idealized versus measured velocity profiles in the human aorta,” *J. Biomech.*, vol. 46, no. 1, pp. 102–109, 2013, doi: 10.1016/j.jbiomech.2012.10.012.
- [36] D. Gallo *et al.*, “On the use of in vivo measured flow rates as boundary conditions for image-based hemodynamic models of the human aorta: Implications for indicators of abnormal flow,” *Ann. Biomed. Eng.*, vol. 40, no. 3, pp. 729–741, 2012, doi: 10.1007/s10439-011-0431-1.
- [37] M. Markl *et al.*, “Advanced flow MRI: emerging techniques and applications,” *Clin. Radiol.*, vol. 71, no. 8, pp. 779–795, 2016, doi: 10.1016/j.crad.2016.01.011.
- [38] E. Doutel, J. Carneiro, J. B. L. M. Campos, and J. M. Miranda, “Experimental and numerical methodology to analyze flows in a coronary bifurcation,” *Eur. J. Mech. B/Fluids*, vol. 67, pp. 341–356, 2018, doi: 10.1016/j.euromechflu.2017.09.009.
- [39] R. Ponzini, C. Vergara, A. Redaelli, and A. Veneziani, “Reliable CFD-

- based estimation of flow rate in haemodynamics measures,” *Ultrasound Med. Biol.*, vol. 32, no. 10, pp. 1545–1555, 2006, doi: 10.1016/j.ultrasmedbio.2006.05.022.
- [40] H. J. Kim, I. E. Vignon-Clementel, J. S. Coogan, C. A. Figueroa, K. E. Jansen, and C. A. Taylor, “Patient-specific modeling of blood flow and pressure in human coronary arteries,” *Ann. Biomed. Eng.*, vol. 38, no. 10, pp. 3195–3209, 2010, doi: 10.1007/s10439-010-0083-6.
- [41] VMTK, “Computing centerlines.” <http://www.vmtk.org/tutorials/Centerlines.html>.
- [42] A. G. van der Giessen *et al.*, “The influence of boundary conditions on wall shear stress distribution in patients specific coronary trees,” *J. Biomech.*, vol. 44, no. 6, pp. 1089–1095, 2011, doi: 10.1016/j.jbiomech.2011.01.036.
- [43] U. Morbiducci *et al.*, “A rational approach to defining principal axes of multidirectional wall shear stress in realistic vascular geometries, with application to the study of the influence of helical flow on wall shear stress directionality in aorta,” *J. Biomech.*, vol. 48, no. 6, pp. 899–906, 2015, doi: 10.1016/j.jbiomech.2015.02.027.
- [44] D. Gallo, D. A. Steinman, P. B. Bijari, and U. Morbiducci, “Helical flow in carotid bifurcation as surrogate marker of exposure to disturbed shear,” *J. Biomech.*, vol. 45, no. 14, pp. 2398–2404, 2012, doi: 10.1016/j.jbiomech.2012.07.007.